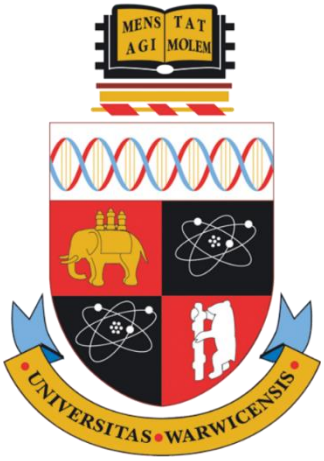

Magnetoelectric and Optoelectric Effects in Ferroelectric Tunnel Junctions

By

Zhengdong Luo

Thesis

Submitted to the University of Warwick

for the degree of

Doctor of Philosophy

Department of Physics

February 2019

To my mom and dad, and L.L.

For their loves

Contents

Acknowledgements

I would like to thank a lot of people for their great support which I could rely on to reach this final point of my PhD.

First and foremost, I would like to express my gratitude to my supervisor Prof. Marin Alexe for taking me into his group and introducing me into such an exciting field. I am extremely grateful to the freedom and guidance given by him allowing me to explore new projects. I would also like to thank him for his help, guidance and encouragement on my research. The tremendous trainings I received from him in the past three years are invaluable and will always guide me in the future life.

I am extremely thankful to Dr. Deasung Park, Dr. Akash Bhatnagar and Dr Geanina Apachitei for helping me get into the 'oxides world' from the very basic substrate treatment method all the way up to the sophisticated sample characterisations.

I owe a debt of gratitude to Dr. Mingmin Yang and his wife Dr. Danqing Liu for their great support in research and general life. I am grateful to Mingmin's ever helping attitude and generosity of sharing his samples even though he knew that the 'lending' was the process of destroying the samples.

I would like to thank my friends in Engineering department: Dr. Tianxiang Dai, Changwei Zheng and Dr. Fan Li. Without their kind help, I would have never been able to master the cleanroom facilities and photolithography fabrication method.

I would like to express my deep gratitude to Dr. Daniele Preziosi for his 'written in Thesis' experience on thin film growth and magnetoresistance measurements. Also, I am grateful to his very kind help during my stay at PSI synchrotron beamline.

Thanks are due to my friends in University of Warwick with whom I shared great times: Dr. Haiyuan Wang, Collins, Ray Zhou, Xue Xia, Andreas and his girlfriend Shannon, 'the Doctor' Tom Shortland, Ashleigh and many others. Without their wonderful friendship, it is not possible for me to reach here.

I would also like to acknowledge the support from Dr. Martin Lees, Michael Crosbie, Dr. Mark Crouch, Dr. Neil Wilson and Dr. David Walker on experiment facilities.

I am deeply grateful to my mom and dad for their endless support and love. Finally, words cannot express my gratitude to my wife Lin for her patience, her love and her company over the long journey.

Declarations

I declare that the content of this Thesis is my own work carried out at the Department of Physics, University of Warwick, between October 2015 and February 2019 under the supervision of Professor Marin Alexe. The research results reported here has not been previously submitted, either wholly or in part, for admission to a higher degree in any academic institution.

The $PbTiO_3/La_{0.7}Sr_{0.3}MnO_3$ heterostructure samples used in Chapter 4 were grown at the 'Max Planck' Institute for Microstructure Physics in Halle Germany by Dr. Geanina Apachitei. The transmission microscopy sample preparation and analysis in this work have been done by Dr. Jonathan James Prescott Peters under the supervision of Prof. Ana Sanchez in the Microscopy group at Warwick University. All the other sample growth and characterisations were carried out by the author.

Zhengdong Luo

February 2019

List of publications during PhD

[1] **Zhengdong Luo**, Daesung Park, Ming-Min Yang, and Marin Alexe. 'Light-controlled nanoscopic writing of electronic memories using the tip-enhanced bulk photovoltaic effect', *ACS applied materials & interfaces* 11(8) 8276. 2019

[2] Dae-Sung Park, Gregory J Rees, Haiyuan Wang, Diana Rata, Andrew J Morris, Igor V Maznichenko, Sergey Ostanin, Akash Bhatnagar, Che Jong Choi, Ragnar DB Jónsson, **Zhengdong Luo**, et al. 'Electromagnetic Functionalization of Wide-Bandgap Dielectric Oxides by Boron Interstitial Doping', *Advanced Materials* 30 (39) 1802025. 2018.

[3] **Zhengdong Luo**, Geanina Apachitei, Ming-Min Yang, Jonathan JP Peters, Ana M Sanchez, and Marin Alexe. 'Bi-ferroic memristive properties of multiferroic tunnel junctions', *Applied Physics Letters*, 112: 102905. 2018.

[4] Mehmet Sanlialp, **Zhengdong Luo**, Vladimir V Shvartsman, Xianzhu Wei, Yang Liu, Brahim Dkhil, and Doru C Lupascu. 'Direct measurement of electrocaloric effect in lead-free $Ba(Sn_xTi_{1-x})O_3$ ceramics', *Applied Physics Letters*, 111: 173903. 2017.

[5] Ming-Min Yang, **Zhengdong Luo**, Dong Jik Kim, and Marin Alexe. 'Bulk photovoltaic effect in monodomain $BiFeO_3$ thin films', *Applied Physics Letters*, 110: 183902. 2017.

[6] Ming-Min Yang, Akash Bhatnagar, **Zhengdong Luo**, and Marin Alexe. 'Enhancement of local photovoltaic current at ferroelectric domain walls in $BiFeO_3$', *Scientific Reports*, 7: 43070. 2017.

[7] Dawei Zhang, Yonggang Yao, Minxia Fang, **Zhengdong Luo**, Lixue Zhang, Linglong Li, Jian Cui, Zhijian Zhou, Jihong Bian, and Xiaobing Ren. 'Isothermal phase transition and the transition temperature limitation in the lead-free (1-x) $Bi_{0.5}Na_{0.5}TiO_3$-x$BaTiO_3$ system', *Acta Materialia*, 103: 746-53. 2016.

[8] Ran Su, **Zhengdong Luo**, Dawei Zhang, Yang Liu, Zhipeng Wang, Junning Li, Jihong Bian, Yanxi Li, Xinghao Hu, and Jinghui Gao. 'High energy density performance of polymer nanocomposites induced by designed formation of $BaTiO_3$@ sheet-likeTiO_2 hybrid nanofillers', *The Journal of Physical Chemistry C*, 120: 11769-76. 2016.

Unpublished Work

Zhengdong Luo, Jonathan J.P. Peters, Ana M. Sanchez and Marin Alexe. 'Flexible memristors based on single-crystalline ferroelectric tunnel junctions' (under review)

Abstract

Ferroelectric tunnel junctions (FTJs) consisting of two electrodes separated by an ultrathin ferroelectric tunnel barrier can exhibit giant resistance switching by ferroelectric polarisation reversal and allow for non-destructive information readout. By exploiting the internal degree of freedom-ferroelectric domain structure and external structure design-stacking with ferromagnetic electrodes, FTJs can be further enhanced with electric memristive behaviours and the magnetic field controllable operation. More and more novel properties are expected to be studied in FTJs as most of the constituent materials are made from transition metal oxides which could accommodate a wide range of fascinating properties. Therefore, FTJs have established themselves as an intriguing platform for novel electronic applications.

To fully exploit the potential of FTJs in order to meet the requirements of current information storage industry such as ever-higher data storage densities, lower energy consumption, multifunction features and even form factor such as flexible and stretchable mechanical properties, new physics and materials along with innovative device fabrication strategies for FTJ-based systems are urgently needed. In this work, we first explored the possibility of magnetoelectrically coupled ferroelectric tunnel memristor. By combining the transport results and the virtualised ferroelectric domain evolution upon a set of electric fields, we came up with a qualitative physical model which can well describe the observed coupling between the tunnelling electroresistance and tunnelling magnetoresistance. The second block of this work is the study of a hybrid FTJ and ferroelectric photovoltaic cell device which realised the reversible optic control of resistance switching in FTJs. The mechanism of controlling the FTJ resistance states by the tip-enhanced photovoltaic effect is explained. Operation parameters including writing speed and strength are discussed in detail. The final subject is devoted to the development of flexible ferroelectric tunnel memristors using transferable FTJ nanomembranes. We studied the epitaxial layer transfer method and managed to obtain ultrathin single-crystalline ferroelectric oxide membranes. By comprehensive structural investigations, we revealed that the well-preserved single-crystal structure and compressive strain state in ferroelectric nanomembranes are key for the existence of ferroelectricity. Flexible memristive FTJs were made by mounting ferroelectric nanomembranes on plastic substrates and displayed excellent functional properties. Overall, this work not only provides new insights into the unprecedented magnetoelectrically and optoelectrically coupled systems with ultrathin ferroelectric oxide layers but also offers the strategy to extend their applications to flexible systems.

Abbreviations

FTJ	Ferroelectric tunnel junction
FeRAM	Ferroelectric random access memory
MFTJ	Multiferroic tunnel junction
BTO	$BaTiO_3$
WKB	Wentzel-Kramers-Brillouin
DOS	Density of states
FNT	Fowler-Nordheim tunnelling
TI	Thermionic injection
TER	Tunnelling electroresistance
TMR	Tunnelling magnetoresistance
MTJ	Magnetic tunnel junction
BPV	Bulk photovoltaic effect
vdW	Van der Waals
SRO	$SrRuO_3$
PLD	Pulsed laser deposition
STO	$SrTiO_3$
HF	Hydrogen fluoride
LSMO	$La_{0.67}Sr_{0.33}MnO_3$
T_c	Curie temperature
PTO	$PbTiO_3$
PZO	$PbZrO_3$
PZT	$PbZr_{0.2}Ti_{0.8}O_3$
BFO	$BiFeO_3$
SAO	$Sr_3Al_2O_6$
XRD	X-ray diffraction
FWHM	Full-width-at-half-maximum
RSM	Reciprocal space mapping
STEM	Scanning transmission electron microscopy
FIB	Focused ion beam
AFM	Atomic force microscopy
PSPD	Position sensitive photodetector
PID	Proportional-integral-differential
PFM	Piezoresponse force microscopy
IP	In-plane
OOP	Out-of-plane
C-AFM	Conductive-AFM
Ph-AFM	Photo-AFM

SQUID	Superconducting QUantum Interference Device
PPMS	Physical Property Measurement System
u.c.	Unit cell
ADF	Annular dark field
PMMA	Poly methyl methacrylate

Chapter 1

Introduction

Ferroelectrics, which possess switchable polarisation representing ‘0’ and ‘1’ data bits, are an ideal building block for computer memory applications. A successful example is the ferroelectric random access memory (FeRAM) which is the fundamental component for low power, long retention, radiation resistant microprocessor-based systems.[1] For instance, FeRAMs are widely used e-money or transport smart cards which holds a tremendous global market size. The capacitive readout of binary polarisation states from the ferroelectric layer typically at around one hundred nanometre thickness however could constitute two main obstacles for the development of FeRAMs: destructive readout necessitating a write-read-write cycle and poor scalability with low storage densities.[2, 3]

Nowadays, trends in information storage applications demand ever-higher data storage densities, lower power consumption, multifunction features and even form factor such as flexible and stretchable mechanical properties. The emergence of ferroelectric tunnel junctions (FTJs) in which two electrodes sandwich a few nanometre-thick ferroelectric barrier, has reinvigorated interests in ferroelectric memories and is promising to meet the aforementioned requirements of advanced data storage applications. Similar to FeRAMs, data bits in FTJs are encoded by ferroelectric polarisation, but probed by the charge tunnelling current which gives rise to the non-destructive readout. Recent works have demonstrated that FTJs can have ON/OFF resistance ratios reaching up to six orders of magnitude and are of very high storage densities, which has established themselves as a promising candidate for new type memories.[4] Employing another degree of freedom in ferroelectrics namely domain structure as the control parameter, memristive behaviours can be obtained in FTJs.[5] These ferroelectric tunnel memristors operating with pure electronic effect could mimic the bio-synapse behaviours and are ideal for use in neuromorphic computing architectures. Furthermore, due to the

ultrathin thickness of the ferroelectric layer, the interface properties become significant in the FTJs. Bringing the ferroelectric layer in contact with ferromagnetic electrodes, interface reconstruction leads to the artificial multiferroicity at the ferroelectric/ferromagnetic interface and results in the ferroelectric polarisation controllable spin polarisation.[6] Such a phenomenon inspired the development of multiferroic tunnel junctions (MFTJs) which could deliver a new type of four state magnetoelectrically coupled memory and serve as an interesting platform to explore the interplay between spin, charge and lattice.

Beyond the demonstrated achievements, how to further enhance the operation performance and deliver more complex functions than simply electric controlled switching remains as an outstanding question, driving the future development of FTJ-based structures. For example, despite the pure-electronic ferroelectric tunnel memristors, can this kind of memristor also be controlled using magnetic field or even remotely by light? If possible, what would be the physics behind such operations? Moreover, as the world is witnessing the booming of flexible electronics, can FTJ-based heterostructures be integrated on those soft substrates and thus be pushed forward for future flexible electronic memories? The quest for these novel functions therefore requires the bold association of different materials, novel device geometries and advanced fabrication strategies along with a deeper understanding of the related physics in FTJ-based structures.

To this end, the objective of the present Thesis is to investigate and understand the magnetically and optically controllable novel resistive switching phenomena in FTJ-related oxide structures and explore the strategy to fabricate flexible memory devices based on ultrathin ferroelectric oxide nanomembranes. The structure of the work will be organised as the following:

Chapter 2 presents the fundamental background for understanding the displayed results. It covers the basics of ferroelectricity, ferroelectric perovskite oxide materials and polarisation preservation at ultrathin thickness. Charge transport mechanisms, resistance switching principles, domain configuration enabled

memristive behaviours and spin-dependent tunnelling in FTJs will then be discussed. It also gives a brief overview of photovoltaic effect in ferroelectrics including the origin of bulk photovoltaic effect and the tip enhancement along with the definition and current development of ferroelectric thin film based flexible electronics.

Chapter 3 offers the introduction of sample preparation including thin film growth and device fabrication and provides a detailed explanation of various experimental techniques and tools used in this work. All the materials used in this Thesis with a focus on their structure properties are presented. The research methodology has been to perform crystal structure characterisation, local surface topography and ferroelectricity investigation as well as electrical measurements with optic and magnetic stimuli on obtained FTJ samples.

Chapter 4 demonstrates a magnetoelectrically coupled or bi-ferroic FTJ memristor. This topic involves the experimentally observed magnetic field and electric filed controllable multibit resistant states in a multiferroic tunnel junction. To interpret this novel phenomenon, a plausible scenario based on the multidomain configuration in the ferroelectric barrier is developed, where the ferroelectric domains play the role as both charge and spin conduction channels.

Chapter 5 describes an exciting combination of FTJs with a ferroelectric photovoltaic cell. By utilising the strong electric field originating from the tip-enhanced photovoltaic effect, we realised the reversible switching of resistance states in FTJs with nanosized contact by exclusively light control. The mechanism of the light-enabled electric writing is discussed in detail. Key parameters of an optoelectronic memory including operation speed, light intensity for electric writing, etc. are discussed. A prototype design of a hybrid full optic-controlled electronic memory is introduced.

Chapter 6 devotes to show a flexible FTJ-based memristor and the generic approach for obtaining transferrable single-crystalline ferroelectric oxide nanomembranes. In particular, through the grow-transfer method, a 3.6 nm thick $BaTiO_3$ ferroelectric

oxide thin film can be obtained and transferred on plastic substrates. The well-preserved crystal structure along with the compressive strain state allow for the existence of robust ferroelectricity in the freestanding thin $BaTiO_3$ nanomembranes. Furthermore, highly flexible memristors based on the FTJ nanomembranes are systematically investigated.

Finally, Chapter 7 draws main conclusions of the work and provides a short outlook concerning the future development of FTJs and ferroelectric thin films.

Chapter 2

Fundamentals

In this chapter, we present necessary background information related to the current work. Basic definitions and physical mechanisms related to ferroelectricity and ferroelectric perovskite oxide materials are first introduced. Next, ferroelectric tunnelling junction and its extension to the so-called multiferroic tunnel junction are discussed which covers the basic concepts and working principles. As tip-enhanced photovoltaic effect was used as the method for optical-enabled writing in this work, a brief introduction of ferroelectric photovoltaics is thus provided. Last, the state of the art of the emerging flexible single-crystalline ferroelectric oxide nanomembranes is presented.

2.1. Introduction to ferroelectrics

2.1.1 Ferroelectricity in perovskite oxides

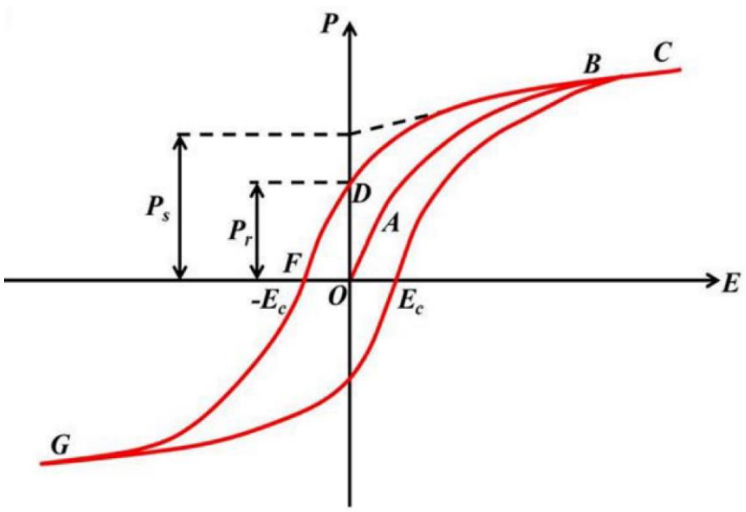

Figure 2.1: A typical ferroelectric hysteresis loop. Adapted from the reference [8].

Ferroelectrics are polar materials in which at least two equilibrium orientations of the spontaneous polarisation vector exist in the absence of an external electric field. In such a system, the spontaneous polarisation vector can be switched between

these orientations through applying an electric field.[7] Due to the occurrence of domain structures, the ferroelectrics exhibit hysteresis phenomena during the switching process. A typical macroscopic hysteresis loop of ferroelectric switching is schematically depicted in Figure 2.1.[8] In an ideal ferroelectric crystal, the hysteresis loop should be symmetric, from which important ferroelectric parameters such as coercive field, saturated/remnant polarisation can be extracted.

Ferroelectrics have been an extensive subject of research due to their great potential for information storage applications as the switchable electric polarisation characteristic is ideal for the '0' and '1' data bits.[2] In the past years, most of the studied ferroelectric materials are perovskite oxides which commonly share a simple ABO_3 crystal structure, where A and B respectively represent a cation element.[9] An example of a prototype perovskite ferroelectric oxide, i.e., barium titanate $BaTiO_3$ (BTO) is presented in Figure 2.2. In its centrosymmetric cubic perovskite unit cell (Figure 2.2a), the Ba atoms form the corners of the cube and those face-centred oxygen anions form the octahedron within the cube. The Ti atom sits in the centre of the cube leading to its six-fold coordination. In this highly-symmetric structure, the BTO only exhibits paraelectric response to external electric field and hence is not ferroelectric. Such a structure normally exists in BTO at temperatures above the Curie temperature. In order for the ferroelectricity, a non-centrosymmetric arrangement of the ions and their corresponding electrons is needed. For example, as shown in Figure 2.2b and 2.2c, the BTO is with a tetragonal unit cell at room temperature, which is lower than its Curie temperature, and exhibits spontaneous polarisation as a consequence of the electric dipole moment created by the relative shift between the Ba and Ti sublattices and the oxygens. The ferroelectric polarisation per unit cell grows with increasing shift of the constituent ions against each other, which suggests the possibility of manipulation of the ferroelectricity through increasing the tetragonality of the crystal unit cell.[10]

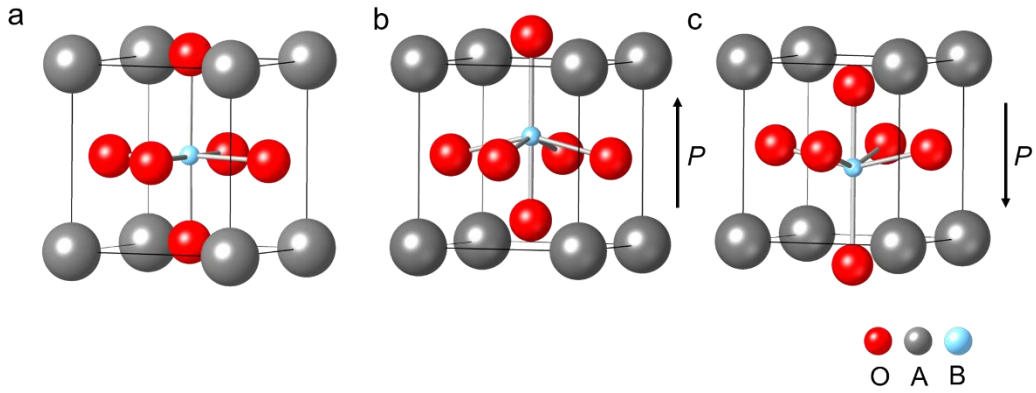

Figure 2.2: The crystal structure of typical ABO_3 perovskite. In the case of BTO, A = Ba, B = Ti and six oxygen anions form the octahedron. (a) The cubic unit cell with no ferroelectricity. (b) and (c) for polar distorted unit cells with upward and downward spontaneous polarisations, respectively. Picture produced by the commercial software CrystalMaker.

2.1.2 Critical thickness for ferroelectricity

Trends in consumer electronics keep requiring electronic devices with reduced size and lower operating power. Moreover, characterisation and understanding the thin film behaviours with reducing size might lead to novel properties despite that the competing effects such as misfit strain from substrate, surface properties and fundamental size quantisation make the objective highly challenging.[11] Therefore, it is becoming more and more important to study the functional properties of ferroelectrics at ultrathin thickness from both research and application perspectives. Considering an ideal ferroelectric crystal thin film, the ferroelectricity is mainly influenced by the electrostatic conditions at the surfaces. Recalling the generation of spontaneous polarisation in ferroelectric perovskite, the net electric dipole moment will inevitably lead to the formation of net charges at the surfaces of the ferroelectric, which thus produce an extra electric field termed depolarisation field pointing antiparallel to the polarisation direction. In a typical metal/insulator/metal capacitor structure, the depolarisation field can be screened with ‘perfect’ metal electrodes. However, the screening charges are not sufficient to compensate the

depolarisation field due to the finite screening length in realistic metals. Thus, the residual depolarisation field cannot be eliminated and tends to destabilise the ferroelectric polarisation. In the case of ultrathin films, the depolarisation field becomes more severe due to the significant finite screening at metal/ferroelectric interfaces and drives the formation of domains with opposite polarisation.[11, 12] Moreover, in realistic ferroelectric films, defects like oxygen vacancies could also destabilise the polarisation and further induce the degradation of ferroelectric properties such as fatigue.[13]

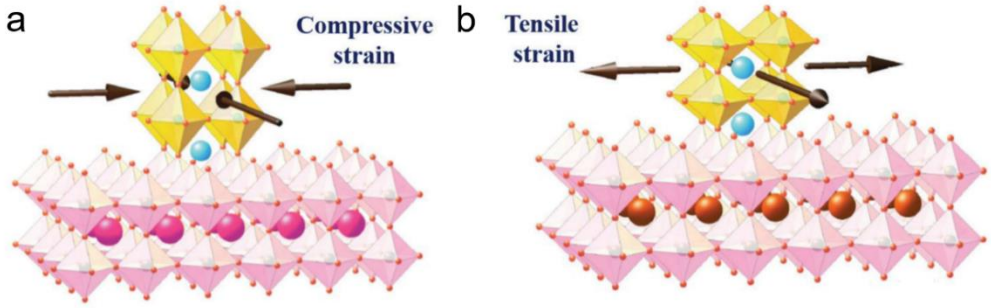

Figure 2.3: Schematic illustration of the compressive (a) and tensile (b) strain engineering by growing thin film on substrate with misfit lattice parameters. Adapted from the reference [10].

Regardless the debate on the critical thickness of ferroelectricity,[11, 14] the experimentally probed thickness for the existence of stable ferroelectricity in perovskite ferroelectric thin films shows an significant decrease in recent years thanks to the maturity of film growth technique and the proposed strain engineering strategy (see Figure 2.3). It is well known that experimentally obtained thin films can be predominately controlled by the thin film quality in terms of their properties. For example, defects like oxygen vacancies, structure deviation from right stoichiometry, dead layer, etc., can cause severe degradation of ferroelectric behaviours. These problems can be tackled by optimising the film growth parameters. On the other hand, intrinsic tuning of the crystal structure of the ferroelectric oxide films can be realised by strain engineering using substrate with

misfit lattice to the growth material.[10, 15] For example, stable and controllable polarisation was observed in 1 nm thick BTO layer which is with a high tetragonality by aid of the compressive strain imposed by the $DyScO_3$ substrate.[16] Therefore, it suggests a practical and efficient way towards ultrathin ferroelectric layer-based systems by using strain engineering in the ferroelectric thin films.

2.2. Ferroelectric tunnel junctions

2.2.1 Charge transport in ultrathin ferroelectric barriers

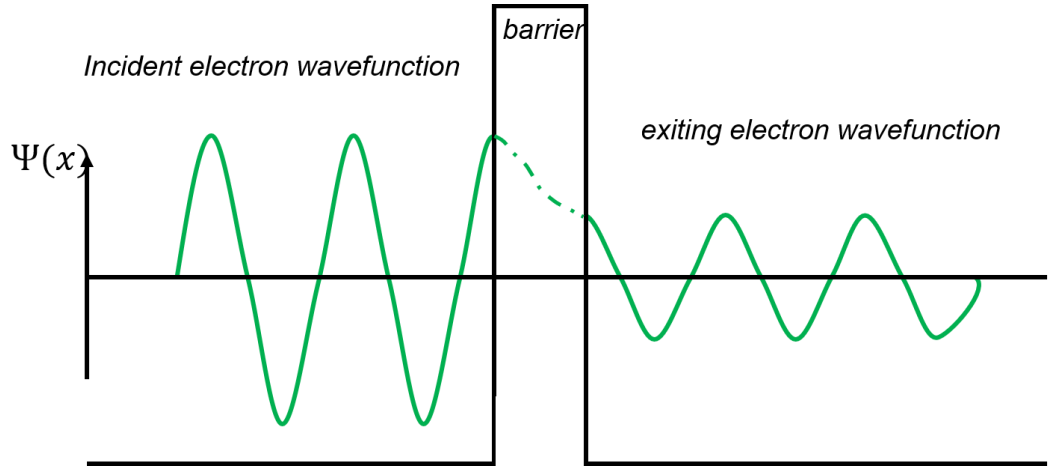

Figure 2.4: Schematic sketch of the wavefunction of an electron tunnelling through the potential barrier with the energy lower than the barrier height.

Similar to metal/insulator/metal (M-I-M) tunnel junction structures in which quantum tunnelling happens when applying a voltage across the ultrathin insulator barrier. Ferroelectric tunnel junctions (FTJs) are M-I-M structures in which the polar material-ferroelectrics are used as the tunnelling barrier. Due to the similar structure, FTJs share the common tunnelling processes as the normal tunnel junctions in which the charge tunnelling can be described by the probability density of its wave function as schematically shown in Figure 2.4. As shown in Figure 2.4, when an electron encounters a potential step, the incident electron wave function intensity decreases exponentially through the barrier but can still extend to the other side of the barrier where the electron can be found with a finite probability. In such

a planar tunnel junction, the electron tunnels through a one-dimensional potential barrier *V(x)*, is described by a wave function $\psi(x)$, which satisfies the Schrödinger equation,

$$-\frac{\hbar^2}{2m}\frac{d^2}{dx^2}\psi(x) + V(x)\psi(x) = E\psi(x) \tag{2-1}$$

at a given position *x*. Here *m* is the mass of an electron, $\hbar$ is the reduced Planck constant. Considering $V_L = V_R = -V$ at the left and right electrode locations, when the electron with an energy *E* can tunnel through the electric potential *V(x)* (*E* > *V)*, the solutions of the above equation are $\psi(x) = \psi(0)e^{\pm ikx}$ where $\boldsymbol{k}$ is the wave vector as $k = \frac{2m(E-|V|)}{\hbar}$. In the classically forbidden region, within the barrier, the solution is given by $\psi(x) = \psi(0)e^{-2\varkappa x}$, where $\varkappa = \frac{\sqrt{2m(|V|-E)}}{\hbar}$ being the decay constant that describes the electron penetrating the tunnel barrier into the *x* direction. The probability density of the electron near point *x* is finite in the barrier region and is proportional to $\psi(x)^2$. Define the transmission coefficient *T* as given by the ratio between transmitted current density and the incident current, by using the Wentzel-Kramers-Brillouin (WKB) approximation[17], we can write:

$$T \propto e^{-2\int_{x_1}^{x_2}\sqrt{\frac{2m(V(x)-E)}{\hbar}}dx} \tag{2-2}$$

Applying a bias *V* across the rectangular shaped barrier, the total tunnelling electric current I_{l-r} which is the sum of the electrons that can tunnel through is given as:

$$I_{l-r} \propto \int_{-\infty}^{+\infty}\rho_1(E)\rho_2(E+eV)T(E)[f(E)-f(E+eV)]dE_x \tag{2-3}$$

Here $\rho_1(E)f(E)$ is the number of occupied states on the left side at energy *E*, $\rho_2(E+eV)f(E+eV)$ is the is the number of occupied states on the right side at energy $E+eV$, $\rho_1(E)$ and $\rho_2(E+eV)$ each is the density of states (DOS) at energy E and $E+eV$ in left- and right-side electrodes, $f(E) = \frac{1}{1+e^{E/k_BT}}$ and $f(E+eV) = \frac{1}{1+e^{E+eV/k_BT}}$ are the Fermi-Dirac distribution functions representing the occupied states where k_B is the Boltzmann's constant and *T* is the temperature.

In a realistic FTJ, three different charge transport mechanisms: direct tunnelling, Fowler-Nordheim tunnelling and thermionic injection (Figure 2.5), can account for the observed tunnelling current depending on the applied voltage amplitude, barrier thickness, etc. Next, we briefly review these possible electric transport mechanisms in FTJs following Pantel et al.'s analysis.[18]

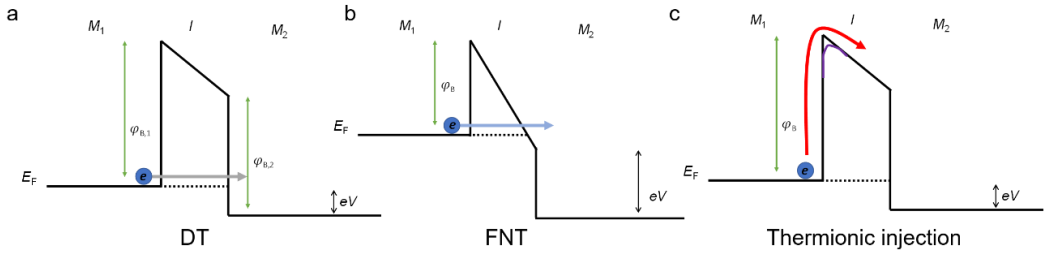

Figure 2.5: Transport mechanisms for an FTJ at the applied bias. (a) Direct tunnelling. (b) Fowler-Nordheim tunnelling and (c) thermionic injection, the purple curve highlights the image force lowering.

-Direct tunnelling

In an FTJ with the ferroelectric insulator layer sufficiently thin and maintaining the ferroelectric spontaneous polarisation, the electrons can directly tunnel through the potential barrier. Due to the existence of depolarisation field and different screening length of the two metal electrodes,[19] the interfacial barrier heights $\varphi_{B,1}$ and $\varphi_{B,2}$ are not the same. In this case, the asymmetric potential is normally termed as trapezoidal. Using the current density J_{DT} given by Gruverman et al.[20] which is based on the analysis of Brinkman et al.[17] and with the WKB approximation, we have:

$$J_{\mathrm{DT}} = \mathrm{C}\frac{exp\left\{\alpha(V)\left[\left(\varphi_{\mathrm{B},2}-\frac{eV}{2}\right)^{\frac{3}{2}}-\left(\varphi_{\mathrm{B},1}+\frac{eV}{2}\right)^{\frac{3}{2}}\right]\right\}}{\alpha^2(V)\left[\left(\varphi_{\mathrm{B},2}-\frac{eV}{2}\right)^{\frac{1}{2}}-\left(\varphi_{\mathrm{B},1}+\frac{eV}{2}\right)^{\frac{1}{2}}\right]^2} \times \sinh\left\{\frac{3}{2}\alpha(V)\left[\left(\varphi_{\mathrm{B},2}-\frac{eV}{2}\right)^{\frac{1}{2}}-\left(\varphi_{\mathrm{B},1}+\frac{eV}{2}\right)^{\frac{1}{2}}\right]\frac{eV}{2}\right\} \quad (2\text{-}4)$$

Here $C = -(4em_{eff})/(9\pi^2\hbar^3)$ and $\alpha(V) = [4d(2m_{eff})^{\frac{1}{2}}]/[3\hbar(\varphi_{B,1} + eV - \varphi_{B,2})]$, m_{eff} is the effective tunnelling electron mass, *e* is electron charge. For the situation where the applied voltage is low that $\varphi_{B,i} \gg \frac{eV}{2}$ (i = 1, 2), the tunnelling current is almost linear with respect to the applied bias and thus practically the electroresistance of the junction can be derived at this voltage regime.

-Fowler-Nordheim tunnelling

At relatively high voltage, Fowler-Nordheim tunnelling (FNT) starts to dominate the charge transport in the tunnel junction. In this situation, the effective barrier potential is modified as the voltage is higher than the interfacial barrier height. Therefore, in FNT the electrons tunnel through a triangular-shaped potential barrier at the electric field *E* as shown in Figure 2.5b. The FNT current is given by:[21]

$$J_{FNT} = \frac{e^3 m_e}{8\pi h m_{eff} \varphi_B} E^2 \exp\left(-\frac{8\pi\sqrt{2m_{eff}}}{3he}\frac{\varphi_B^{\frac{3}{2}}}{E}\right) \quad (2\text{-}5)$$

with $\varphi_B$is the barrier potential, m_e is the electron mass.

-Thermionic injection

Charge carriers can have the finite probability to overcome the potential barrier by thermal energy at non-zero temperatures. As can be seen from Figure 2.5c, the potential barrier is modified by image force lowering, as the image carriers build up a potential at the metal/ferroelectric (wide bandgap semiconductor) interface. This process can be described by thermionic injection (TI) for sufficient applied voltage which is higher than $3\,K_BT/e$:

$$J_{TI} = A^{**}T^2 \exp\left[-\frac{1}{K_B T}\left(\varphi_B - \sqrt{\frac{e^3 E}{4\pi\varepsilon_0\varepsilon_{ifl}}}\right)\right] \quad (2\text{-}6)$$

where A^{**} is the effective Richardson's constant which depends on the material itself, ε_{ifl} is the permittivity of the barrier material responsible for the image force lowering.

2.2.2 Resistance switching in ferroelectric tunnel junctions

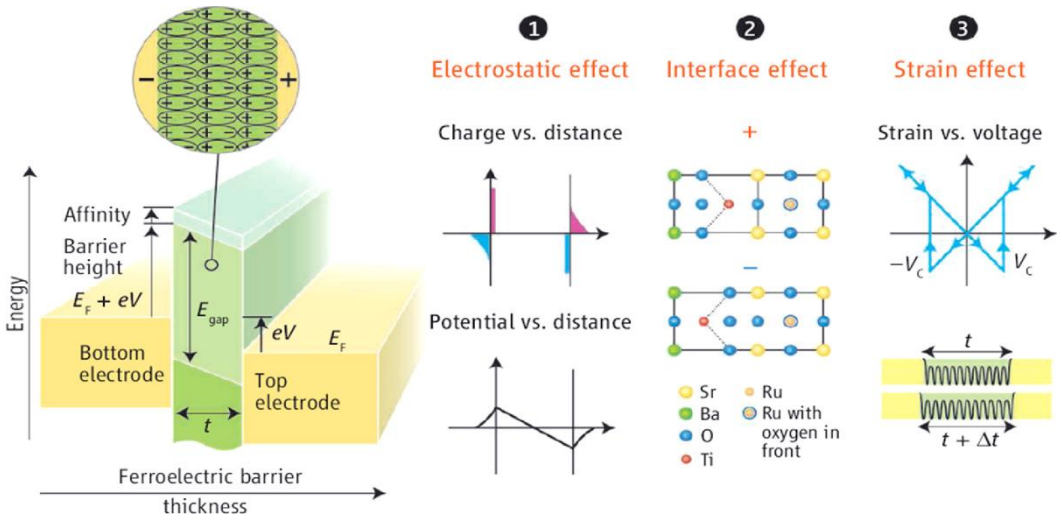

Figure 2.6: The concept of an FTJ and the mechanisms accounting for the tunnelling resistance. Adapted from the reference [23].

As introduced before, an FTJ consists of a thin ferroelectric layer sandwiched by two electrodes. The resistance states of FTJs can be reversibly changed by switching the polarisation direction in the ferroelectric barrier. Similar idea of a resistive switching tunnel junction device using ferroelectric barrier was proposed almost 50 years ago by Esaki et al., which was conceptualised as 'polar switch'.[22] However, this idea was not realised due to the experimental obstacles of obtaining high-quality ultrathin ferroelectric films and poor understanding of ferroelectric behaviours at thin thickness allowing the occurrence of tunnelling. As mentioned in section 2.1.2, the development of oxide thin film fabrication technique now allows people to obtain ferroelectric thin films showing stable polarisation at thickness of 1 nm and therefore pave the way for the prosperity of the research of FTJs.

The concept of an FTJ as developed by Tsymbal et al. is shown in Figure 2.6.[23] In an FTJ, the resistance change between two ferroelectric polarisation states is termed as tunnelling electroresistance (TER):

$$TER = \frac{R_{OFF} - R_{ON}}{R_{ON}} \quad (2\text{-}7)$$

where R_{OFF} and R_{ON} each represents the high and low resistance state in the FTJ. As summarised in Figure 2.6, three most important mechanisms could contribute to the TER in an FTJ.

-Electrostatic effect

As mentioned before, the depolarisation field pointing oppositely to the polarisation direction exists in an FTJ due to the finite screening length of the metal electrode. In an FTJ with metal electrodes of different screening lengths, the electrostatic potential profile associated with the depolarisation field is asymmetric for the opposite polarisation directions. Therefore, the average barrier height seen by the tunnel electrons is different for opposite polarisations, which consequently leads to the TER.[19]

-Interface effect

During polarisation switching, the ion displacement occurs in the ferroelectric oxides at the atomistic scale, which can induce asymmetric atomic position changes at the top and bottom ferroelectric/electrode interfaces.[24] The resultant asymmetric electronic structure changes at the interfaces can therefore lead to the variation of the transmission probability of charge tunnelling across the ferroelectric barrier and thus the TER.[25, 26]

-Strain effect

The strain effect is due to the converse piezoelectric effect since all ferroelectrics also exhibit piezoelectricity. Depending on the direction of the applied electric field with respect to the ferroelectric polarisation, the thickness of the ferroelectric layer could increase or decrease which thus causes the change of the tunnelling potential barrier. Owing to the strain changes accompanying the polarisation reversal, the FTJ must also present a hysteretic current-voltage behaviour and thus resistive switching.[27] However, we note that in the situation that the ferroelectric polarisation

is aligned to the electric field at high voltage regime ($V > V_c$), the resistance change does not happen. On the other hand, the mechanical strain can be also used to change the ferroelectric properties and modify the TER behaviours which could be useful for applications in agile mechanical sensors.[28]

2.2.3 Memristive behaviours

In general, memristive behaviour refers to that the system resistivity is permanently changed in response to a set of external stimuli such as voltage, current, light and so on.[29-31] In realistic ferroelectrics, owing to the energy constraints and local material properties such as defects, the polarisation switching does not occur homogeneously but involves the domain nucleation, growth and expanding.[7, 32] By applying voltage pulse with suitable duration and amplitude, the ferroelectric multidomain configuration can be established rather than the uniform domain state.[33] In principle, as the depolarisation energy for multidomain state is smaller than it in monodomain state, the multidomain state could exist stably. Moreover, in the strained ferroelectric ultrathin films, the 180° domains will be favoured due to that the polarisation being constrained to the energetically preferential directions. By considering each domain as a separate conducting channel and the junction resistance as an average contribution of all the channels (domains), we can thus expect that the domain evolution as a function of the applied voltage can result in the memristive resistance behaviours in FTJs. A representative example can be found in a recent work by Chanthbouala et al, which is summarised in Figure 2.7.[5] Clearly, the FTJ resistance can be driven into multiple states corresponding to the ferroelectric domain configuration and therefore can be regarded as a memristive system or memristor.

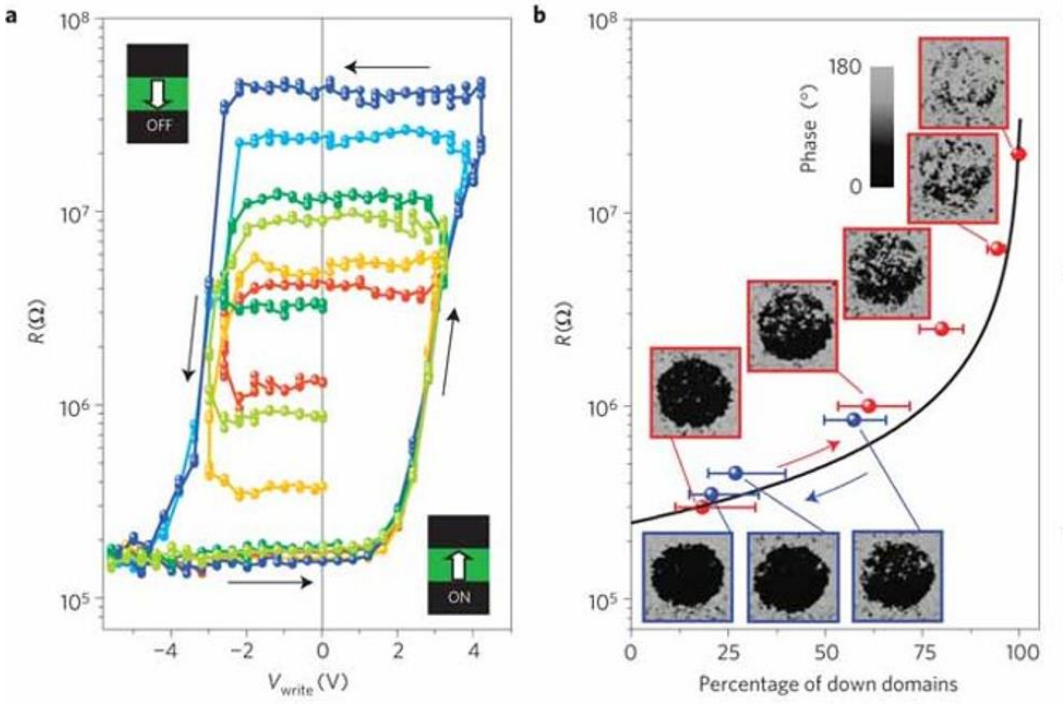

Figure 2.7: Memristors based on FTJs. (a) The hysteretic resistance switching as a function of the applied voltages. (b) The resistance variation corresponding to the virtualised domain evolution. Adapted from the reference [5].

2.3. Spin-dependent tunnelling with ferroelectric tunnel junctions

2.3.1 Tunnelling magnetoresistance in magnetic tunnel junction

Since the first report of large and reproducible tunnelling magnetoresistance (TMR) in 1995,[34] the research on magnetic tunnel junctions (MTJs) has been immensely active in order for the high-performance information storage applications. Similar to the structure of ferroelectric tunnel junction, insertion of a thin insulating layer between two ferromagnetic electrodes forms an MTJ. In an MTJ, two distinct resistance states can exist corresponding to parallel and antiparallel magnetisation orientation alignments between the top and bottom ferromagnetic electrodes (see

Figure 2.8a), which gives rise to the TMR.[35] Note that we assume in Figure 2.8a that the ferromagnetic electrodes are with different coercive field. Further on, a detailed illustration of the mechanism accounting for the TMR in an MTJ is presented in Figure 2.8b. Due to the ferromagnetic electrodes, the tunnelling electrons are spin polarised as determined by the spin-dependent density of states (DOS) of the majority and minority electrons at the Fermi level of the ferromagnetic electrodes. In the tunnelling process, the tunnelling of majority-spin and minority-spin electrons can be regarded as independent from each other. Moreover, the electrons of one spin state from the first ferromagnetic layer will only be accepted by the empty states of the same spin state in the counter ferromagnetic electrode. Following these assumptions, we can conclude that the tunnelling probability is highest when the magnetisations in the electrodes are parallelly aligned, and lowest for the situation that electrodes are with antiparallel magnetisation moments. Following Julliere's model,[35] consider that the conductance of a specific spin state is simply proportional to the DOS of the ferromagnetic electrodes, the TMR is given as:

$$TMR = \frac{R_{ap} - R_p}{R_p} = \frac{2P_1P_2}{1 - P_1P_2} \tag{2-8}$$

where R_{ap} and R_p denote the resistance of MTJ at parallel and antiparallel magnetic moment alignment, respectively. P_i present the spin polarisation at the barrier and ferromagnetic layer interface (i =1, 2 for the first and second electrode).

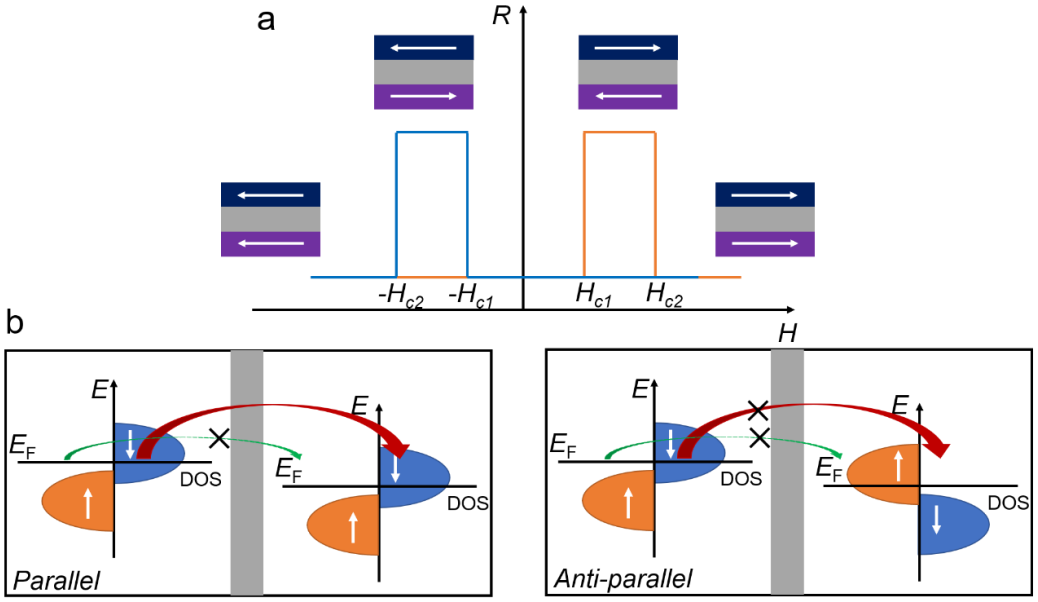

Figure 2.8: Schematic illustration of the TMR in an MTJ. (a) The typical resistance evolution in an MTJ while sweeping the magnetic field. The resistant states are decided by the parallel or antiparallel magnetisation moments in ferromagnetic electrodes. The two ferromagnetic layers are of different coercive fields. (b) Band structure illustrating the spin-polarised tunnelling process for parallel (left) and antiparallel (right) magnetisation alignment.

2.3.2 Electric-controlled tunnelling magnetoresistance in multiferroic tunnel junction

From the application point of view, low-power consumption electric writing operation of MTJs is highly required.[36] The breakthrough is expected to be realised in multiferroic materials/systems which could present both ferromagnetic and ferroelectric order parameters.[37, 38] An intriguing example would be the electric control of TMR in multiferroic tunnel junctions (MFTJs). By replacing the normal insulating layer with a ferroelectric barrier in an MTJ, various resistance states simultaneously corresponding to the electric and magnetic fields can be enabled through exploiting the coupling between ferroelectricity and ferromagnetism. Such a heterostructure is thereby called as an MFTJ (ferroelectric and ferromagnetic).

The first demonstration of such a device is based on a multiferroic tunnel barrier $La_{0.1}Bi_{0.9}MnO_3$ (LBMO) as reported by Gajek et al.[39] The ferroelectric and ferromagnetic nature of LBMO allows for the four memory states based on the combination of TER and spin-filtering effect of the tunnel barrier. This kind of junction is termed as intrinsic MFTJ as the magnetization-polarisation parameters of the barrier determine the transport behaviours.

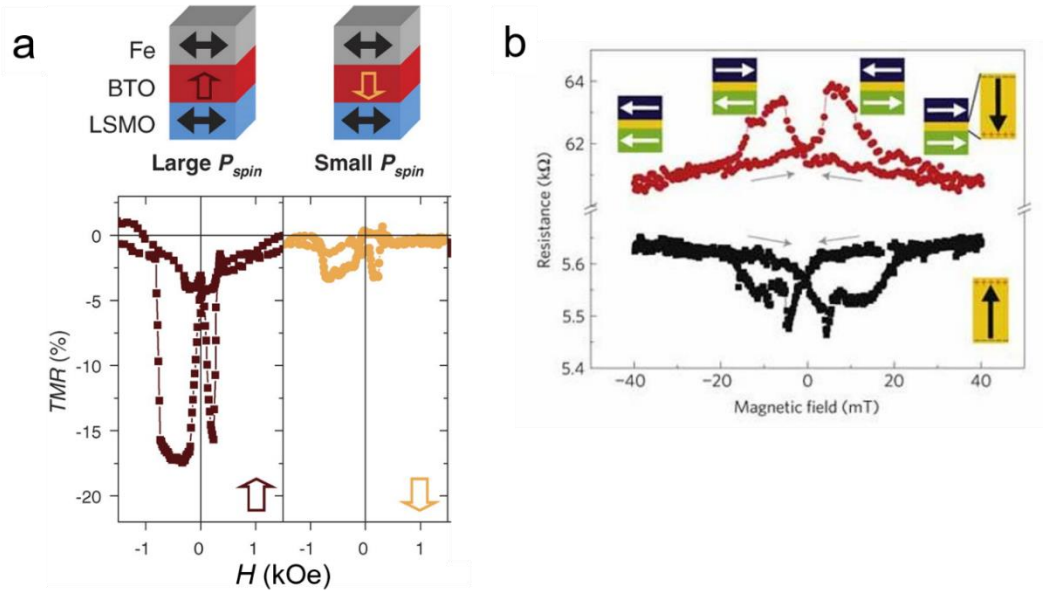

Figure 2.9: Electric control of TMR in MFTJs. (a) Modulation of the TMR amplitude in a $Fe/BaTiO_3/La_{0.7}Sr_{0.3}MnO_3$ MFTJ. Adapted from the reference [6]. (b) Reversible switching of TMR in $Co/Pb(Zr_{0.2}Ti_{0.8})O_3/ La_{0.7}Sr_{0.3}MnO_3$ MFTJs. Adapted from the reference [41].

Later on, the artificial MFTJ was reported by integrating junction in the form of ferromagnetic electrode/ferroelectric tunnel barrier/ferromagnetic electrode.[40] Due to the coexistence of TMR and TER, these MFTJs are also expected to show four memory states in the response of both magnetic and electric fields. Compared to the intrinsic MFTJ, the separation of ferromagnetic and ferroelectric materials in artificial MFTJs can bring higher flexibility to the material selection and may enable emerging properties through the coupling at the ferroelectric/ferromagnetic interface.[24] For example, the strong modulation and even reversal of the spin

polarisation in MFTJs have been reported,[6, 41] see Figure 2.9. These phenomena are attributed to the interfacial magnetoelectric coupling between the ferroelectric and ferromagnetic layers, and further researches based on the microscopic investigations suggested the induced magnetic character in the ferroelectric interfacial layer namely the interfacial multiferroicity.[42]

2.4 Photovoltaic effect in ferroelectrics

2.4.1 Basics

Photovoltaics refers to the conversion of light into electricity using materials in which the charge carriers can be excited to a higher energy state upon photon absorption. In conventional semiconducting materials like Si, the photogenerated charge carriers are separated by the internal field developed at the interface such as p-n junction and Schottky barrier in which the open-circuit photovoltage is restricted by the energy barrier height and does not exceed the bandgap.[43, 44] In ferroelectrics, unique photoresponse that is called as bulk photovoltaic (BPV) effect was observed, which can exhibit steady-state photocurrent at zero bias with light illumination on the homogeneous medium and above-bandgap open-circuit photovoltage.[45] Those properties make the BPV effect different from that with the conventional inhomogeneous excitation medium.

Pioneering work back in 1970 has evidenced that such an unconventional photovoltaic effect is related to the non-centrosymmetric nature of crystal structure, which exists in crystals belonging to 20 point groups that lack a centre of inversion symmetry, e.g. piezo-, pyro- and ferroelectric materials.[46, 47] The mechanism of the BPV effect is associated with the photon excitation in a non-centrosymmetric crystal of the nonthermalized (hot) carriers, leading to asymmetric distribution of nonthermalized carrier momentum.[46] The existence conditions of the BPV can be described using the theory developed by Ruppel et al. based on the Boltzmann transport equation and analysis about the asymmetry in *k*- and *r*-space responsible for photovoltaic voltage generation.[48] To generate the steady-state photocurrent, the

distribution of electrons in space *r*, momentum *k* and time *t* can be described by the distribution equation:

$$\frac{\partial f}{\partial t} + \upsilon_k \nabla_r f - \frac{eE}{\hbar} \nabla_k f = G + R + S \tag{2-9}$$

here *E* is the electric field which can be written by introducing the electric potential φ:

$$E_k = -\nabla_r \varphi(r, t) \tag{2-10}$$

υ_k is the velocity of an electron:

$$\upsilon_k = \frac{\nabla_k \varepsilon_k}{\hbar} \tag{2-11}$$

where ε_k is energy of the electron in the electron-originated band. In equation 2.9, the term $\upsilon_k \nabla_r f$ represents the diffusion current as a consequence of the spatial variation of the carrier concentration and $\frac{eE}{\hbar} \nabla_k f$ term stands for the electric field induced drift current. On the right side of equation 2.9, the collision integral describes the carrier generation with rate *G*, recombination due to electrons and holes transitions with rate *R*, and scattering with the rate *S* among the same type of carriers.

Next, we can write the distribution function *f* while in thermodynamic equilibrium using the time independent Fermi distribution as:

$$f_{eq}(r, k) = f_{eq}(\varepsilon_k - E_F) = \frac{1}{1 + e^{\varepsilon_k - E_F / k_B T}} \tag{2-12}$$

where E_F is the Fermi level. When $f_{eq}(k) = f_{eq}(-k)$, the distribution function is symmetric as in thermodynamic equilibrium, therefore there will be no current as can be seen from equation 2.12. An electric current generation requires an asymmetric part $f^{as}(r, k)$ in the distribution function, thus the current $J(r)$ can be given by considering the volume *V*:

$$J(r) = -\frac{2 \sum_k e \upsilon_k f^{as}(r,k)}{V} \tag{2-13}$$

Under light excitation, external perturbation can be introduced into equation 2.12

and a new distribution function $f_{ph}(r,k)$ with the term $\partial f(r,k)$ representing the change due to the perturbation can be deduced as:

$$f_{ph}(r,k) = f_{eq}[\varepsilon_k - E_F(r)] + \partial f(r,k) \tag{2-14}$$

Due to the fact that the current can be only carried by $\partial f(r,k)$, the optical generation rate $G_{opt}(r,k)$ can then be expressed as:

$$\partial f(r,k) = \tau G_{opt}(r,k) + \frac{\partial f_{eq}(r,k)}{\partial E} \upsilon_k \nabla_r E_F(r) \tag{2-15}$$

here τ is the relaxation time for the carrier from excited state back to the equilibrium. From 2.14, the asymmetric part $f^{as}(r,k)$ can be introduced through the non-symmetric optical excitations in *k* space. In non-centrosymmetric crystals with a polar axis, and under the circumstances that the carrier recombination process is different from generation process and $G_{opt}(k)$ does not equal $G_{opt}(-k)$, we can write:

$$\partial f^{as}(k) = \frac{\tau}{2}[G_{opt}(k) - G_{opt}(-k)] \tag{2-16}$$

A schematic illustration of the photoexcitation process in non-centrosymmetric and centrosymmetric materials can be found in Figure 2.10. Qualitatively speaking, the BPV effect exists in materials with non-centrosymmetric crystal structure and the carrier recombination process must be different from the carrier excitation process.[46, 48]

In ferroelectric materials, the BPV can be described phenomenologically as:

$$J_{ph} = I_{photo}\beta_{ijk}e_j e_k \tag{2-17}$$

As indicated by equation 2.17 the photocurrent J_{ph} generated in ferroelectrics under the linear polarised light with intensity of I_{photo} will depend on the third rank BPV tensor β_{ijk}, and the terms e_j and e_k which present the projections of electric field of light on the plane of the sample. Hence, it can be concluded from equation 2.17 that the photocurrent induced by BPV effect is not related to the ferroelectric polarisation direction and can be controlled by the light polarisation.[49] As for the

open-circuit photovoltage, considering the gap distance d between the collecting electrode pairs, we can write:

$$V_{oc} = \frac{J_{ph}}{\sigma_{dark}+\sigma_{ph}} d \tag{2-18}$$

Clearly, the giant open-circuit photovoltage in ferroelectrics is due to the super low conductivity of the crystal under dark σ_{dark} and illumination σ_{ph}, respectively.[49]

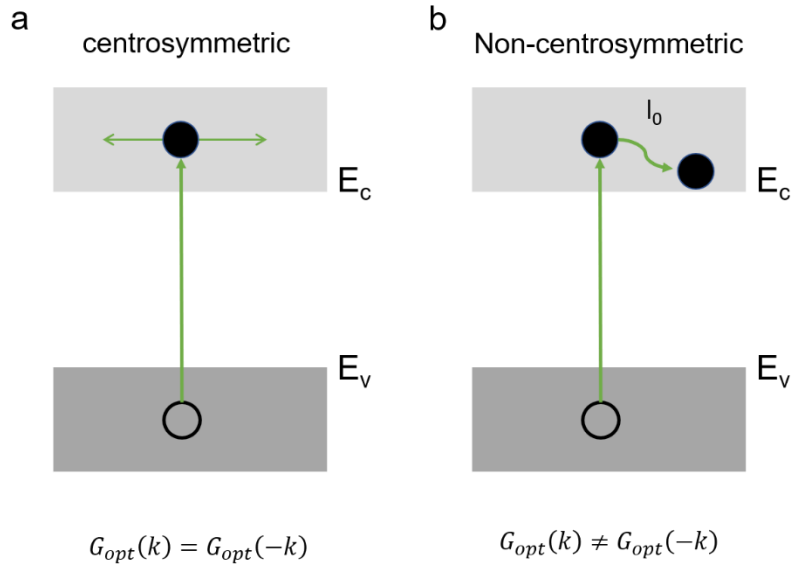

Figure 2.10: Photoexcitation process in centrosymmetric (a) and non-centrosymmetric materials (b).

2.4.2 Tip-enhanced photovoltaic effect

The tip-enhanced photovoltaic effect was first reported by Alexe et al. in bismuth ferrite single crystal.[50] In their work, it is shown that photoexcited carriers can be efficiently collected and the external quantum efficiency can be enhanced by up to seven orders of magnitude by using a nanoscopic contact rather than conventional macroscopic electrodes. Although the physical origin of this effect might be still at debate,[51] another important perspective implied by this work, namely the electric field distribution at the nanoscopic hemispheric tip (~30 nm in radius) beside the focus on energy harvesting using the tip-enhanced BPV effect has attracted increasing interests. As theoretically explored by Sturman et al,[52] the photocurrent

in short-circuit model can induce a non-zero electric field which can be strongly enhanced with reducing the top electrode size. Moreover, it is theoretically analysed that this local photocurrent induced electric field could be sufficient to repolarise the polarisation of the ferroelectric crystal near the top electrode depending on the contact size and crystal thickness. These results thus make one wonder if the tip-enhanced BPV effect can be utilised for electric control of polarisation of ferroelectrics, especially at the nanoscale?

2.5 Flexible single-crystalline ferroelectric oxides: state of the art

Compared to conventional rigid substrate hosted electronic devices, flexible electronics which show excellent mechanical flexibility are undergoing a rapid development due to their considerable potential in new device concepts.[53] It has been regarded as the next ubiquitous platform which can accommodate a wide range of electronic applications as shown in Figure 2.11. The functioning component in a flexible system is the key part which dominates the device performance. Upon the realistic requirements of various applications, materials including but not limited to organic semiconductor polymers,[54, 55] inorganic semiconductors,[56] 2D layered materials[57, 58] have been exploited serving as the functional component. However, functional oxide thin films which present a broad spectrum of fascinating properties such as piezoelectricity,[59] high temperature superconductivity,[60] multiferroicity,[61] colossal magnetoresistance,[62] conducting interface,[63] etc., have rarely been considered for those flexible systems. The main reason is related to the fact that it is difficult to directly grow single-crystalline functional oxide films on the main-stream plastic flexible substrates, because plastics normally decompose at the high crystalizing temperature of the oxide films (~600 °C).

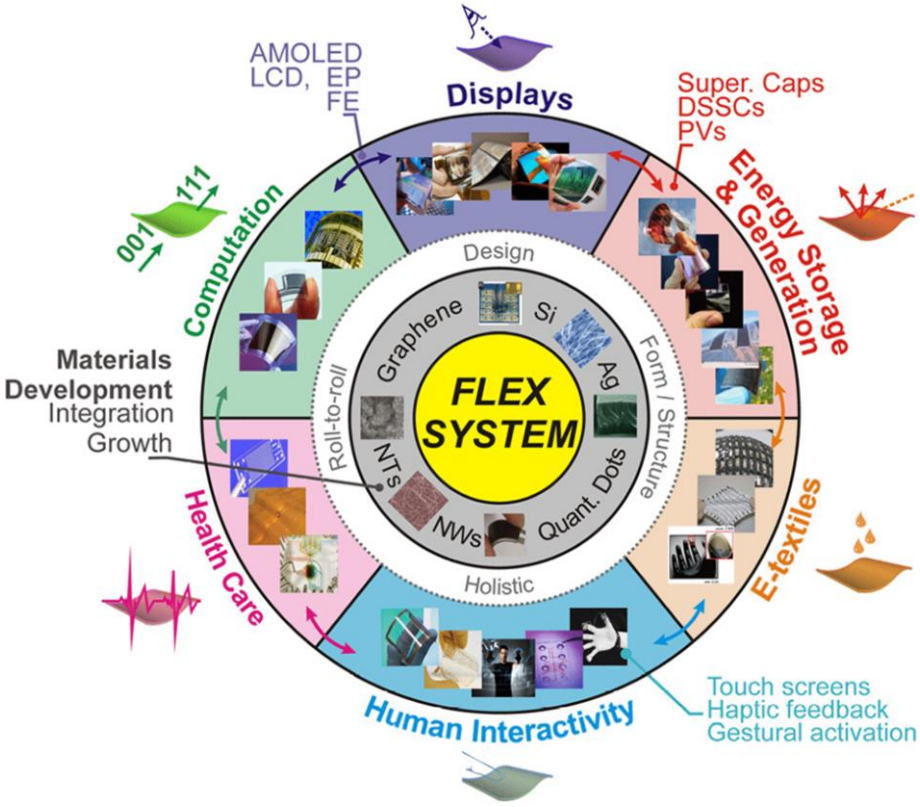

Figure 2.11: A representative schematic showing the potential applications and materials used for the flexible electronics. Adapted from reference [53].

Very recently, rapid progress on flexible functional oxide devices have been made especially on the single-crystalline ferroelectrics due to their wide applications on non-volatile memories,[2, 3] sensors,[64] etc., which are promising to add an important building block to flexible electronics. In this section, we present a brief overview of the status quo of flexible functional oxides with the focus mainly on single-crystalline ferroelectrics. We note that although the flexible ferroelectrics have been realised many years ago, the materials used before were mainly organic ferroelectrics like polyvinylidene fluoride (PVDF)-based polymers[65] or sol-gel derived polycrystalline ferroelectric oxides like lead zirconate titanate (PZT) on soft stainless-steel foil,[66] which underperform in terms of inferior ferroelectric properties or much higher coercive field compared to those of single-crystalline ferroelectric films.[67, 68]

Two main strategies have been extensively explored to obtain flexible single-crystalline ferroelectric oxides: (I) direct growth through van der Waals (vdW) oxide epitaxy;[67] (II) 'grow-transfer' by selective etching.[69]

-Van der Waals oxide epitaxy

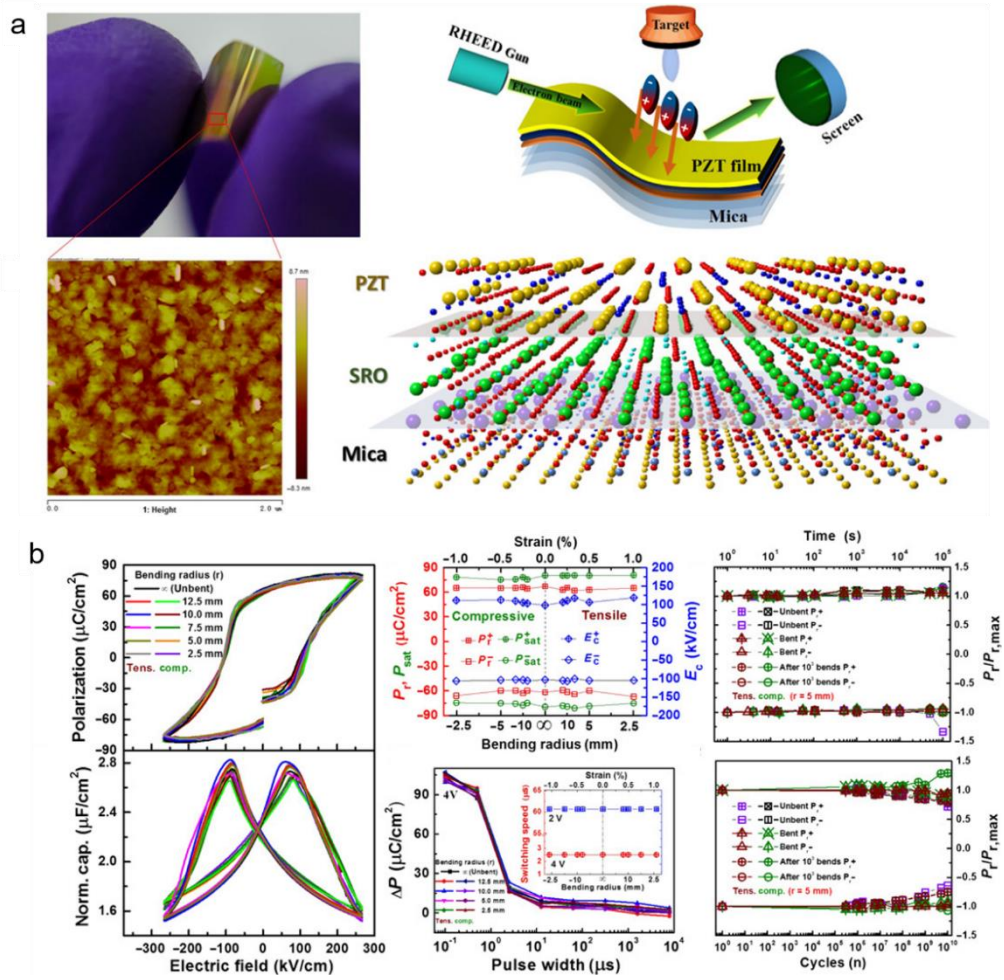

Figure 2.12: Epitaxial PZT on Mica. (a) The optical image, topography and growth method of the flexible PZT capacitor. (b) Summaries of the ferroelectric performance. Adapted from reference [73].

The vdW epitaxy has been demonstrated as a powerful method to grow epitaxial layers without the requirement to satisfy lattice mismatch between the substrate and the grown material.[70-72] Recently, this idea has been expanded to the fabrication of single-crystalline functional oxide thin films. A representative work is the

successful fabrication of high-performance PZT ferroelectric epitaxial layer on $SrRuO_3$ (SRO) buffered Mica substrate.[73] As shown in Figure 2.12, the obtained PZT/SRO/Mica heterostructure is highly flexible and bendable. Through the electric characterisations, the PZT thin films exhibit superior ferroelectric properties with high saturated and remnant polarisations. Moreover, the Mica based flexible ferroelectric capacitors demonstrate excellent retention and fatigue endurance and are stable against the shape changes. These results suggest that the Mica-based ferroelectric oxide thin films can present similar functional performance compared to those rigid single crystal hosted thin films, and are with the desired extra functionality-mechanical flexibility. Following this route, a series of epitaxial oxide films based multifunctional flexible applications even beyond ferroelectrics have been studied such as strain tuneable metal-insulator transition in Mott insulator,[74] piezoelectric energy harvester,[75] resistive switching memory,[76] strain-tunable microwave ferromagnetism device.[75] However, it must be noted that the orientation of the film is not controlled by the vdW material based substrate, for example: PZT grows along [111] direction on (*00l*)-oriented Mica and the grown film cannot be freely transferred to other desired surfaces like transferable nanomembranes do.

-Grow-transfer method

Using the grow-transfer method, the epitaxial layers can be of any orientation by selecting the proper substrates and transferred to any foreign substrates after lift-off. The idea of this method relies on the insertion of a sacrificial layer between the substrate and the thin film of interest. After removing the sacrificial layer, the desired thin film can be lifted off to form the nanomembrane (i.e. monocrystalline structure with thickness lower than a few hundred nanometres and with the lateral dimensions at least two orders of magnitude larger than the thickness),[77] and transferred onto any new substrates. A recent example of using this method to make ferroelectric flexible devices was reported by Bakaul et al.,[69] the key results are shown in Figure 2.13. They obtained the SRO/PZT/SRO nanomembranes by

selectively etching the LSMO sacrificial layer and lifting off from the STO substrate. As can be seen from Figure 2.13, the obtained SRO/PZT/SRO heterostructure preserves the single-crystalline structure after placed on the PET substrate and exhibit superior ferroelectric properties. Using the same method, the authors also managed to transfer oxide nanomembranes on Si substrates.[78] Moreover, due to the vast archive of single-crystal substrates for oxide films, oxide nanomembranes of different orientations and crystal structures can be obtained by choosing the proper substrates. This feature can further enhance the multifunctionality of these oxide nanomembranes as it is known that the crystal structure of functional oxide films can lead to novel properties.[79, 80] Therefore, compared to the vdW oxide epitaxy, the grow-transfer method could provide advantages in production of ferroelectric oxide nanomembranes with various crystal structures and integration with arbitrary surfaces which may further lead to bio-compatible systems.

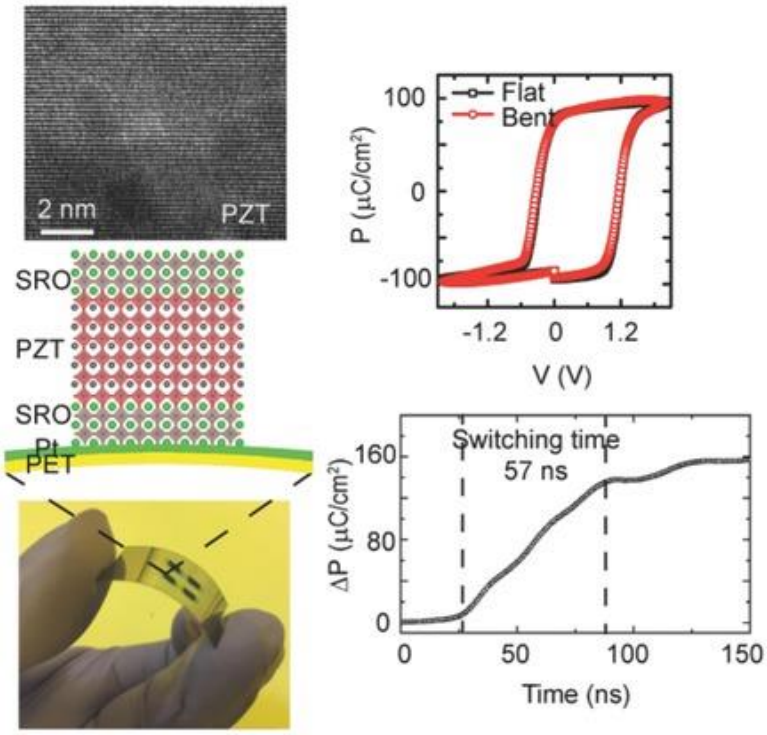

Figure 2.13: Epitaxial PZT based structure on PET. Adapted from the reference [69].

2.6 Summary

With FTJ-based novel devices being the focus of this Thesis, we discussed the ferroelectricity, perovskite oxides that are exclusively used in this work and ferroelectric polarisation- and spin-dependent charge tunnelling phenomena which will be useful to understand the results of the FTJs. As the exploration of multifunctional devices based on FTJs being another key point of the work, we further presented brief introduction to ferroelectric photovoltaics and the emerging flexible ferroelectric devices.

Chapter 3

Materials and experimental methods

In this Thesis, a considerable part was devoted to the thin film growth and characterisation. Thereby, this chapter will first present all the used materials with the focus on their structure information and the growth methods used in this work. Except the metal layers which were used as the electrodes, all the samples were made from perovskite oxide thin films by pulsed laser deposition. Using photolithography, different devices were made from these films. A variety of experimental tools were used to characterise the samples ranging from structure investigation equipment to electric/magnetic measurement facilities. X-ray diffraction and transmission electron microscopy were used for structure investigation of the samples. Local properties of thin films including topography, ferroelectric domain structure and conducting states were acquired by atomic force microscopy-based system. Electric transport and magnetic characteristics were measured using different types of magnetometer and electronic facilities. In this chapter, the working principles and major setup of these equipment will be briefly introduced, which can be helpful to understand the experimental results.

3.1 Thin film growth

3.1.1 Pulsed laser deposition

Pulsed laser deposition (PLD) is a chemical vapour transfer technique which is featured of stoichiometric transfer of laser ablated targets for many complex materials. As triggered by the immense interest in high temperature superconducting thin films, PLD as a simple and reproducible method for in-situ stoichiometric thin film growth especially for high quality oxides films has received renewed attention since 1980s.[81] Nowadays, it has been adopted as an important fabrication technique from laboratory research to industry commercial production for a wide range of materials even beyond oxides.[81, 82] As can be found in Figure

3.1, the basic deposition process of using PLD can be summarised as: when ultrashort (0.1-10 ns) laser pulse with sufficient energy (0.1 -10 J/cm^2) bombards the sintered target, plasma which consists of the atoms/ions from the ablated material travels from the target towards the substrate and deposits the plume species on the substrate to form the film. The key requirement for the PLD is to select a laser with nanosecond pulse width and ultraviolet wavelength that can be strongly absorbed by the target material. Throughout the work, a KrF excimer laser with 248 nm wavelength was used.

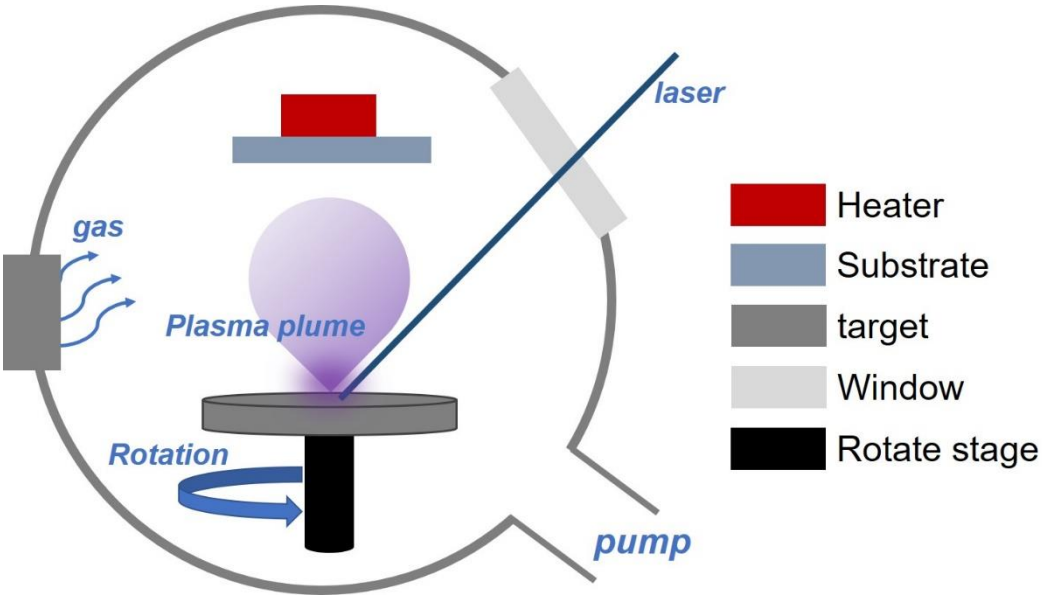

Figure 3.1: Schematic illustration of the configuration a model PLD system.

Several key components of our PLD chamber can be also found in Figure 3.1. The pump system which consists of a mechanic pump and a turbo pump in series can enable an ultrahigh vacuum (below 10^{-6} mbar). Within this vacuum, background gas like oxygen and argon can be introduced into the chamber. During the deposition, the background gas is important as it can serve two purposes. First, participating the chemistry of material growth, for example, O_2 which interacts with the ablated material can provide reactive species in the plume to facilitate the formation of multi-cation phase of complex oxide materials. Second, the background gas can be used to reduce the kinetic energy of the ablated species and

thus control the ablation plume expansion. A rotation stage is adopted for the target to reduce the inhomogeneous area on the target caused by long-time laser ablation. As materials are of their own crystallization temperature, a heater ranging from room temperature to 700 °C is used to set the substrate temperature as desired. Moreover, the distance between the substrate and the target can be adjusted by changing the position of the heater.

3.1.2 Thin film growth modes

In PLD deposition, four kinds of thin film growth modes can occur as depicted in Figure 3.2.[83]

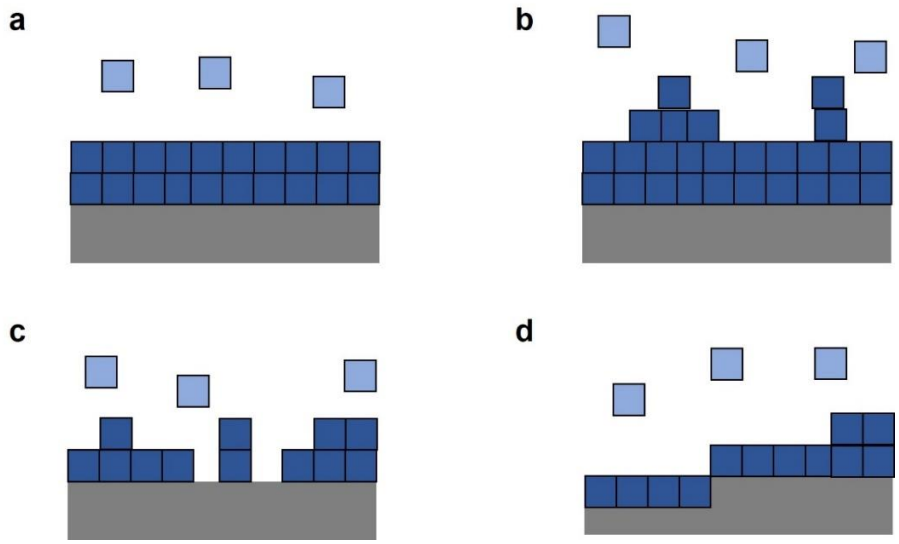

Figure 3.2: Schematic drawing of four different kinds of thin film growth modes using PLD. (a) 2D layer by layer growth (Frank-Van der Merwe); (b) layer by layer to island (Stranski-Krastanov); (c) island growth (Volmer-Weber); (d) step-flow mode.

-Layer by layer growth (Frank-Van der Merwe): adatoms diffuse on the substrate surface, the growth for the overlayer only occurs until a complete layer underneath of the material is formed.

-Layer by layer to island (Stranski-Krastanov): also refers to step-bunching mode, new steps of the material may form before the underneath steps are fully covered

by the material, which thereby lead to bunches of steps.

-Island growth (Volmer-Weber): in order to minimise the total surface energy, the film does not wet the total surface which leads to multiple islands of the materials rather than the continuous 2D layers.

-Step-flow mode: this kind of growth normally occurs on the vicinal surface, atoms diffuse towards steps of the substrate due to the high mobility of the adatoms and the steps propagate during deposition, which enables the layer by layer growth.

These four modes can be controlled through choosing different types of substrates, changing the parameters of the laser and PLD chamber conditions. Achieving the right mode which is crucial for the growth of the high-quality thin films can be challenging, and some important parameters should be considered for optimising the growth: the laser fluency which decides the nucleation rate during film growth; the repetition rate of the laser which controls the film deposition speed; the background gas which can influence the stoichiometry of the film and atoms arrangement kinetics on the substrate surface; the target-substrate distance which decides the growth speed and thickness homogeneity of the thin film; the temperature of the substrate which has strong impact on the kinetic energy of the atoms on the substrate and thus the nucleation behaviours.

3.1.3 Metal film evaporation

E-beam evaporation, which is used for metallic layer deposition serving the purpose of electrode coating in this Thesis, is based on the thermic phenomenon. During e-beam evaporation, the target material used for the coating purpose is bombarded by the electron beam to be heated up and thus converted into the gaseous state for coating on the surface. The e-beam evaporation experiments were conducted using a Scientific Vacuum System (SVS) 8-pocket electron beam evaporator which can reach a ~10^{-7} mbar base pressure.

3.2 Materials

3.2.1 Substrate: $SrTiO_3$

$SrTiO_3$ (STO) is a typical ABO_3 perovskite and of a cubic crystal structure with the lattice constant of 3.905 Å. STO single crystal has been used as the substrate for the growth of a broad spectrum of functional oxide perovskite materials due to the two main reasons: (1) as displayed in Figure 3.3, the lattice constant of STO is close to the in-plane lattice constants of many functional oxide materials;[10] (2) it is possible to obtain the sharp SrO- or TiO_2-terminated surface in STO which is crucial for the high quality oxide film growth.[84] Because that the thin films epitaxially grown on STO are of much thinner thickness compared to that of STO substrate, the unit cell of the overlayer constrained on the substrate will be of tensile or compressive misfit strain state which can be defined as:

$$\delta^{in} = (a_{sub} - a_{film})/a_{sub} \quad (3\text{-}1)$$

where δ^{in} is the in-plane strain state, and a_{sub} and a_{film} are the in-plane lattice constant of the substrate and the film, respectively.

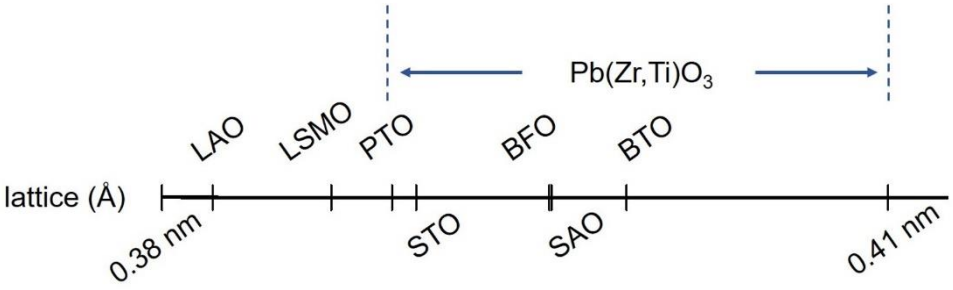

Figure 3.3: Comparison of the in-plane lattice constants of all the perovskite materials used in this Thesis.

In the current work, all the measured samples were grown on commercially available (001)-oriented STO substrates with low-miscut angle. The as-received STO substrates are with mixed termination. In order to obtain single-terminated

STO, we doped chemical and thermal combined treatment before thin film depositions.[85] After standard acetone cleaning process, STO substrates were etched by DI water for 10 min and further by Hydrofluoic acid (HF) for 10 s in order to remove the SrO bonds. Subsequently, the STO substrates were annealed at 950 °C in a N_2 furnace for 1.5 h which resulted in the well-defined single TiO_2-terminated surface. A good example of the treated STO showing the ultra-flat topography with step-and-terrace is displayed in Figure 3.4.

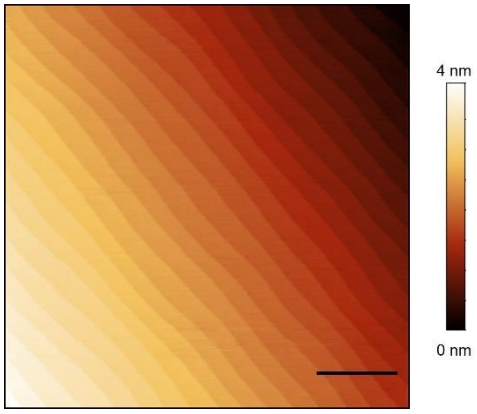

Figure 3.4: Topography of treated STO substrate. Scale bar: 0.5 μm.

3.2.2 Bottom electrode: $La_{1-x}Sr_xMnO_3$

$La_{1-x}Sr_xMnO_3$ is a perovskite oxide which can be tuned from insulating antiferromagnetic to conducting ferromagnetic by varying the Sr doping level. At the optimised composition for ferromagnetic properties, namely x = 0.33, $La_{0.67}Sr_{0.33}MnO_3$ (LSMO) is of high Curie temperature (T_c) of ~370 K and half-metallic with nearly 100% polarisation of the conduction electron spin.[86] Apart from its excellent conductive and ferromagnetic properties (~100% spin polarisation), LSMO can be grown epitaxially on wide range of substrates due to their structure similarity which therefore is considered as a good choice for the electrode in oxide heterostructures especially magnetic tunnel junctions.[87] In bulk, LSMO possesses a rhombohedral unit cell with lattice constant a_r = 5.471 Å and α_r = 60.43°.[88] Upon epitaxially grown on the STO (001) substrate, LSMO is of tensile strain state with the crystal structure becoming pseudocubic of c = 3.846 Å.[89] An

example of 30 nm LSMO grown on STO by PLD is presented in Figure 3.5, the LSMO shows well-defined step-and-terrace surface which is necessary for growing the following high-quality oxide overlayers.

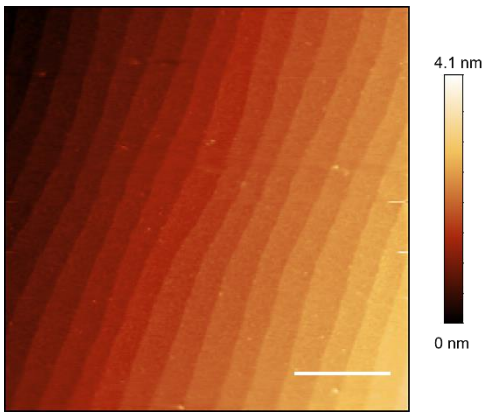

Figure 3.5: Topography of a 30 nm LSMO grown on STO (001) substrate. Scale bar: 0.5 μm.

3.2.3 Ferroelectric barrier: $BaTiO_3$, $PbTiO_3$ and $PbZr_{0.2}Ti_{0.8}O_3$

Three different kinds of perovskite ferroelectric oxide materials were used as the ferroelectric barrier for ferroelectric tunnel junctions in this work. They are all of typical ABO_3 crystal structure as presented in Figure 2.2 section 2.1.1. As discussed in section 2.1.1, ferroelectricity in these materials arises from the displacement of B-site atom (Ti or Zr) and oxygen octahedra with respect to the A-site Pb/Ba atoms. Such a displacement results in a stable electric dipole moment in the unit cell along its symmetry axis.[90]

$BaTiO_3$ (BTO) is the first discovered polycrystalline ceramic material that shows ferroelectricity and has attracted intense interest as a model ferroelectric system from research perspective.[91] In bulk, BTO is of a tetragonal crystal structure with $a = b = 3.992$ Å and $c = 4.0361$ Å at room temperature. While cooling down from high temperature, it undergoes the structure transition from paraelectric cubic phase to ferroelectric tetragonal phase at the transition temperature of 131 °C, and further tetragonal-orthorhombic-rhombohedral phase transitions at 0 °C and -90 °C, respectively.[91] Through strain engineering method, i.e., by growing the BTO on

substrates with mismatching lattice parameters, the ferroelectric properties of BTO can be enhanced with higher spontaneous polarisation, remarkably improved T_c and reduced critical thickness maintaining the ferroelectricity.[92, 93]

Lead zirconium titanate ($PbZr_xTi_{1-x}O_3$), a solid solution of $PbTiO_3$ (PTO) and $PbZrO_3$ (PZO) is the most widely used piezoelectric material for electromechanical applications and also used for non-volatile memory cell due to its excellent ferroelectric properties.[91, 94, 95] In this work, we used PTO and $PbZr_{0.2}Ti_{0.8}O_3$ (PZT) as the ferroelectric barrier of ferroelectric tunnel junctions. Note that from the previous work of our group, PZT grown on STO (001) can maintain ferroelectricity even at the thickness of 1.6 nm,[18] therefore could serve as a good candidate for ferroelectric tunnel junctions. For thin film deposition, ceramic targets of 10% Pb excess were used for compensation of the volatile Pb at high temperature.

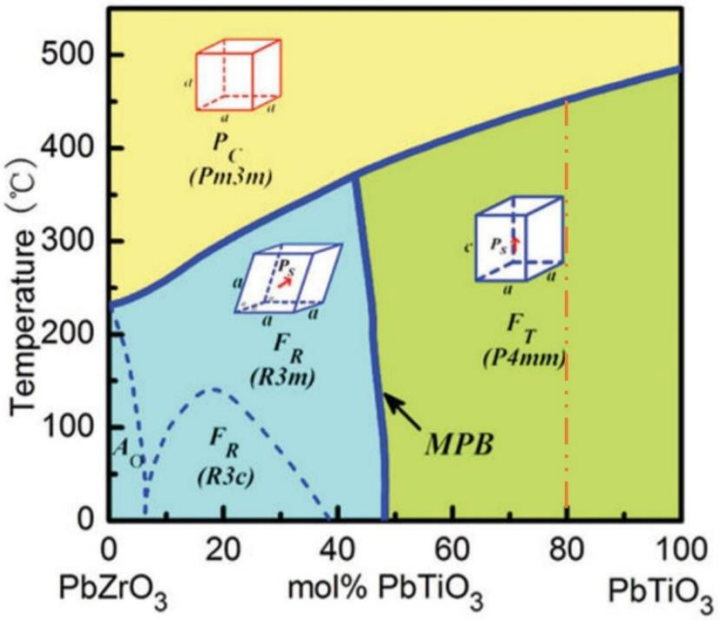

Figure 3.6: Phase diagram of Lead zirconium titanate ($PbZr_xTi_{1-x}O_3$) system. Adapted from the reference [95].

As can be seen from the phase diagram of lead zirconium titanate system (Figure 3.6), due to the low level of Zr doping, the properties of the used PZT (x = 0.2) resemble to that of the PTO. Compared to BTO, PTO and PZT both show much

higher T_c beyond 400 °C and robust ferroelectric polarisation. Unlike BTO which exhibits four different phases with varying temperatures, upon cooling down from high temperature, both PZT and PTO only experience a cubic paraelectric to tetragonal ferroelectric phase transition. At room temperature, lattice constants for bulk PZT and PTO are: a = 3.952 Å / c = 4.148 Å and a = 3.896 Å / c = 4.144 Å, respectively.[96, 97]

3.2.4 Ferroelectric photovoltaic film: $BiFeO_3$

$BiFeO_3$ (BFO) is almost the mostly studied multiferroic system in the past few years owing to its exceptional physical properties ranging from the combination of ferroelectricity with antiferromagnetism to domain wall nanoelectronics.[98-100] The bulk BFO is of rhombohedra crystal structure and exhibits spontaneous polarisation along the oxygen octahedron displacement direction, i.e. pseudocubic [111] direction. The Curie temperature for its ferroelectric order is as high as 825 °C and the Neel temperature for its antiferromagnetic order is around 370 °C. Moreover, being intrinsically a bulk photovoltaic (BPV) material of a favourable bandgap of 2.7 ev which sits in the visible light spectrum, BFO has attracted lots of interests since the recent surge in ferroelectric photovoltaics.[49, 50] The BFO crystal can exhibit large open-circuit photovoltaic voltage and light-polarisation controllable photocurrent,[101] therefore was used as a photovoltaic cell in the hybrid light writable electronic memory devices in Chapter 5. For the growth of BFO thin films, BFO ceramic target was fabricated with intentionally 20% Bi excess to compensate the Bi volatile during high temperature deposition.

3.2.5 Water soluble film: $Sr_3Al_2O_6$

$Sr_3Al_2O_6$ (SAO) is a hygroscopic perovskite oxide with high water solubility.[102] At room temperature, the SAO exhibits a cubic unit cell (space group $pa\overline{3}$) with lattice constant of 15.844 Å which closely matches four unit cells of the STO substrate ($4 \times a_{sto}$ = 15.620 Å) on the in-plane mesh. It has been reported that SAO can be epitaxially grown on STO (001) due to the resemblance of their lattice and

is therefore possible for the growth of other functional oxide overlayers on top of it.[102]

3.2.6 Thin film growth parameters

Growth parameters were found for different oxide thin films and checked by examining the crystal structure, topography and functional properties. Growth conditions for each material were then optimised to give the best quality of thin films. Thin films made using certain numbers of laser pulses were examined by transmission electron microscopy (TEM) to obtain the thickness information, which in return was used to derive the growth rate with respect to the laser pulse number. The detailed growth parameters are summarised in Table 3.1 below.

Material	**Temp. (°C)**	P_{O2} **(mbar)**	**Fluence (J/cm^{-2})**	**Laser rate (Hz)**
BTO	650	0.01	1.5	2
PZT	600	0.2	1	10
LSMO	600	0.15	1	2
BFO	670	0.2	0.5	10
SAO	650	0.005	1.75	1

Table 3.1: Thin film growth parameters of oxides. These conditions remain almost constant for each material grown in the certain PLD chamber.

3.3 Device fabrication

Device pattern and fabrication on these thin films were conducted using UV light photolithography (Suss Microtec MA8) in the yellow room. A standard photolithography process is displayed in Figure 3.7. The oxide thin film (I) is spin-coated with the positive/ negative photoresist and further baked on a heat stage; (II) then exposed to the UV light under a mask with desired device patterns for a certain time allowing the exposed area of the photoresist to be reacted; (III) the film is subsequently immersed into the specific developer in which the development of the

reacted photoresist occurs and leaves the desired pattern of photoresist on the film. Note that positive or negative photoresist leads to the 'disappear' or 'preserve' of the UV exposed areas. After obtained the device pattern, metal film is deposited by the e-beam evaporation on the oxide thin film. The unwanted metal layer on the thin film is 'lift-off' by washing away the photoresist underneath via acetone.

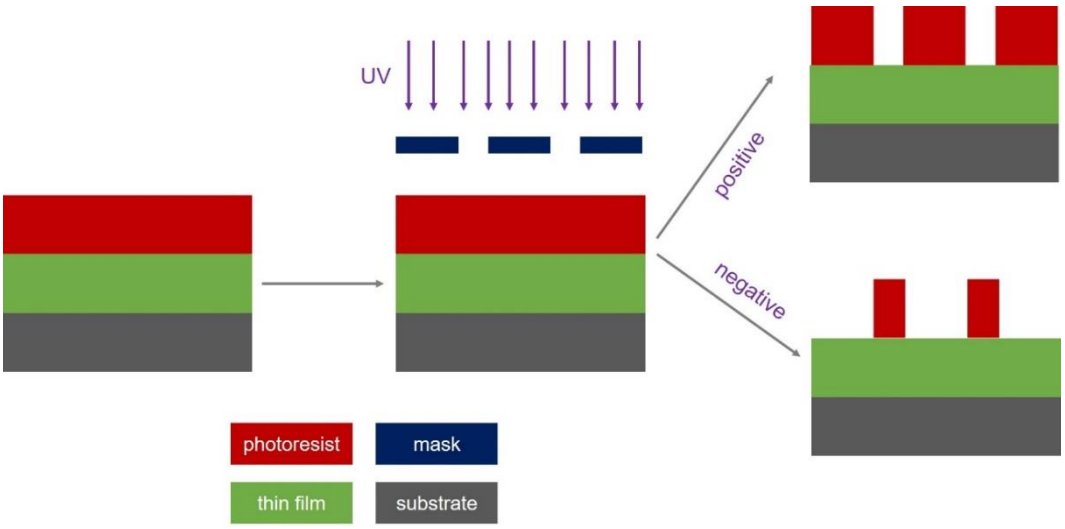

Figure 3.7: Schematic drawing of a standard photolithography process using positive and negative photoresist, respectively.

3.4 Structure investigation

3.4.1 X-ray diffraction

X-ray diffraction (XRD), based on the interactions between the X-ray photons with the electrons surrounding the ion, is one of the most popular techniques to characterise the material in terms of its crystallinity, structure and chemical composition.[103, 104] Due to the fact that the wavelength of the X-ray (1-2 Å) is comparable to the size of an atom, the incident X-ray on the surface of a crystal having a periodic structure can give rise to a coherent diffraction following the Bragg's law:

$$2d_{hkl}sin\theta_{hkl} = n\lambda \qquad (3\text{-}2)$$

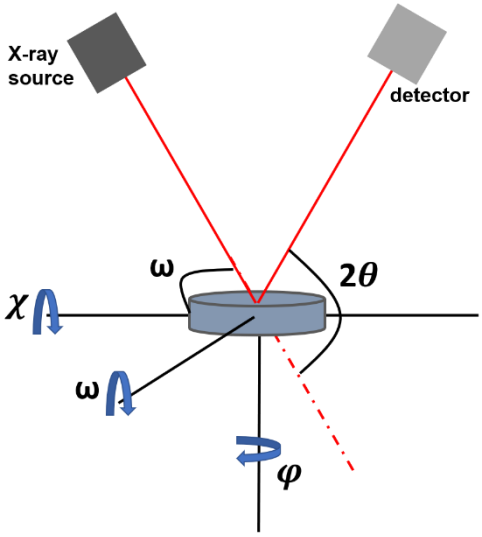

Figure 3.8: Schematic drawing of the XRD measurement setup.

where d_{hkl} is distance between the diffracting planes, θ_{hkl} is the angle between the X-ray and the lattice planes, n is the diffraction order and λ is incident X-ray wavelength (1.5406 Å). In this Thesis, the XRD experiments were performed using a Panalytical X'pert Pro diffractometer at University of Warwick. The sample position with respect to the incident X-ray direction can be tuned by changing the angle of the sample holder (θ) and detector (2θ) as well as rotating the sample holder in respective (χ, φ, ω) angles, as shown in Figure 3.8. Study of the film orientation and phase identification can be realised via 2θ - ω scan. While performing the 2θ-ω scan, the sample is placed at the position with the sample surface and the incident X-ray at the angle ω, meanwhile the detector records the scattered radiation at the angle 2θ. By continuously varying ω and 2θ in the way that the angle of the detector keeps as double of that of the incident X-ray, the 2θ-ω spectra can be obtained by recording the scatter radiation counts at each step of the angle sweeping. While keeping the 2θ fixed and varying ω in the vicinity of θ, rocking curve measurements or ω scan can be done. The full-width-at-half-maximum (FWHM) of the obtained peak can provide the information of the alignment of the 2θ-related family of crystallographic planes. Therefore, the FWHM is regarded as an important measure for the crystal mosaicity.

In order to check the epitaxial properties of the thin films, reciprocal space mapping (RSM) on some samples were conducted in this work. The reciprocal lattice is the Fourier transformation of the real space lattice, and each reciprocal lattice point represents a lattice plane in the real space. RSM around asymmetric planes, e.g. (103) can offer the lattice parameter information of the single-crystalline films. To carry out the RSM scan, a series of 2θ-ω scans with various ω steps are performed. In other words, after placing the sample around a specific lattice plane, a series of 2θ scans are performed in a range of Δ2θ at each selected ω value which is within the selected range of Δω. Through the combination of Δ2θ and Δω scans, 2D reciprocal map around a specific lattice plane with the distribution of the diffraction intensities can be derived. Subsequential lattice plane positions in the reciprocal space are given by:

$$q_{ip} = \frac{2}{\lambda}\sin(\theta)\sin(\theta - \omega) \tag{3-3}$$

$$q_{oop} = \frac{2}{\lambda}\sin(\theta)\cos(\theta - \omega) \tag{3-4}$$

where the q_{oop} and q_{ip} represent the components of the scattering vector out-of-plane and in-plane of the sample surface. Henceforth, the lattice parameters of the sample can be calculated using:

$$a\ (b) = h(k)/q_{ip} \tag{3-5}$$

$$c = l/q_{oop} \tag{3-6}$$

3.4.2 Scanning transmission electron microscopy

While XRD provides an average description of the structure information for an entire sample, scanning transmission electron microscopy (STEM) is powerful for local structure investigation which enables the detection of ion displacements, local defects, lattice parameters, elementary composition, etc. at atomic scale.[105] The STEM works on the principle that a focused beam of electrons is used to scan over the specimen, meanwhile the desired signal is recorded and processed to form the image. Using a high angle detector, atomic resolution images can be obtained as a

function of the atomic number. Resolution of the STEM image can further reach sub-angstrom with the addition of an aberration corrector. Specimen for the STEM imaging needs to be thinned down until of good electron transparency. In the present work, all the STEM images were acquired by Dr. J.J.P. Peters at University of Warwick. STEM specimens were prepared using a focused ion beam (FIB) with standard lift-out procedures. STEM images were acquired using a double CEOS corrected (to third order), Schottky emission JEOL ARM-200F microscope operating at 200 kV. To reduce scan distortion and sample drift effects, each image is the sum of 20 short exposure images. Lattice parameters were measured from the difference between atom peak positions found by fitting 2D Gaussians.

3.5 Local characterisation

3.5.1 Atomic force microscopy

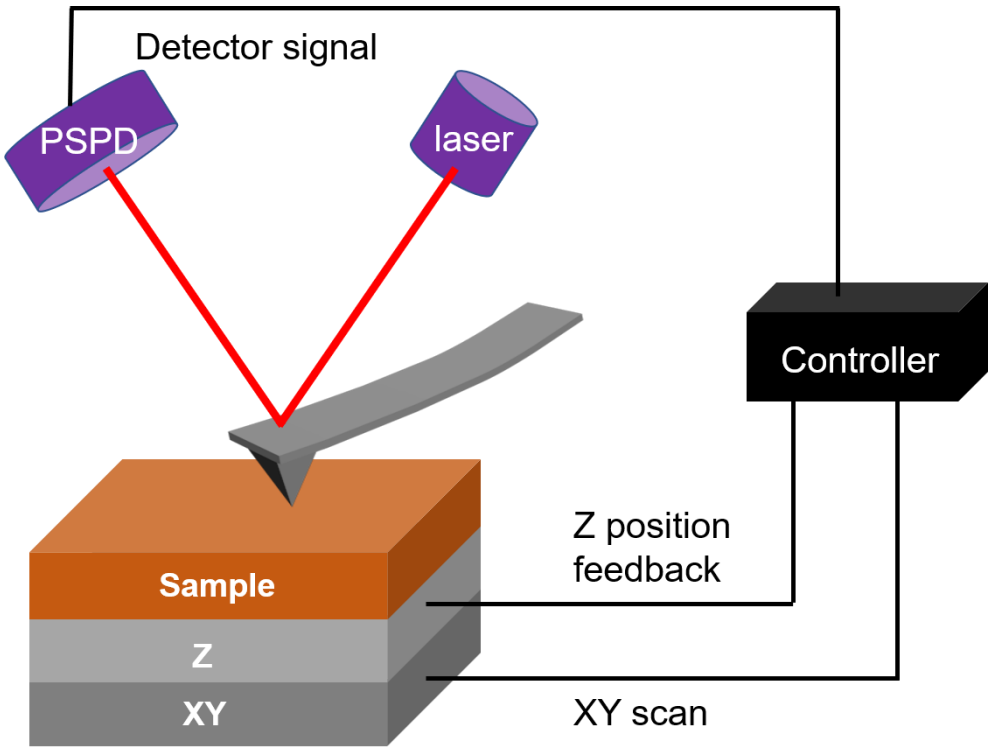

Figure 3.9: Schematic of AFM imaging configuration.

Atomic force microscopy (AFM) has matured into a versatile nanoscopic platform

enabling the characterisation of local surface properties of a broad range of materials.[106, 107] The operation principle of an AFM is based on the detection of the position change of the cantilever with a sharp needle-like nanometric tip mounted at its free end, a schematic drawing illustrating the configuration of an AFM is shown in Figure 3.9. During contouring the surface of the sample, the forces acting on the tip induced by the tip/surface interaction cause a deflection of the cantilever, and the change of the position of the laser beam reflected from the back of the cantilever onto a position sensitive photodetector (PSPD). The position change signal recorded by the PSPD is used to compare with a pre-set point, and the derived difference between them is set as error signal. The error signal is further processed by a proportional-integral-differential (PID) feedback controller, which adjusts the vertical position of the tip with respect to the sample surface. Reconstruction of the sample topography is then obtained through plotting the PID signal of the tip at different points during the scan.

Three kinds of working modes of AFM topography scanning are available: contact mode, non-contact mode and tapping mode, which are characterised according to the interaction types between the tip and sample surface. For contact mode, the tip is placed closest to the sample surface and experiences a high repulsion force, there is a set-point force applied on the cantilever to make sure that the tip stays in contact with the sample. By recording the deviation of the tip from the set-point, the surface information is captured. However, due to the constant contact of the tip on the sample surface, problems such as quick tip degradation and frictional force induced noise could occur. By lifting the tip slightly up from the surface into the regime where the tip is attracted by long range Van der Waals forces, AFM works in the non-contact mode. In this mode, the set-point value represents tip bending in the opposite direction than that in the repulsive regime. By mechanically oscillating the cantilever between the attractive and repulsive force regions, AFM works in the intermittent contact or tapping mode. It takes the advantages of both contact and non-contact modes as the cantilever is oscillated at the resonance frequency and the tip only stays in contact mode with the sample for a very short time. In this Thesis,

all the topography images were acquired in contact mode using either the Park XE-100 system or Asylum MFP3D.

3.5.2 Piezoresponse force microscopy

Piezoresponse force microscopy (PFM), which is basically a contact-AFM with an ac voltage applied to the tip, can measure the dynamic electromechanical response of ferroelectric materials.[107-109] With the ability to image and manipulate the ferroelectric domains, it has become an important technique for studying local ferroelectric properties. A typical configuration of the PFM is shown in Figure 3.10a. During vertical PFM scanning of a ferroelectric sample, an ac voltage is applied between the tip and the bottom electrode of the sample:

$$V_{tip}(t) = V_{ac}\cos(\omega t) \tag{3-7}$$

Due to the converse piezoelectric effect, the sample surface tends to expand or contract which thus leads to the surface deformation with the same oscillating manner of the ac voltage signal but with a phase difference. This process is schematically illustrated in Figure 3.10b. The electromechanical response in ferroelectrics is directional due to the presence of spontaneous polarisation. Moreover, depending on ferroelectric polarisation with respect to the applied voltage direction, piezoresponse of the sample can be divided into two situations: 0° in-phase and 180° out-of-phase to the driving voltage for ferroelectric polarisation parallel and antiparallel to the voltage direction, respectively. The sample local piezoresponse can be detected by the PSPD through its interaction with the tip and modulated by a lock-in amplifier as an electric signal. Therefore, by comparing the phase difference between the ac voltage signal (reference) and the cantilever deflection signal, one can obtain the vertical polarisation information. Normally, the measured piezoelectric response is comprised of phase and amplitude signals. Moreover, as the piezomechanical vibrations of the in-plane or lateral ferroelectric domains can also be detected by the tip, it is possible to extract the information of the IP ferroelectric polarisation component. By recording the in-plane (IP) and out-of-plane (OOP) cantilever deflections, IP and OOP domain

structures of the sample can be simultaneously measured.[45, 49]

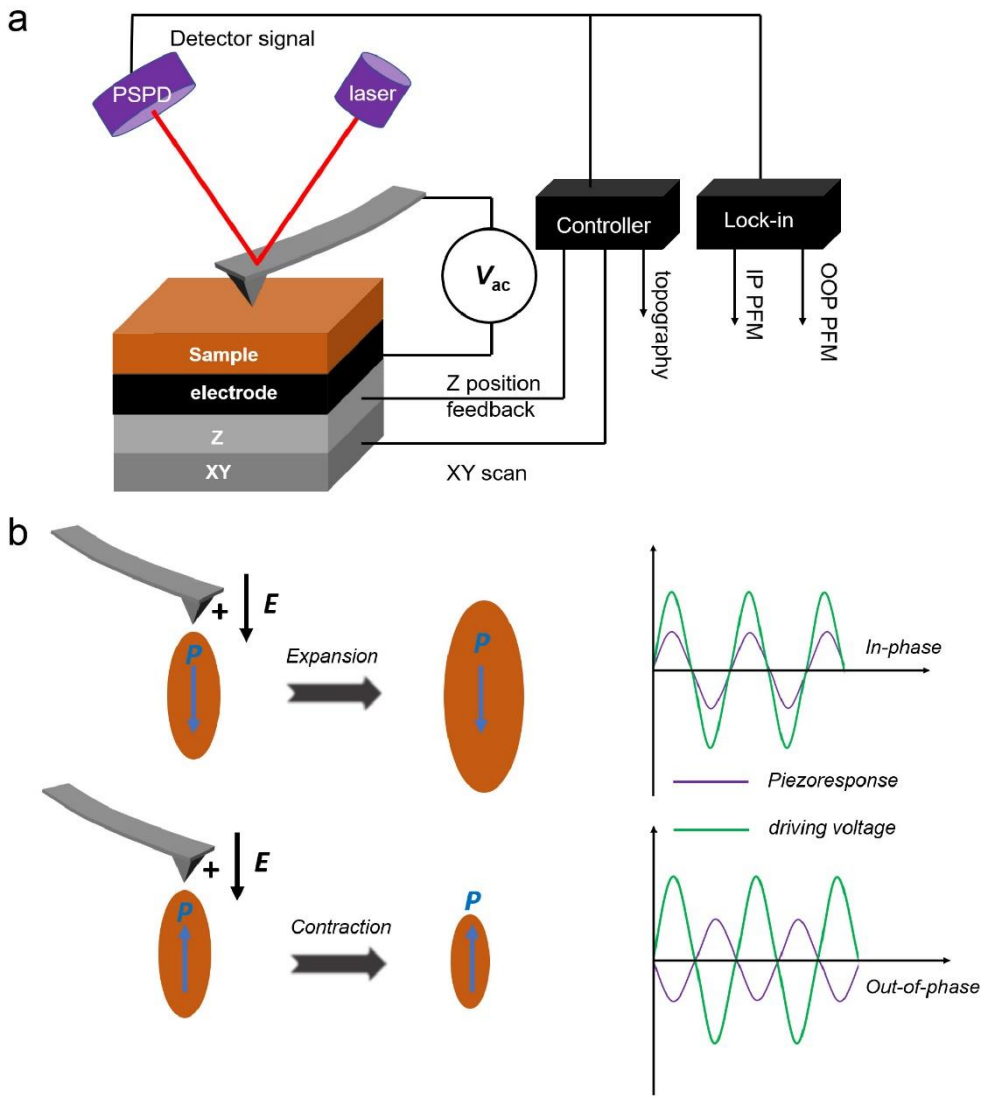

Figure 3.10: Schematic of the PFM setup and working principles. (a) Schematic illustration of the configuration of a PFM. (b) Working mechanism of the vertical PFM. Ferroelectric materials expand or contract when the polarisation aligns parallel or antiparallel to the applied voltage at the tip. The applied ac voltage therefore results in the 0° and 180° piezoresponse phase for parallel and antiparallel polarisation/applied voltage alignments, respectively.

3.5.3 Conductive-AFM and Photo-AFM

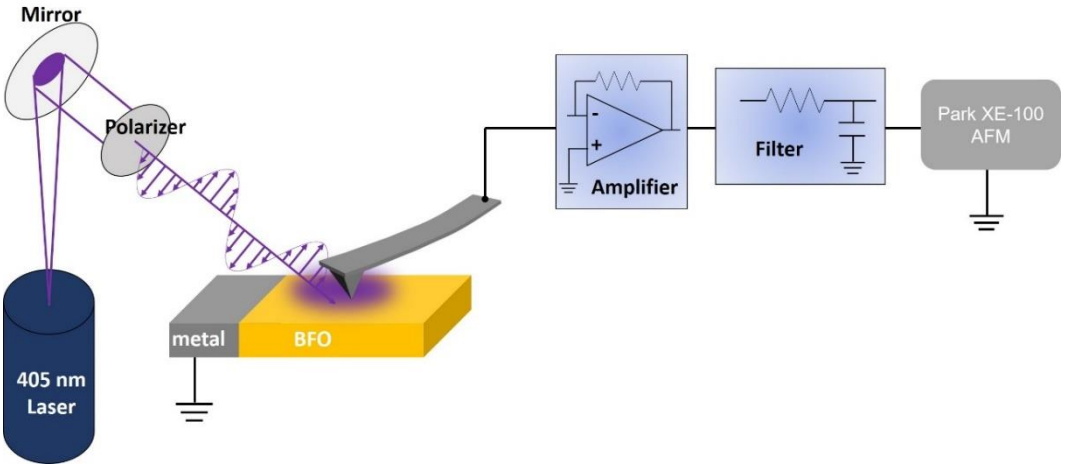

Figure 3.11: The schematic illustration of the configuration of a self-built ph-AFM system. The components excluding the laser part are basically the CFM module.

Conductive-AFM (C-AFM) using a conductive tip in contact AFM mode, can be used to measure the current distribution of an insulating layer by applying the voltage between the tip and the bottom electrode underneath the insulating layer. In this study, for investigating local electronic properties under light mediation, we combined the Park XE-100 C-AFM module with an optical system which we named as Photo-AFM (ph-AFM) system.[50, 101] The configuration of this system is displayed in Figure 3.11. The light is directed on the sample surface with the light-polarisation controlled by an automatically controllable half-wave plate. The light-induced electric signal collected by the AFM tip is amplified by a transimpedance amplifier (Femto, DLPCA-200) with a switchable gain ranging within 10^3 V/A to 10^{11} V/A. Subsequently, the voltage signal is processed using a low pass filter with a cut-off frequency of 300 Hz and 12 dB. Eventually, the processed electric signal is passed to the AFM system which can simultaneously record the electric signal along with other signals like topography.

3.6 Electric and magnetic measurements

3.6.1 Ferroelectric tester

Ferroelectric hysteresis loop which is a consequence of domain structure evolution showing the non-linear response of polarisation to the applied electric stimulus, is normally considered as the most primary characteristic for ferroelectrics. Through the hysteresis loop, characteristic parameters of a ferroelectric including spontaneous polarisation, remnant polarisation and coercive field can be obtained. The basic idea of measuring the hysteresis loop is to record the polarisation of a ferroelectric as a function of applied ac voltage waveform. To achieve it, a 'sense' capacitor is connected in series to the ferroelectric capacitor, and the charge density collected by the 'sense' capacitor is considered as the same as the polarisation value of the ferroelectric in practice. In the current study, a commercially available ferroelectric tester (aixACCT: TF2000) was used for recording the ferroelectric switching behaviours of ferroelectric films thicker than 10 nm.

3.6.2 Magnetic characterisation tools

In this study, Quantum design MPMS-5S Superconducting QUantum Interference Device (SQUID) and Physical Property Measurement System (PPMS) were used for magnetic-related experiments.

SQUID is a very sensitive magnetometer which can be used to detect extremely subtle magnetic response. The principle of how the SQUID works is based on the ability to convert the magnetic flux into an electrical signal by exploiting the flux quantization and Josephson effect.[110, 111] The MPMS-5S SQUID we used is with a sensitivity of 10^{-7} emu and capable of sweeping vertical magnetic field from -7 T to 7 T and changing the temperature from 4 K to 400 K. As displayed in Figure 3.12, to perform the SQUID measurement, the sample is placed into a clear drinking straw which serves as the sample holder. As the magnetic field in SQUID can only be applied in the vertical direction, the sample should be placed with its plane along or perpendicular to the magnetic field upon the realistic measurement

requirement.[110, 112] For those complex angle-dependent magnetic tests, a rotator for the SQUID system is available.

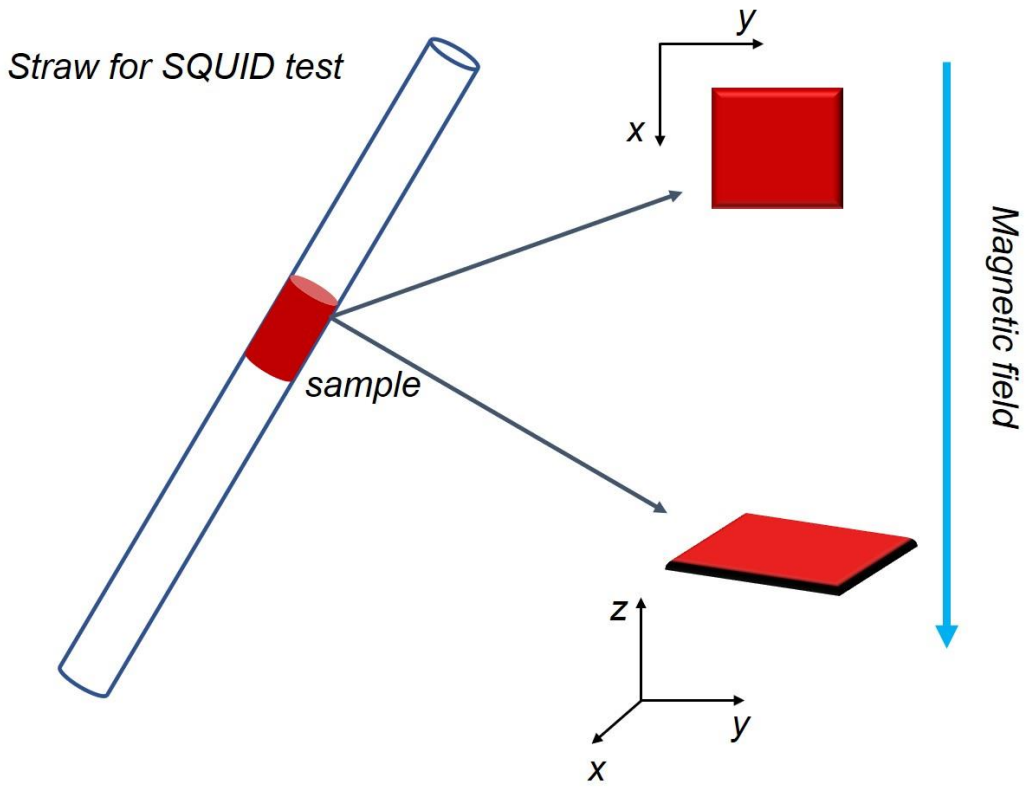

Figure 3.12: A cartoon showing the sample measurement method using the SQUID.

PPMS is a versatile tool for magnetic field and temperature dependent transport experiments. In this study, we performed tunnelling magnetoresistance (TMR) experiments on the multiferroic tunnel junctions using the PPMS of the Superconducting and Magnetism group of Warwick university. The PPMS is capable of providing the test environment with temperature ranging from 400 K to 1.8 K and vertical magnetic field sweeping in the range of -9 T to 9 T. With its own hardware, transport measurements can be conducted in ac or dc modes with automatic computer control. In the case of performing our TMR tests, a rotator was used to align the sample plane parallel to the direction of magnetic field. Magnetoresistance properties of the samples were collected using the self-built source meter/function generator setup described in the following section.

3.6.3 Tunnelling electroresistance measurement setup

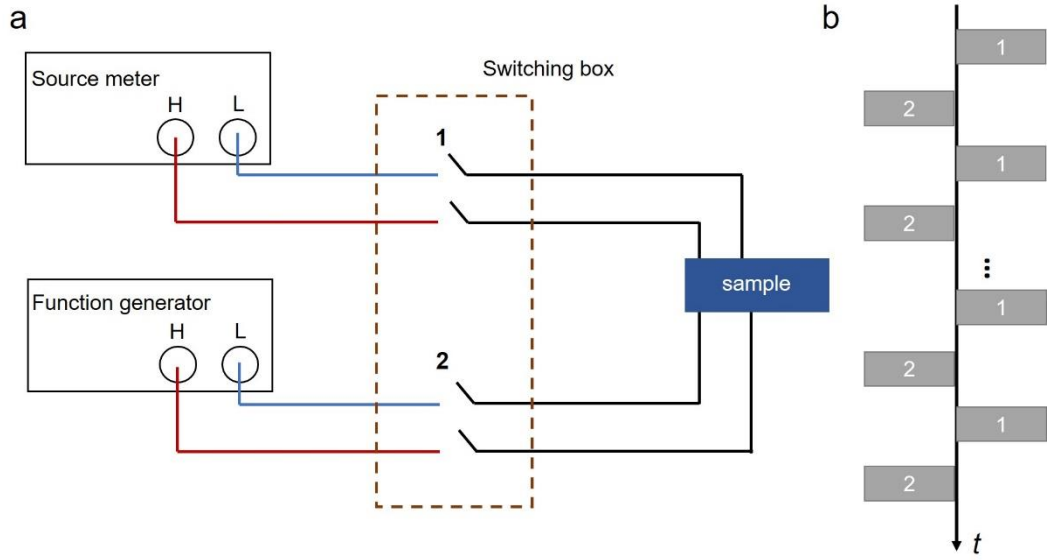

Figure 3.13: Tunnelling electroresistance measurement setup. (a) Schematic drawing of the setup for TER measurements. (b) The event sequence demonstrating the method for multiple TER tests.

Current-voltage (*I*-*V*) measurements were generally used to record the transport properties of our ferroelectric tunnel junctions. For tunnelling electroresistance (TER) measurements, *I*-*V* of the ferroelectric tunnel junctions should be recorded at different polarisation states of the ferroelectric barrier. As shown in Figure 3.13a, A home-made system consisting of a source meter (Keithley 2635) and a function generator (Tektronix AFG 3102) with a specifically designed switching box is presented for the purpose of TER measurements. The system with a digital I/O card can be automatically controlled by a computer through the developed software in our group. For setting the polarisation state in the ferroelectric barrier, programmable voltage pulses are applied by the function generator through '2'. The resistance state of the ferroelectric tunnel junction is subsequently recorded by *I*-*V* measurement using the source meter through '1'. For memristor measurement, a large number of voltage pulsing events and *I*-*V* measurements were conducted using the software. The programme was written following the sequence of events

showing in Figure 3.13b, which thus can record the *I*-*V* data of the ferroelectric tunnel junction after each applied voltage pulse.

TMR measurements were conducted using the same setup but putting the sample in the PPMS system which can provide the desired temperature and magnetic field. During TMR measurement, a constant voltage was applied on the sample while sweeping the magnetic field, i.e. recording the continuous current as a function of magnetic field.

3.7 Summary

In this chapter, introduction of thin film growth technique and all the materials used in this work with focus on their crystal structure information along with experimental facilities and methods has been presented. Physical properties of thin films are strongly related to their crystal structure and growth quality, for example strain engineering by lattice misfit of the substrate and oxygen vacancies introduced through changing the oxygen pressure during growth can completely alter the sample properties. Therefore, careful optimisation of the growth parameters as well as the choice of the right substrate are crucial for growing thin films exhibiting the desired properties. Photolithography along with electrode fabrication method were discussed, particularly on the process of fabricating devices with specific designs. XRD and STEM as important tools for structure analysis were used for evaluating the quality and lattice parameters of the thin films. AFM system equipped with PFM, C-AFM and ph-AFM functions are discussed in terms of their working principles and the possibilities of using them for topography, ferroelectric domain and local transport measurements. Finally, tools for characterising magnetic and electric-transport properties of samples along with the basic idea of TMR and TER measurements are briefly demonstrated.

Chapter 4

Magnetoelectrically coupled memristive behaviours in a multiferroic tunnel junction

Recently, magnetic tunnel junction (MTJ) and ferroelectric tunnel junction (FTJ) enabled memristive devices have been demonstrated.[5, 30] However, a single device showing simultaneously magnetic and electric memristive behaviours has not yet been reported. In this chapter, we present such a magnetoelectrically coupled memristor based on a Co/$PbTiO_3$ (PTO)/$La_{0.3}Sr_{0.7}MnO_3$ (LSMO) multiferroic tunnel junction (MFTJ). In such an MFTJ, the tunnelling magnetoresistance (TMR) can be reversibly controlled by voltage pulses owing to ferroelectric polarisation-dependent spin polarisation at the ferroelectric/ferromagnetic interface. Through electrically modulating the ratio between up- and down-polarised ferroelectric domains, a broad range of tunnelling magnetoresistance and tunnelling electroresistance can both be achieved, which leads to the magnetoelectrically coupled memristor.

4.1 Motivation: towards the bi-ferroic memristor

MTJ, composed of a thin dielectric barrier sandwiched between two ferromagnetic electrodes, presents the TMR effect which shows two distinct resistance states in response to parallel or antiparallel magnetic moment configuration in the ferromagnetic electrodes. Although MTJs have been the subject of intensive study due to its great potential for non-volatile magnetic memory applications,[34, 113, 114] moderate data storage density and especially a high-power consumption for controlling magnetisation still remain as major obstacles for improving the device performance. To tackle these problems, several methods have been proposed including but not limited to utilising various non-collinear magnetization configurations in the ferromagnetic electrodes of semiconductor spin valves[115] or all-oxides MTJs,[116] manipulating domain states of ferromagnetic electrodes in

pseudo spin vales,[117] or tuning tunnel barrier oxygen vacancies by voltage pulses in MgO-based MTJs.[30] Despite the aforementioned solutions, one promising candidate is MFTJ, in which the ferroelectric/multiferroic layer is incorporated into a conventional MTJ as the tunnel barrier.[39, 41, 42, 118-122] Four memory states can be obtained in MFTJs by voltage pulsing thanks to the coexisting TMR and tunnelling electroresistance (TER) given by resistance variation upon different ferroelectric polarisation orientations.[6, 16, 19, 20, 23, 123-126] Moreover, MFTJs have been demonstrated as a rich platform to explore the electric control of magnetism at the ferroelectric/ferromagnetic interface.[6, 41] Therefore, such a structure is extremely appealing for high density memory applications with ultralow power consumption and exploring the emerging electronic properties from the research point of view.

As mentioned before, four resistance states can be obtained for an MFTJ corresponding to its upward and downward ferroelectric single-domain state. However, during the ferroelectric switching, multi-domains with opposite polarisations can indefinitely coexist. The actual domain configuration can be easily tuned by choosing the parameters, i.e. amplitude and duration of the switching voltage pulse.[7] Domain configuration, an important degree of freedom in ferroelectrics, can in principle result in multiple levels of ferroelectric polarisation states corresponding to the volume ratio of up- and down-polarised ferroelectric domains.[5, 33, 127] Recently, engineering of the ferroelectric domain structure has enabled new functionalities in ferroelectric-based devices, such as multilevel polarisation states in the ferroelectric random-access-memory (FeRAM)[33] and continuous resistance states in the ferroelectric memristor.[5, 127, 128] On the other hand, it has been shown that in an MFTJ, significant change of spin-dependent tunnelling and thus TMR can be obtained between opposite ferroelectric polarisation states due to the polarisation dependent screening effects[129] and hybridisation[42, 119] at the ferroelectric/ferromagnetic interface. Keeping this in perspective, like the case of memristor behaviour in FTJs, one can perceive that the spin transport, consequently the value of TMR, in an MFTJ can be continuously tailored by controlling the ferroelectric domain configuration. So far, this effect of

the ferroelectric domain configuration on MFTJ magnetotransport has not been investigated. In this chapter, we experimentally demonstrate the multi-level electric control of both TMR and TER in Co/$PbTiO_3$(PTO)/$La_{0.3}Sr_{0.7}MnO_3$(LSMO) MFTJs. While in case of FTJs that the ferroelectric polarisation tunes the charge transport (tunnel current), in the present case the ferroelectric polarisation is shown to control the spin polarised transport and thus the TMR of MTJs.

4.2 Sample structure

4.2.1 Topography and ferroelectricity

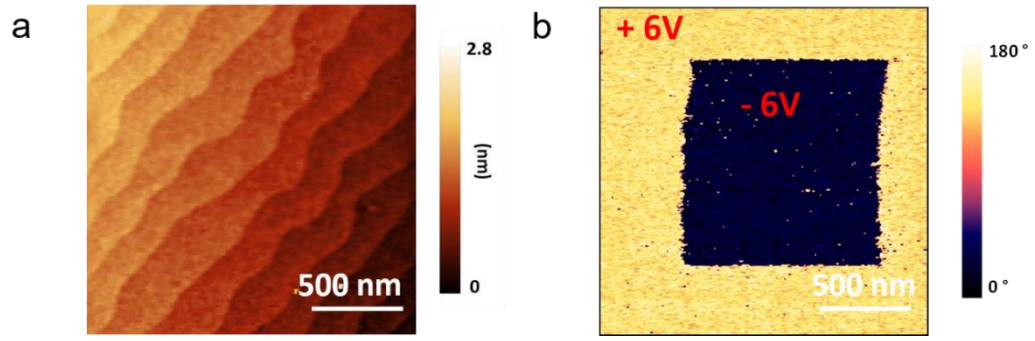

Figure 4.1: Topography (a) and PFM with electrically written ferroelectric domains (b).

MFTJs are based on high quality PTO (12 u.c.)/LSMO (60 u.c.) epitaxial thin films grown on (001)-oriented $SrTiO_3$ (STO) substrates by Pulsed Laser Deposition (PLD). Samples were prepared by Dr. G. Apachitei and detailed fabrication process can be found from our previous reports.[120] We first investigated the topography and ferroelectric properties of the PTO/LSMO heterostructure using AFM and PFM, the results are shown in Figure 4.1. AFM and PFM images were collected using the Park XE-100 system. PFM data were collected with 1 V ac voltage and 23.27 kHz frequency using a NSC14/Pt (MikroMasch) cantilever. It can be seen from the AFM image in Figure 4.1a that the surface of the PTO is atomically flat. The ferroelectricity of the PTO film is shown in Figure 4.1b, the out-of-plane PFM image demonstrating clear 180° phase contrast after electric writing of ferroelectric domains indicates the strong piezoelectric activity and stability of written

ferroelectric domains in our thin PTO films even at the 12 unit-cell thickness.

4.2.2 Microscopic structure

The Co/PTO/LSMO sample was further characterised by the scanning transmission electron microscopy (STEM). All the STEM images were taken using a double CEOS corrected (to third order), Schottky emission JEOL ARM-200F microscope operating at 200 kV in STEM mode. In Figure 4.2, annular dark field (ADF) STEM imaging shows that the well-defined Co/PTO/LSMO heterostructure and the magnified image on the right panel with atomic number contrast clearly indicates that Co/PTO and LSMO/PTO interfaces are atomically sharp. The above results therefore indicate that the PTO/LSMO heterostructure is of high quality and robust ferroelectric properties which can serve as a model multiferroic tunnel junction system for the following studies on the memristive behaviours.

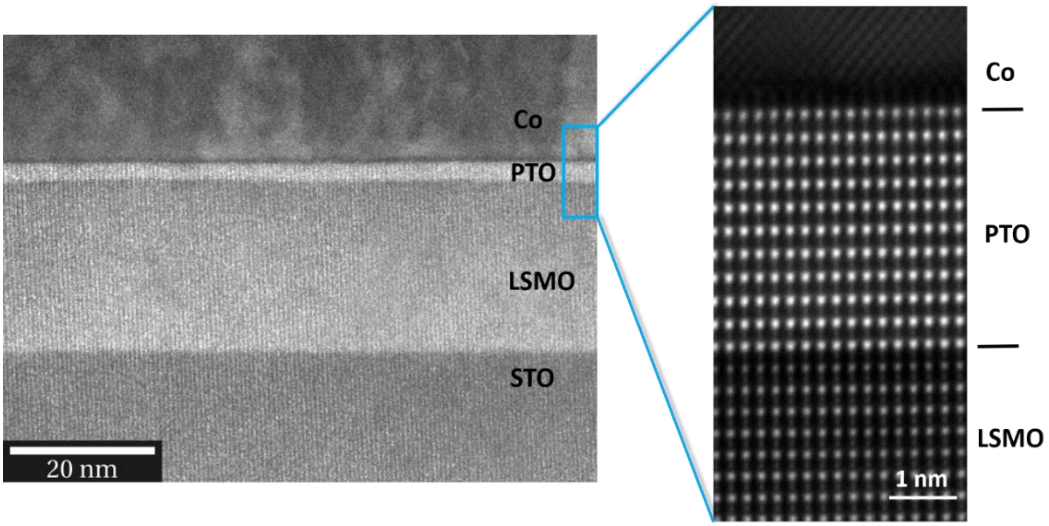

Figure 4.2: STEM images of the Co/PTO/LSMO heterostructure.

4.3 Magnetoelectrically coupled memristive properties

4.3.1 Polarisation controlled electronic and spin transport

In order to carry out the transport measurements, tunnel junction devices were defined by patterning 40×40 um^2 Au/CoO/Co top layers as top electrodes through

photolithography, sputtering and lift-off. The devices were mounted on the PPMS puck and inserted into the PPMS in which variable temperatures and magnetic fields can be applied, see Chapter 3.6.2 for details. To make contacts onto these small top electrodes, insulating photoresist hard mask was adopted, a device with connected contacts is schematically displayed in Figure 4.3.

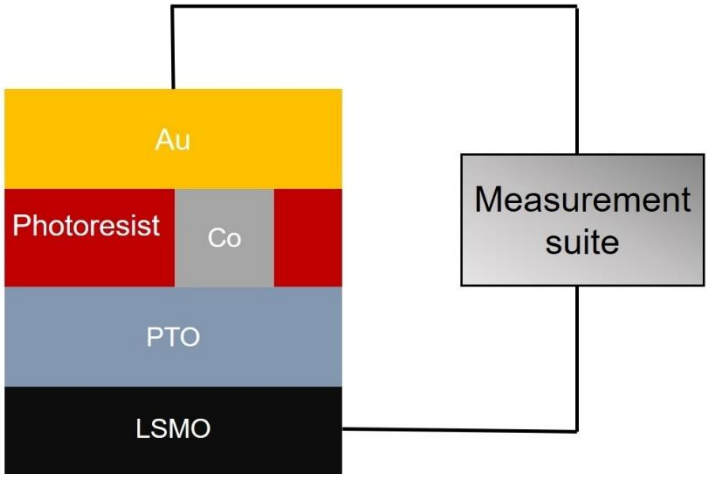

Figure 4.3: The connection of an FTJ device using a photoresist hardmask.

We first characterised the electronic transport properties of the FTJs at two opposite ferroelectric polarisation directions. By applying 6 V and -6 V voltage pulses with a duration of 50 µs on the PTO FTJs, a drastic change of the *I-V* behaviours was observed (see Figure 4.4a). At 100 mV, the resistance change of the device is more than 1000% which refers to a giant TER.[130]

After confirming the TER behaviour of the FTJ, we further conducted TMR measurements after cooling the sample with -0.5 T magnetic field to 10 K from room temperature, at the PTO polarisation up and down states, respectively. The TMR is defined as: $TMR = (R_{ap} - R_p)/R_{ap}$, where R_{ap} and R_p are the junction resistance in the antiparallel and parallel magnetic configurations of the electrodes, respectively. As shown in Figure 4.4b, the TMR is found to strongly depend on the ferroelectric polarisation orientation. More than 10-fold change of the TMR value is observed here between up- and down-polarised ferroelectric single domain states. The negative TMR observed here suggests a negative spin polarisation nature at

Co/PTO interface and highlights the spin-dependent interfacial bonding effect which is typical of the perovskite oxide-based interface.[6, 42, 120, 131] Unlike in our earlier work on $Pb(Zr,Ti)O_3$-based tunnel junctions, the TMR does not change the sign when the polarisation switches from totally up (P_{up}) to totally down (P_{down}) states.[41, 120] In the present case of PTO-based tunnel junctions, the TMR absolute value decreases from about 30% (TMR_{high}) in the P_{down} state to almost zero, i.e. only 3% (TMR_{low}), in the P_{up} state, rather similar to the $BaTiO_3$ (BTO) case reported by Garcia *et al.*.[6] It is worth noting that the variation of TMR amplitude with PTO polarisation direction is opposite to that of the BTO case, i.e., TMR absolute value gets larger while switching PTO polarisation downward which is consistent with previous Pb-based ferroelectric MFTJs.[120, 132]

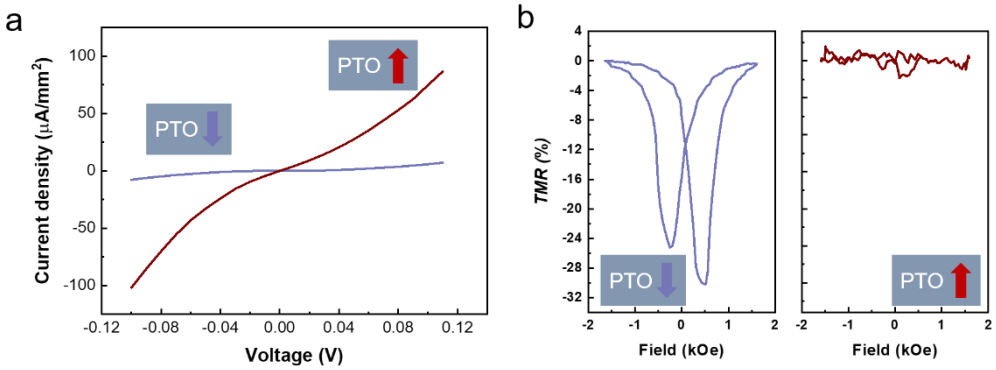

Figure 4.4: Polarisation dependent I-V curves (a) and TMR properties (b) of the MFTJ. Data taken at 10 K.

We note that the TMR of the MFTJ is asymmetric. This behaviour is related to the intentionally inserted CoO layer at the top electrode. With the CoO/Co antiferromagnetic/ferromagnetic bilayer, exchange bias is introduced to enhance the ferromagnetic coercivity which helps the practical TMR measurement.[6] The corresponding magnetic response of the MFTJ sample was measured by the SQUID as shown in Figure 4.5. The ferromagnetic hysteresis loop was measured following the same magnetic field cooling procedure as that for TMR measurement, i.e. cooling from 300 K to 10 K with a negative 0.5 T field. Clearly, minor loop of Co and major loop of LSMO can be found due to their different coercive fields.

Moreover, the exchange bias of CoO/Co is obvious as can be seen from the horizontal shift of the hysteresis loop.

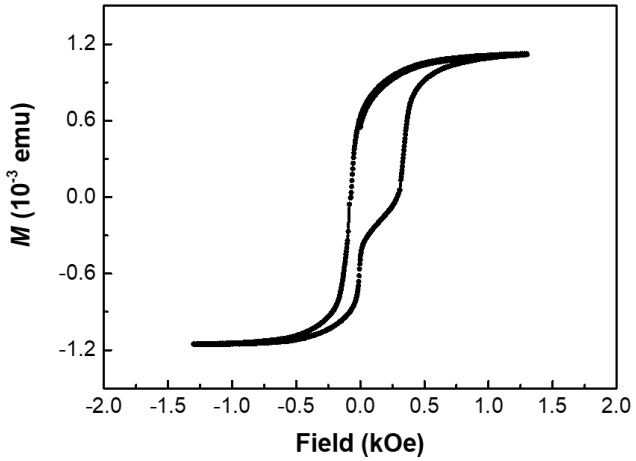

Figure 4.5: Ferromagnetic hysteresis loop of the Au/CoO/Co/PTO/LSMO film.

4.3.2 Programmable bi-ferroic memristor

For a memristor, the functional properties are permanently changed in response to a set of voltage driven process.[30] In our case, we found that the TER and TMR of the MFTJ can be dynamically tuned by applying voltages pulses, which manifests that the MFTJ can serve as a memristor with ferroelectric-ferromagnetic coupled tunnelling properties. The main functional properties of the tunnel junction are shown in Figure 4.6. The TER properties are shown in Figure 4.6a where zero-magnetic field *I*-*V* curves of the MFTJ were collected at 10 K after applying writing voltage pulses with various amplitudes. Starting from the totally downward polarised state (after 6 V poling), we gradually changed the population of upward and downward ferroelectric polarisation via a set of negative voltage pulses. The transport properties of our MFTJ change accordingly, and eventually the full change of resistance state associated with single domain state (*P* fully upwards) has been obtained. Summarised in Figure 4.6b, one can clearly see this reversible resistive switching behaviour of our MFTJ. The multilevel resistance states change shown here, demonstrating the memristive properties, can be attributed to the

corresponding domain reconfiguration process during polarisation reversal in the ferroelectric films similar with previous reports.[127, 128, 133, 134]

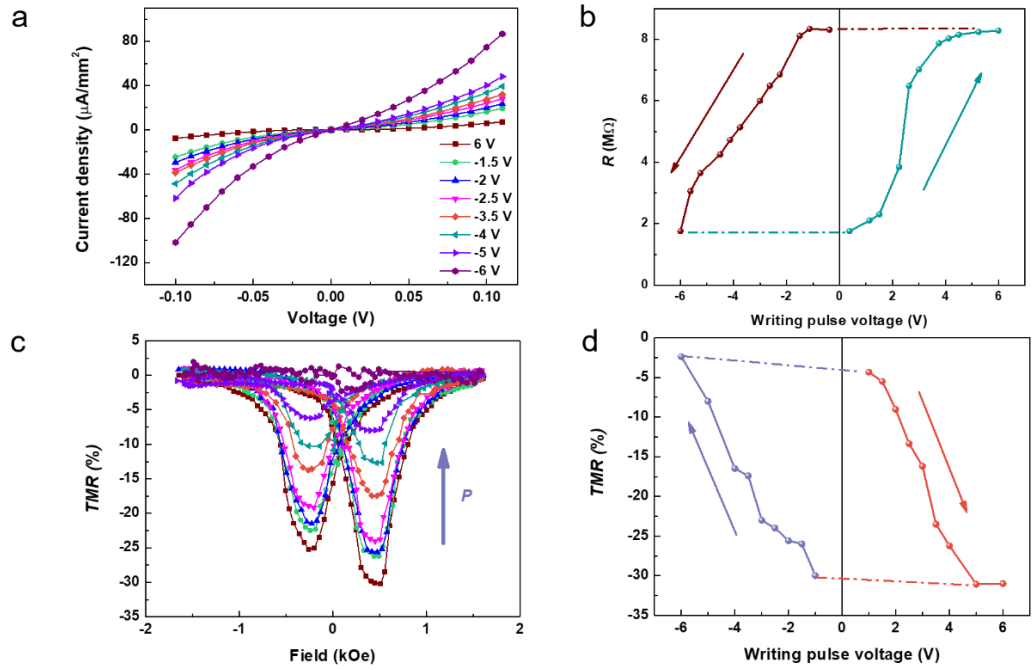

Figure 4.6: TER and TMR evolution as a function of voltage pulses. (a) $I-V$ curves of the MFTJ measured at 10 K after poling by writing voltages pulses with different amplitudes and constant width (50 μs). (b) Tunnelling resistance of the MFTJ after poling the PTO ferroelectric barrier into different states. (c) TMR of the junction recorded at 10 K with 10 mV applied bias after -0.5 T cooling from 300 K as a function of PTO ferroelectric polarisation states. (d) Dependence of the TMR of the PTO polarisation states as changed by various writing pulse voltages.

Given the ability to partially switch the polarisation, in other words, to continuously modify the population of P_{up} and P_{down} ferroelectric domains, we can assume that the TMR will follow the same tendency as the TER. To gain insights into the MFTJ spin transport properties in response to the ferroelectric barrier domain configuration, we performed TMR measurements at a set of polarisation states. We switched stepwise the ferroelectric polarisation of the MFTJ by applying consecutive voltage pulses with various amplitudes and fixed duration of 50 μs at

zero magnetic field. As expected, a clear stepwise TMR evolution from high value (31%) towards low value (2.8%) in response to the ratio of up- and down-polarised ferroelectric domains is observed, as shown in Figure 4.6c. The TMR amplitude changes more than one order of magnitude, or more than 1000% change in terms of TMR_{high}/TMR_{low} ratio, by applying voltage pulses between -6 V and 6 V. Moreover, this effect which leads to a multi-level electric control of TMR is reversible and reproducible. As can be seen in Figure 4.6d, multiple TMR levels between high (~31%) and low (~2.8%) states can be deterministically set in a classical hysteretic way that follows the ferroelectric polarisation switching process. These results unambiguously demonstrate that depending on the ferroelectric polarisation switching history, the TMR states of the MFTJ can be finely tuned into any level between TMR_{high} and TMR_{low}. In such way an intrinsic spin transport property of the junction, i.e. TMR, can be continuously tuned by solely applying the electric field pulses. Since the tunnelling transport is related to both magnetic and electric order parameters which are electrically tuneable, we can state that MFTJs are bi-ferroic or magnetoelectrically coupled memristors.

Further on, we show that the multilevel control of TMR is not only dependent on the voltage pulse amplitude but also on the duration which provides a further parameter for control from the device application point of view. As shown in Figure 4.7, the TMR changes as a function of voltage pulse duration under 5 V and -6 V voltage amplitude. The measurement sequence is shown in Figure 4.7a. We performed each TMR measurement after applying a SET pulse with different duration to the junction. Before each SET pulse and TMR measurement, we reset the junction into TMR_{high} or TMR_{low} state as the reference by applying a 10 ms long -6 V or 5 V ReSET pulse. The results are summarised in Figure 4.7b. Clearly, starting from the reference state, the TMR can be driven into a large number of intermediate states between TMR_{high} and TMR_{low} using certain writing pulses. The time scale to access these intermediate levels is of ~ μs range which is comparable with the ferroelectric polarisation switching time.[5, 127] The TMR data are fitted with

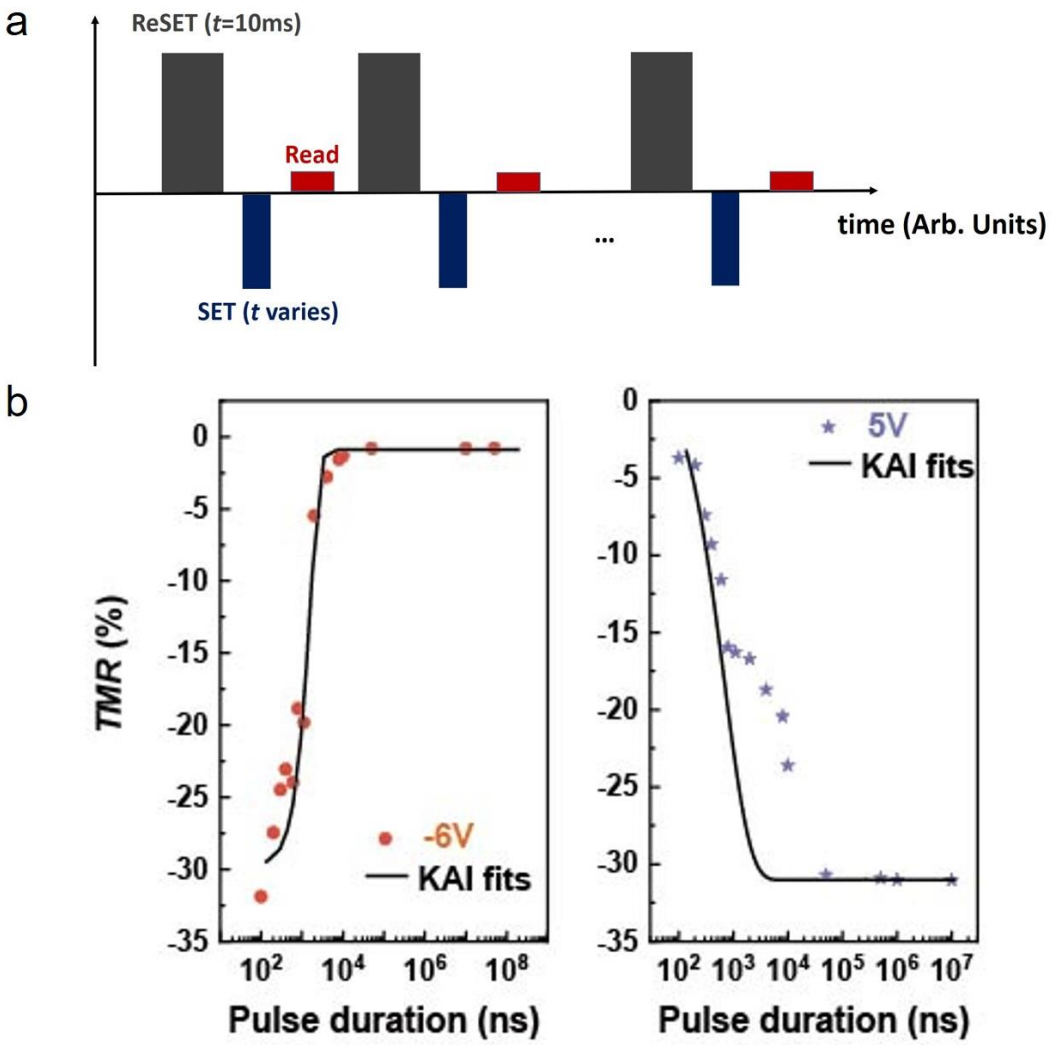

Figure 4.7: Voltage pulse duration dependent tuning of TMR of the MFTJ. (a) Schematic drawing of voltage pulse trains used for control of TMR. A pulse train contains a ReSET pulse to switch the TMR into high or low reference state, then a SET pulse to drive the TMR into desired state and eventually the Read represents a TMR measurement. (b) The evolution of the TMR as a function of the writing pulse duration with -6 V and 5 V amplitude, respectively. The data are shown as symbols and the lines represent the KAI fits.

$\frac{TMR_{high}}{TMR_{low}} \propto e^{-(\frac{t}{\tau})^n}$ as described by the Kolmogorov-Avrami-Ishibashi (KAI) model, where τ is the characteristic switching time.[135] Here, as the polarisation switching

in ultrathin epitaxial ferroelectric thin films is mostly bi-dimensional,[127] we can assume that $n = 2$ in our case. As can be seen from the KAI fits, the TMR evolution for polarisation down-to-up process (applying -6 V voltage pulses) can be well-fitted using the KAI model with $\tau = 893$ ns, indicating the domain nucleation and propagation process. However, for polarisation up-to-down process, a delayed switching can be observed by comparing the KAI fits with the experimental data. We argue that this delay could be contributed to an asymmetric nucleation process as reported before.[5] For the polarisation up-to-down process, the nucleation centres for domain switching needs to be activated while the pinned domains can act as the nucleation centres for the opposite polarisation switching process. It also explains why slightly higher voltages are needed for the down-to-up switching process. For the same junction device, the TMR evolution under cumulative voltage pulses after up to 100 fully switching can still follow the same trend and be well fitted by the KAI model which indicate a good repeatability of the MTFJ (data not shown). Overall, the results shown in Figure 4.7 demonstrate that the TMR levels cannot only be tuned by the voltage pulse amplitude but also the period of the switching pulse. This is in agreement with the ferroelectric polarisation switching kinetics[5, 135] and further confirms the multiple TMR states are corresponding to the ferroelectric barrier domain configuration.

4.3.3 Domain structure evolution

The above experimental results clearly reveal that the memristive behaviours of TMR/TER are related to the ferroelectric polarisation dependent spin transport and multi-domain state of the tunnel barrier. The ferroelectric polarisation switching process, which involves the domain nucleation and growth, can result in the stable domain pattern of mixed domains with opposite directional polarisations.[5, 127] Through carefully choosing the switching pulse amplitude and time, one can obtain exactly the desired ratio of the up- and down-polarised domains.[5, 33, 127, 128] Moreover, multi-domain state is robust due to its smaller depolarisation energy than that of the single-domain state.[7] A schematic drawing of such a mixed domain state

is sketched in Figure 4.8a. To confirm the hypothesis, we visualized the domain evolution by recording the PFM images of three different domain states of PTO after applying a set of short-duration voltage pulses on the top electrode. As can be seen from Figure 4.8b, apart from the fully upward and downward polarisation state, an intermediate state of mixed domains indeed exists.

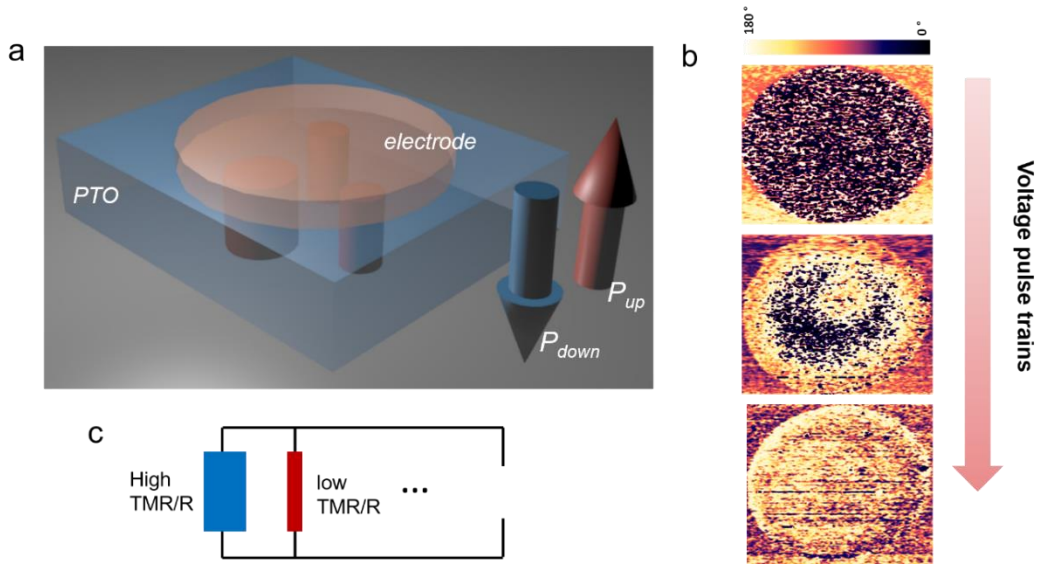

Figure 4.8: Domain evolution in PTO layer. (a) Schematic drawing of the multi-domain state consisting of oppositely polarised ferroelectric domains in the PTO tunnel barrier. The dark-red rods under the electrode present the growth of upward polarisation domains. (b) PFM images showing the PTO domain evolution during applying a set of voltage pulses on the 5 nm thick Pt top electrode (circular shape with 2 µm diameter). (c) A multi-channel model of memristive TMR and TER behaviours.

4.3.4 A qualitative model for the memristive behaviour in the MFTJ

Although the mechanism that relates the spin transport and ferroelectric polarisation remains under debate. However, a plausible scenario suggested by recent theoretical and experimental work has related such a phenomenon to emerging hybrid electronic and magnetic states or even ultrathin interfacial metal oxide layer which can form at ferromagnetic/ferroelectric interface and be

manipulated by ferroelectric polarisation. [6, 41, 42, 120, 131] This interface acts as a further spin-filter so that the spin-polarisation of the current can strongly vary or even can change its sign while switching ferroelectric polarisation toward or away from ferroelectric /ferromagnetic electrode interfaces.[6, 41, 42, 120, 131] This behaviour is also confirmed in our results as a clear TMR change by switching the PTO polarisation is presented.

Taking the multi-domain state and spin-dependent interfacial bonding effect at ferroelectric/ferromagnetic metal interface into consideration, this memristive TMR/TER behaviour in our MFTJs can be qualitatively understood by a global TMR/TER state resulting from a weighted arithmetic mean of different spin polarisations/resistances corresponding to mixed domains with opposite ferroelectric polarisation directions. In the FTJ memristor, the total device resistance is equivalent to individual resistors represented by ferroelectric domains connected in parallel.[5, 127, 128] Analogously, in the TMR case, each Co/PTO ferroelectric domain interface can control the spin polarisation and implicitly the TMR (see Figure 4.8c). The ferroelectric domains can be regarded as the separated spin-dependent transport channels where the spin polarisation is at high state for polarisation pointing away from the PTO/Co interface and changes to its low state for the opposite situation when polarisation points to PTO/Co interface, i.e. PTO domains are up-polarised. Within the top electrode area, the overall spin polarisation and consequently the TMR of the junction are therefore decided by the ratio of up- and down-polarised PTO domains.

4.4 Summary

Memristive TMR and TER behaviours is presented in Co/PTO/LSMO MFTJs enabled by the ferroelectric domain configuration. A broad range of stable and reversible TMR and TER states between their own high and low states can be obtained via electric pulsing. A qualitative model based on the multi-domain transport channels is presented to interpret those results. This electric field multi-level control of TMR and TER shown here suggests a magnetoelectrical coupled or

bi-ferroic memristive nature as an enhanced functionality of MFTJs. The interplay between electronic transport, magnetotransport properties and ferroelectric domain configuration revealed in this study of these seemingly very simple MFTJ devices can further stimulate continued fundamental multiferroic research and broaden their potential applications.

Chapter 5

Light control of ferroelectric tunnel junctions: a hybrid approach

The light control of non-volatile nanoscale memories could represent a fundamental step towards novel optoelectronic devices with memory and logic functionalities. However, most of the proposed devices exhibit insufficient control in terms of the reversibility, data retention, photosensitivity, limited-photoactive area, etc. In this chapter, we demonstrate the use of tip-enhanced bulk photovoltaic effect (BPV) to realise programmable nanoscopic writing of non-photoactive electronic devices, i.e. ferroelectric tunnel junction (FTJ) by light control. The tip-enhanced BPV in combination with the nanoscale contact connection, i.e., atomic force microscopy probe technique can induce more than 10^5 % reversible switching of tunnelling electroresistance of ferroelectric tunnel junctions. The tip-enhanced BPV-FTJ combination thus opens the door for novel optoelectronic non-volatile memories based on ferroelectric oxide structures.

5.1 Motivation: a hybrid optoelectronic memory

Light control of electronic data storage elements has led to new paradigms for optoelectronic memory and logic systems, which are in great demand for future multifunctional agile information storage and computing science.[136-146] Implementing such optoelectronic memory systems, especially for the post-Moore era, requires the ability to: (i) reversibly read-write the electronic data bits through the optical means, and (ii) integrate optical and electronic components alongside at nanoscale to increase data capabilities. Recently, a variety of platforms, including but not limited to semiconductor devices,[137, 147] organic memory cells,[138, 141] emerging 2D materials[139, 143, 144] and resistive switching metal oxides,[136, 142, 148] have been extensively explored in order to engineer the high-performance optoelectronic memories. The majority of the aforementioned devices are built upon materials

with electronic-photonic coupling and operated under the strategy by exploiting the light-induced change of electronic properties in photo- and electro-active materials. A strong coupling of electronic and photonic properties is a prerequisite for those materials which makes the integration of both superior photoresponse and excellent electronic properties in one single material a great challenge. Therefore, despite the practical potential demonstrated so far, such device strategy has shown limits in terms of the efficient combination of key memory performance parameters such as high data write/read speed, long retention time, low fabrication cost and power consumption, long-term endurance, low fabrication complexity of scaling down, etc. with superior photoresponse behaviours like response efficiency, reversibility, etc. in one single platform.[149, 150] An alternative route employing hybrid integration of the separated high-performance photoactive materials and electronic memory materials in one device has recently emerged.[144, 149] In such a hybrid platform, the photoactive material could control the electronic properties of the electroactive component under the light input. This strategy could be advantageous to conventional optoelectronic devices as it can add light as a control parameter to those electronic memory materials even without any photoactive properties. Unfortunately, the nanoscopic integration of photoactive materials with high density and non-volatile electronic memory elements towards high performance optoelectronic memories still remains a great challenge. To build up practical optoelectronic memories which are manipulatable in nanoscale and of full light control, high-performance photoactive element and efficient integration method are thus required.

In this chapter, we demonstrate a hybrid optoelectronic memory by use of tip-enhanced bulk photovoltaic effect to realize the full optical control of FTJs. In particular, we chose atomic force microscopy (AFM) tip which is of typically 30 nm in radius as the nano-sized contact to enable the tip-enhanced BPV effect.[50] For all the measurements, a system comprising the conventional AFM and a bulk photovoltaic cell playing the role of the photo-responsive component was utilised. We experimentally demonstrate that three orders of magnitude of tunnelling

electroresistance (TER) switching in FTJs can be realised by solely using light control. Moreover, using the intrinsic advantages of the BPV effect, all optical write parameters, i.e. duration, intensity and polarity of the photocurrent-induced electric field, are controllable by the incident light intensity and polarisation, as well as the illumination position relative to the BPV cell electrodes. Therefore, the hybrid BPV cell/FTJ design proposed here opens a new window for photoprogrammable solid-state memory devices based on ferroelectric oxide structures.

5.2 Light controlled electric writing system

5.2.1 System configuration

The photo-driven AFM tip charge writing system is presented in Figure 5.1a. The photo-responsive component in the system is the $BiFeO_3$ (BFO) thin film which has been intensively studied as a model system for the BPV effect due to its favourable working window within visible light.[49, 50, 151] The photo-responsive cell and the electronic memory material, i.e., FTJs here, are connected with our photoelectric AFM (ph-AFM) system (see description of the ph-AFM system in Chapter 3.5.3). Note that the AFM cantilever used here is NSC-14 Pt (MikroMasch) with a typical tip radius of 30 nm. The photo-driven AFM tip charge writing system works in the 'short-circuit' regime wherein the photocurrent generated in the BFO is collected by the AFM tip after flowing through the FTJ. We note that the tip-enhanced photovoltaic effect in-principle works with any nanosized contact, and the AFM tip writing system adopted here is only a proof-of-concept demonstration of such an approach. High quality BFO thin films (~150 nm) consisting of pure 71º domain walls were epitaxially fabricated on (110)-oriented $TbScO_3$ (TSO) substrates, see Figure 5.1b and 5.1c. The BFO films are $(001)_{pc}$-oriented for which the pseudocubic crystallographic indexing is used here.

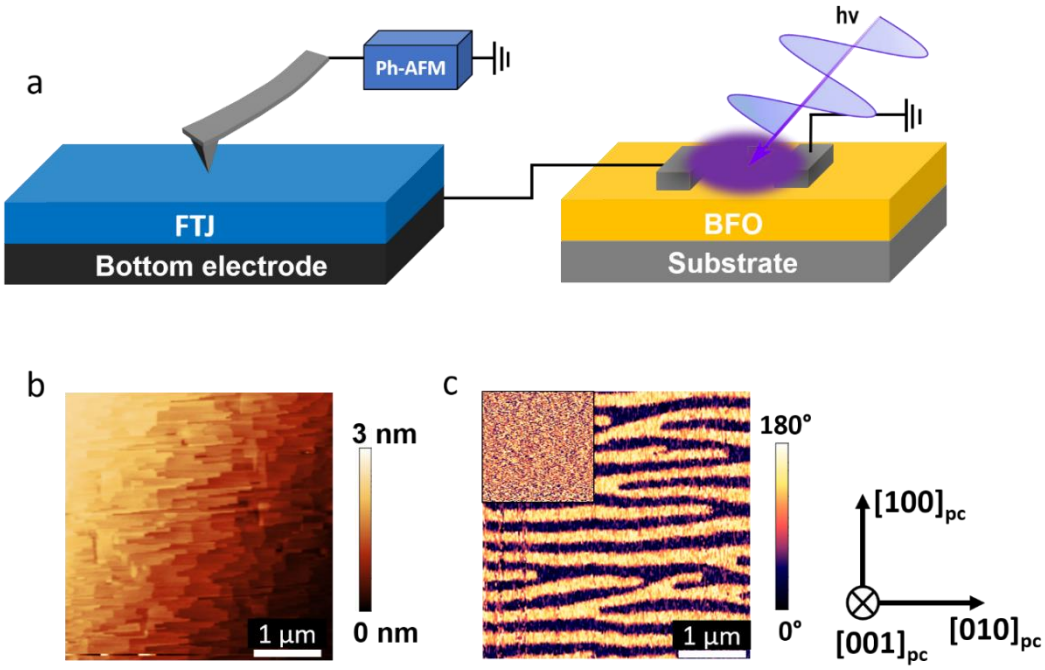

Figure 5.1: Description of the experimental setup. (a) Schematic drawing of the photo-driven charge writing system. (b) Topography of the BFO thin film. (c) In-plane PFM phase image showing the stripe-like 71º domain configuration. The inset shows the one-direction polarised out-of-plane phase. The pseudocubic crystallographic indexing with respect to the stripe domain wall is shown on the right panel.

5.2.2 Photo-electronic process in photoactive cell $BiFeO_3$

The typical bulk photovoltaic properties of the BFO film at certain light polarisation angles (ω) are presented in Figure 5.2. Photo Current-voltage (I_{photo}-V) characteristics of the BFO photocurrent generator were raised using a linearly polarised 405 nm laser with the intensity of 2 W cm^{-2} illumination. The generated photocurrent along different crystallographic directions of the BFO film and under various light polarisation angles relative to the current, i.e., $[100]_{pc}$ (ω = 0º) and $[010]_{pc}$ (ω = -45º), was collected using the AFM tip. The peculiar light-polarisation and crystallographic structure dependent photovoltaic behaviour is a manifestation

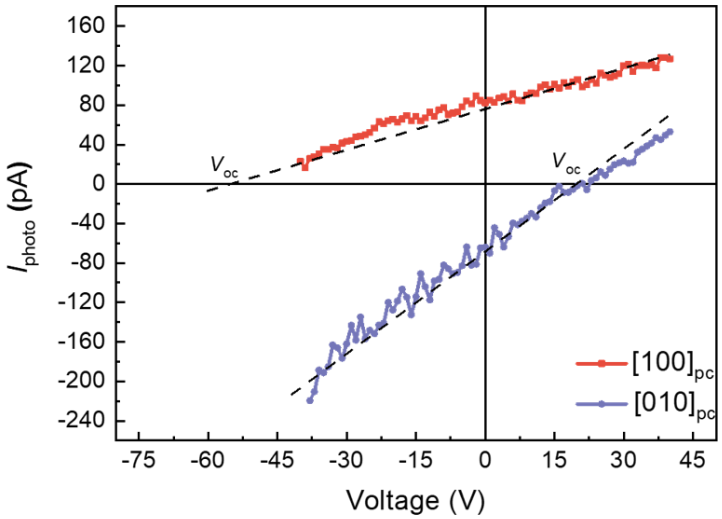

Figure 5.2: BPV properties of the BFO film with current flowing along $[100]_{pc}$ (ω = 0º) and $[010]_{pc}$ (ω = -45º) crystallographic directions, respectively. ω is the light polarisation angle.

of the BPV effect, which will be detailly discussed in the following. Unlike other photovoltaic materials, the ferroelectric photovoltaic materials exhibit very high open circuit voltage (V_{oc}) which is important for applying sufficient light-generated electric field on other electronic materials.[49, 52, 101] Rather high V_{oc} values of -53V and 23 V are obtained for photocurrent along $[100]_{pc}$ and $[010]_{pc}$ directions which guarantees that a high electric field underneath the tip is possible[52, 101] and indicates that the photocurrent can be effectively collected by the AFM tip despite its reduced dimension and the possible large contact resistance. It is worth noting that the negative photocurrent represents that the direction of the current thus electric field points towards the tip.

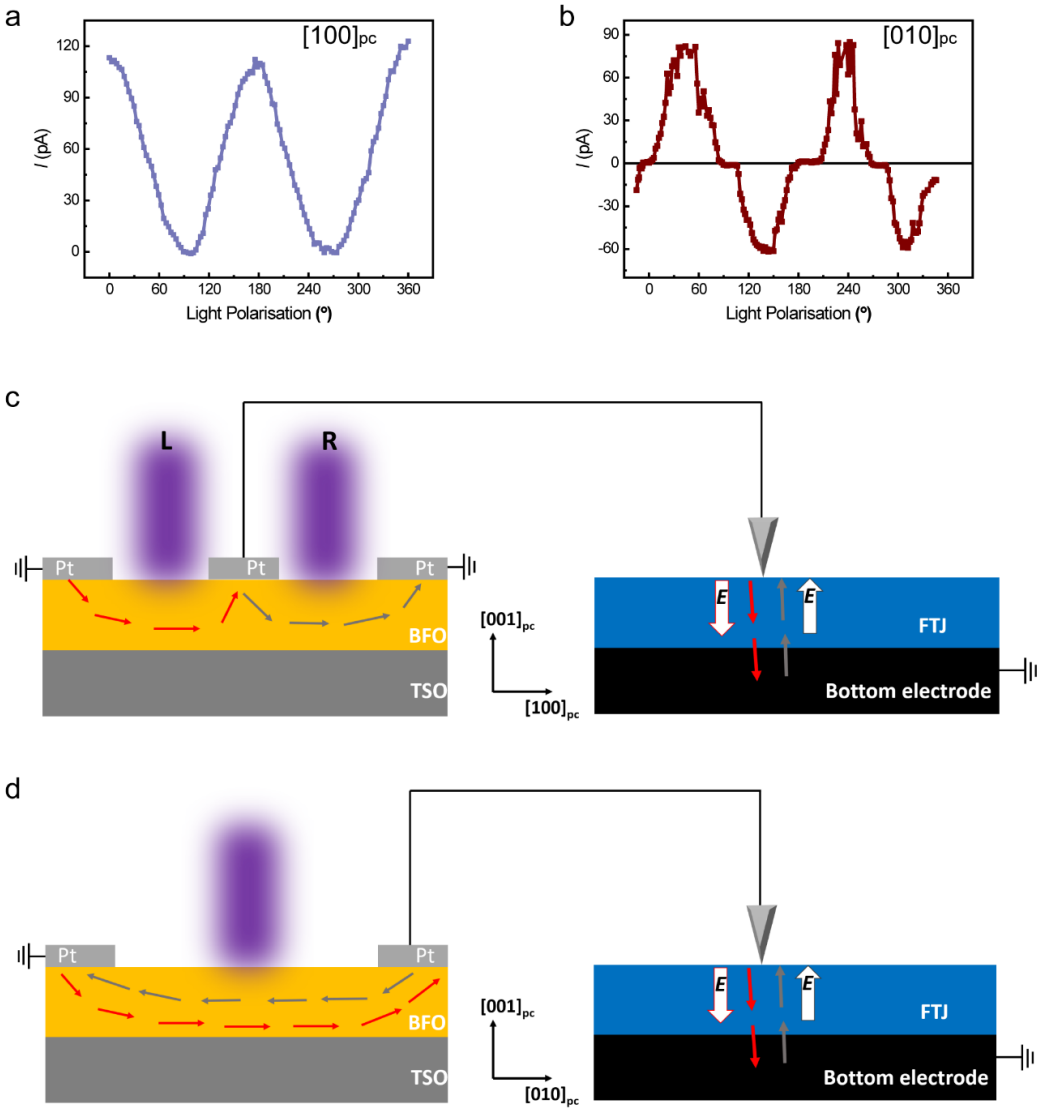

Figure 5.3: Photoelectronic process in BFO. The light polarisation angle dependence of the photocurrent in $[100]_{pc}$ (a) and $[010]_{pc}$ (b) crystallographic directions of BFO, respectively. Electrodes stripes placed along $[010]_{pc}$ (c) and $[100]_{pc}$ (d) on BFO and the resultant electric field generated on the tip.

In Figure 5.3, we exhibit the photocurrent along $[100]_{pc}$ and $[010]_{pc}$ directions of the BFO thin film respectively, as a function of the light polarisation. The I_{photo} along $[100]_{pc}$ shows a sinusoidal dependence on ω but with an offset which keeps

its value always of the same sign. In contrast, the polarity of the current along the $[010]_{pc}$ crystallographic direction switches depending on the ω. The light polarisation dependent photovoltaic properties can be described by the theory of the bulk photovoltaic effect, wherein the photocurrent is produced as a consequence of asymmetric microscopic processes of the photo-generated non-equilibrium carriers[46] and is directly related to the film crystallographic structure as reported.[45, 101, 151] A detailed explanation on this light angle and crystallographic direction dependent BPV current variation can be found in Chapter 2.4.1.

After showing that the photocurrent in BFO thin films runs always along a certain (preferred) crystallographic direction and its polarity can be determined by changing the electrode placement with respect to the crystallographic axis. Next, we demonstrate how to tailor the photocurrent direction and thus the induced electric field polarity on the AFM tip by changing the electrode arrangements on BFO thin film. Two different electrode configurations with respect to the BFO crystallographic directions were used here as shown in Figure 5.3c and 5.3d. For the electrode placement shown in Figure 5.3c, the current flows along $[100]_{pc}$. As the photocurrent is of the same polarity regardless the light polarisation angle (see Figure 5.3a), a three-electrode geometry can be used to change the polarity of the electric field at the AFM tip. Clearly, the photocurrent collected by the AFM tip is of opposite polarity when pointing laser at the left area (L) or right area (R). This feature could be useful for light position dependent optoelectronic applications. Another electrode placement is a two-electrode geometry as shown in Figure 5.3d, in which the photocurrent flows along the $[010]_{pc}$ crystallographic direction. Photocurrent in this situation can be conveniently changed in terms of both amplitude and polarity by rotating the light polarisation as shown in Figure 5.3b. Therefore, the photocurrent generated electric field at the AFM tip is also polarity switchable by tuning the light polarisation.

5.2.3 Working mechanism for light controlled AFM writing

Having established the fundamental BPV properties of the BFO film, we now

explain how our system works for the light controlled charge writing. In a conventional system in which a device is connected to the photovoltaic cell, a matching of the resistance values of device and photovoltaic cell is prerequisite to ensure that sufficient voltage can be applied on the working device. Materials showing BPV effect, e.g. ferroelectrics, are generally of very high resistivity.[49] Therefore, the electric field applied to normal solid-state memory materials with a relatively low resistivity compared to that of ferroelectrics is limited. However, in our system, such problem could be alleviated, as the electric field generated by the BPV current can be strongly enhanced beneath the nano-size AFM tip. As shown in Figure 5.4, the photocurrent collected by a 200 μm planar electrode and AFM tip

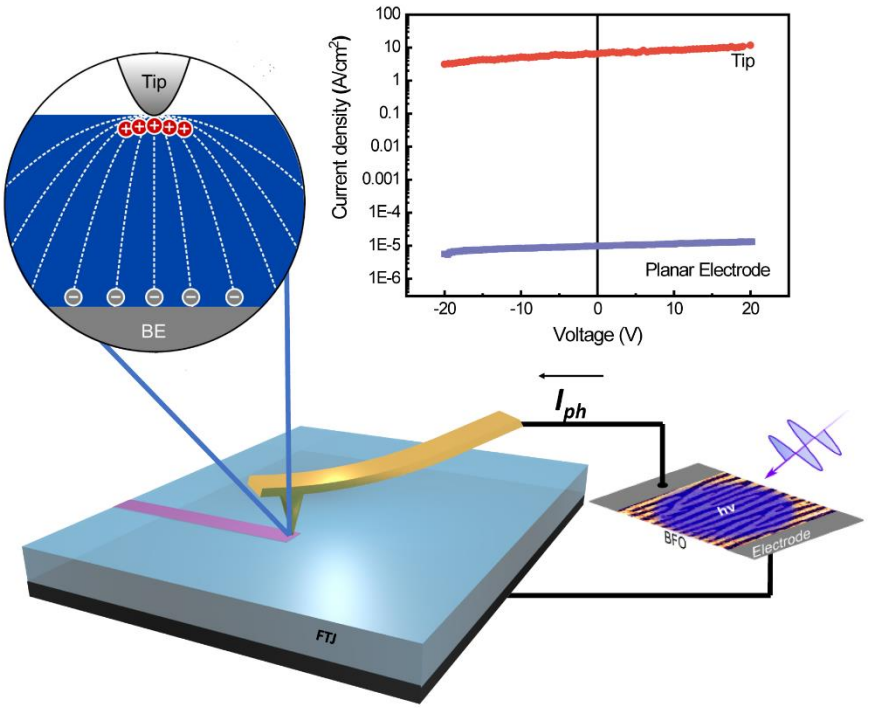

Figure 5.4: An artistic schematic of the working principle of the tip-enhanced BPV enabled charge writing. Upper right inset shows the photocurrent curves collected by the tip and the planar electrode, respectively.

(typically of 30 nm in radius) pair is with a dramatically amplified current density which is almost seven orders of magnitude higher than that collected by the 200 μm × 200 μm planar electrode pair at the same gap distance. As well known, while operating a device in a constant current mode, the local gradient potential, i.e. electric field, is proportional to the local current density.[152] With BFO BPV cell under light illumination, the photo-excited non-equilibrium carriers spontaneously move along the preferred crystallographic direction without applying any external electric field, thus providing a constant current. For the electric field induced by the photocurrent, we have $E_{pv} = (JR - V)/d$ where E_{pv} is the photocurrent induced electric field, *J* is the current density, *V* is the applied voltage and *d* is the thickness. *V* should be zero in our case, thus it is obvious that a non-zero electric field is presented due to the photocurrent.[52] As schematically depicted in the upper left panel of Figure 5.4, an enhanced electric field is expected to be generated beneath the nano-size AFM tip by the photocurrent, albeit rapidly decreasing with increasing the lateral size. Following the analysis of electric field at a point contact made by Lampert et al.,[153, 154] there is a space-charge-limited region in the vicinity of the tip contact area. Considering the ultrathin thickness of the our FTJs, we could assume that the entire ferroelectric barrier underneath the tip can be treated as the space-charge-limited region. In this region, we have $I = 2\pi e\mu n_i r^2 E$ where *I* is the current, μ is the electron mobility, n_i is the injected carriers, *r* is the radius of the spherical geometry of the tip contact position, $E = E(r)$ is the electric field. The field distribution in this particular spherical geometry can be estimated by solving the Poisson equation assuming that the free charges are in thermal equilibrium, a trap-free insulator and a diffusion-free transport mechanism. The boundary condition is at a position away from the contact region: $r = r_{tip}$, $E = 0$. The photovoltaic voltage is given by integrating the field over the entire distance between the two electrodes: $V = \int_{r_-}^{r_+} E_r dr$. By solving the Poisson equation for a pure photocurrent flow and trap-free insulator with the boundary condition, we can get: $E = (\frac{I}{3\pi\mu\varepsilon}\frac{1}{r})^{1/2}$ here ε is the dielectric permittivity of the material.[153]

Therefore, the amplitude of the electric field is estimated to be enhanced by the factor of $[I_{sc}/r_{tip}]^{1/2}$, where the r_{tip} is the radius of the AFM tip. As analysed by Yang et al., the maximum electric field at a tip of 30 nm in radius can be as high as 1200 kV/cm which is much higher than the typical coercive field of perovskite ferroelectric oxides (normally around 100 kV/cm).

5.3 A hybrid light-controlled resistive switching device

5.3.1 Position-dependent photo-driven tip writing of ferroelectric tunnel junctions

High-quality FTJs consisting of 3 nm $PbZr_{0.2}Ti_{0.8}O_3$ (PZT) ferroelectric tunnel barrier and 20 nm $La_{0.67}Sr_{0.33}MnO_3$ (LSMO) bottom electrode were used for the experiment. The FTJ was connected to BFO photovoltaic cell with the ph-AFM. As shown in Figure 5.3, there are two electrode geometries with respect to the BFO crystallographic directions which can be used to control the photocurrent due to the fact that the photocurrent direction by BPV is merely determined by the BFO crystallographic structure. In this section, we demonstrate the case with electrode configuration shown in Figure 5.3c where the photocurrent always flows along the $[100]_{pc}$ crystallographic direction. A detailed electrode arrangement can be found in Figure 5.5a. Among these three electrodes, two areas of the BFO surface can be defined, i.e. Left (L) and Right (R) areas. Illuminating the L area, the photocurrent flows from the BFO into the FTJ then the AFM tip, we define the photocurrent in this case as of negative polarity (see Figure 5.5b). In contrast, photocurrent of the positive polarity can be found when illuminating the R area (see Figure 5.5c). Therefore, with the three-electrode geometry, the polarity of the photocurrent thus the electric field beneath the AFM tip is set by laser illumination on different BFO areas with respect to the electrodes.

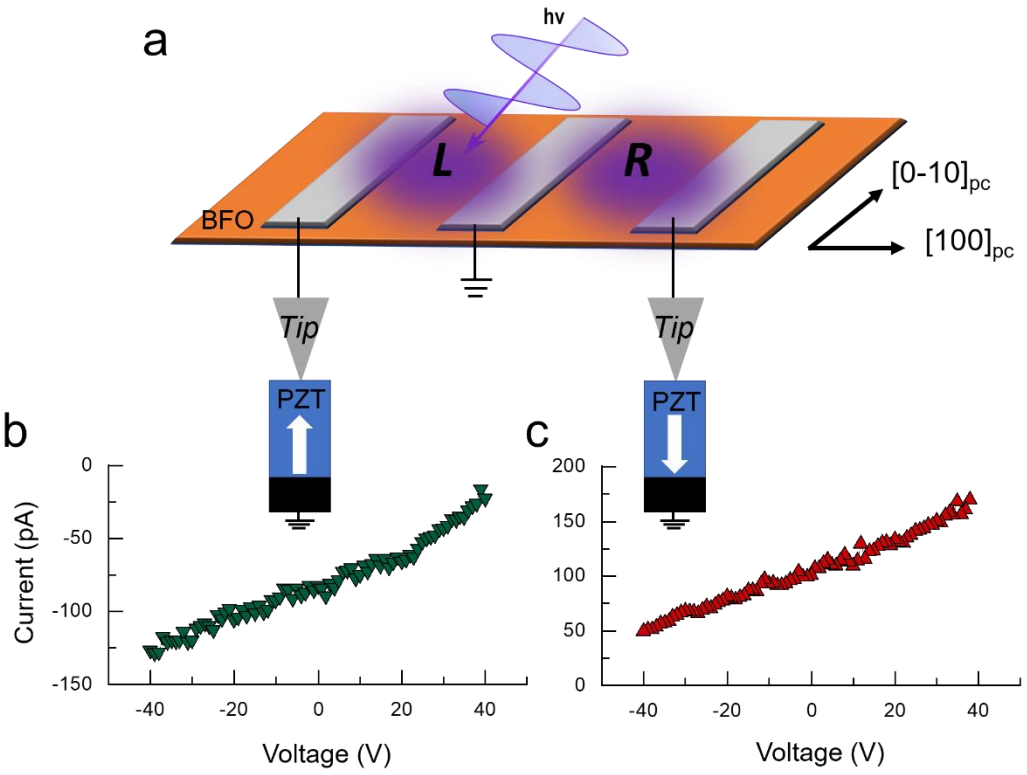

Figure 5.5: Photocurrent collected in an FTJ connected to the BFO. (a) Schematic drawing of the electrode geometry with the photocurrent flowing along $[100]_{pc}$ direction. The BFO generated photocurrent collected from the FTJ with left (L) and right (R) electrode geometries, respectively. The illumination light used here is set at $\omega = 0^{o}$.

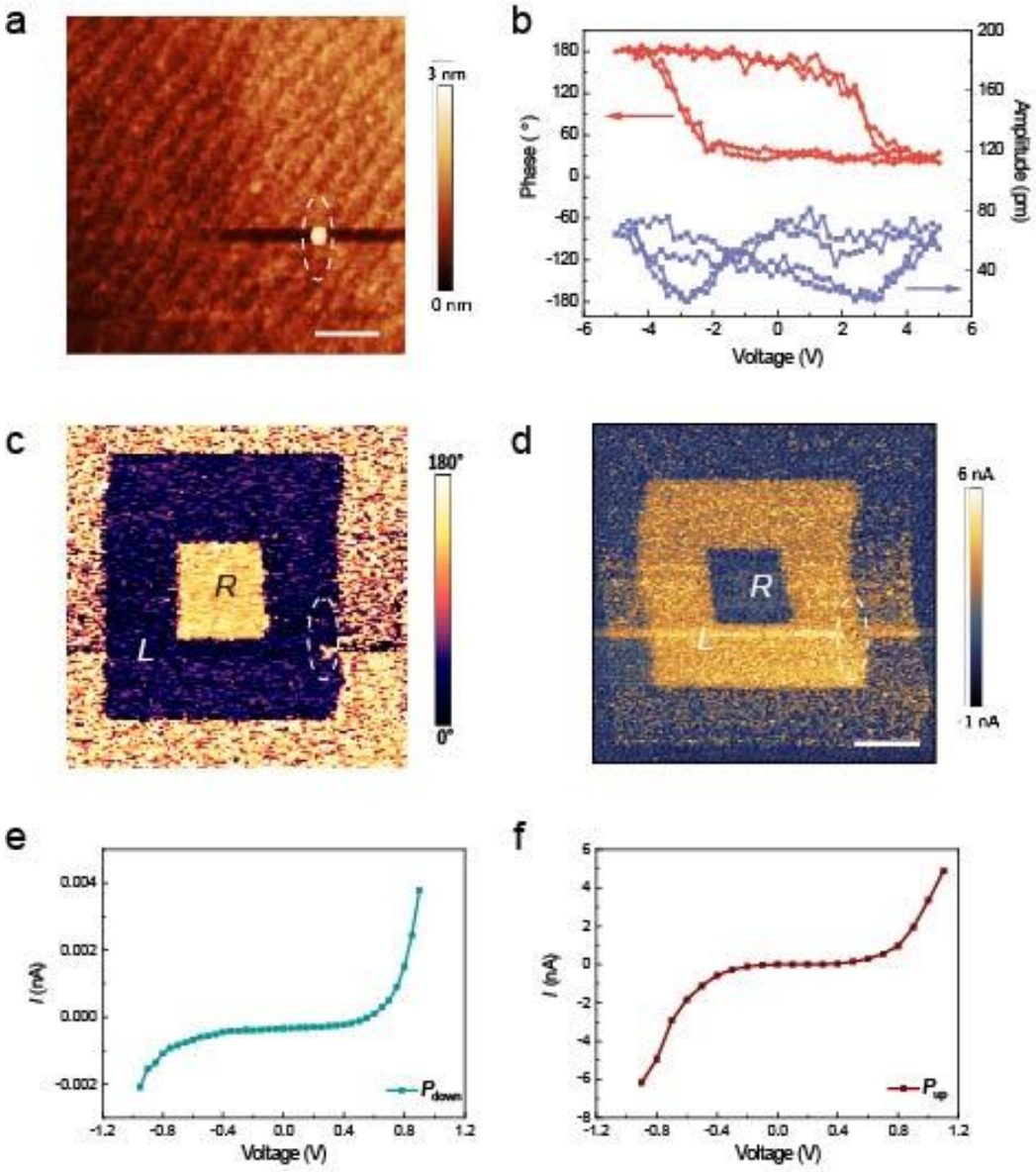

Figure 5.6: Illumination position dependent writing of the FTJ. (a) The topography of the PZT/LSMO heterostructure. (b) The PFM hysteresis loop of the PZT film indicating the ferroelectric nature. PFM phase image (c) and current mapping in CFM mode using 0.6 V reading bias (d) of the FTJ after photo-driven AFM scans with positive (R) and negative (L) photocurrent modes, respectively. *I-V* curves collected from the downward (e) and upward (f) ferroelectric domains, respectively.

We next performed the photo-driven AFM tip scanning on the FTJ. As shown in Figure 5.6a, the PZT/LSMO heterostructure exhibits atomically smooth topography. Piezoresponse force microscopy (PFM) hysteresis loops shown in Figure 5.6b indicate the excellent ferroelectric properties of the thin PZT layer. We then scanned the PZT surface using the AFM tip under the contact mode with the photocurrent from the BFO cell flowing through the PZT into the AFM tip. During the scanning process, photocurrent with positive or negative polarity by directing the light on R or L areas of BFO was applied for different scanning steps. It must be noted that NO external voltage or current was applied to the AFM system but only the photocurrent from the BFO cell during the PZT polarisation writing scans. After the scanning process with photocurrent on, we performed conventional PFM and current mapping of the scanned area of the PZT as shown in Figure 5.6c and 5.6d, respectively. Note that no visible change of the PZT surface was observed after the photo-driven scanning process. As expected, a clear 180º phase contrast is observed which reveals that two domains of antiparallel ferroelectric polarisations have been written on the PZT. This writing effect, i.e. ferroelectric switching, is solely due to our photo-driven AFM tip scanning. Current mapping of two antiparallel ferroelectric domains shows a giant resistance contrast associated with the two opposite ferroelectric polarisation directions, which manifests the well-known TER effect in FTJs.[16, 20, 133] The light controlled giant FTJ resistance switching is further corroborated by *I-V* curves acquired from both ferroelectric polarisation down and up domains as shown in Figure 5.6e and 5.6f, respectively. Three orders of magnitude of resistance switching was achieved using the light controlled writing which is comparable to the TER of previous reports on electric writing of FTJs using AFM.[16, 20] Overall, the photo-driven AFM tip scan indeed can switch the ferroelectric polarisation as predicted by the light-enhanced BPV effect.

5.3.2 Light polarisation-dependent photo-driven tip writing of ferroelectric tunnel junctions

Further on, we show a hybrid device with photo-programmable memory function based on the combination of the FTJ and tip-enhanced BPV effect. The experimental setup is shown in Figure 5.7a. As mentioned before, reversible switching is key to the full light control. A more convenient method to control the photocurrent polarity is to tune the incident light polarisation by which intensity and polarity of the electric field at the AFM tip can both be controlled, see Figure 5.3b. While placing the electrodes on BFO along its $[100]_{pc}$ direction (see Figure 5.3d), the light polarisation switching from -45° to 45° can induce the reversible polarity switch of the photocurrent thus the electric field beneath the tip as shown in Figure 5.7b. With the nano-size contact, i.e. conductive AFM tip here acting as the top electrode on the PZT surface, we continuously reversed the PZT ferroelectric polarisation upward and downward by simply switching the light polarisation between 45º and -45º repeatedly. Following each optically controlled switching, we recorded the resistance of the FTJ as shown in Figure 5.7c. The resistance ON/OFF ratio almost three magnitudes of amplitude can be clearly seen due to the giant TER effect of the FTJ. By locating the AFM tip at different positions, a series of nanoscale FTJs were characterized, as shown in Figure 5.7d. Such a property may be useful to address the scalability issue of the memory devices as the nanosized junctions written by the AFM tip could act as a matrix of nanomemories. To check the retention performance of those light controllable FTJs, we examined the FTJs resistance states as a function of time. As shown in Figure 5.7e, the photo-driven AFM tip writing process is truly non-volatile, where the retention of the written FTJ exceeds 40 min, which is the average stability of our AFM system.

The above results unambiguously demonstrate that the PZT polarisation can be full light-controlled switched by the described setup, which verifies our hypothesis that the electric field originating from the BPV photocurrent in the ‘short-circuit’ regime

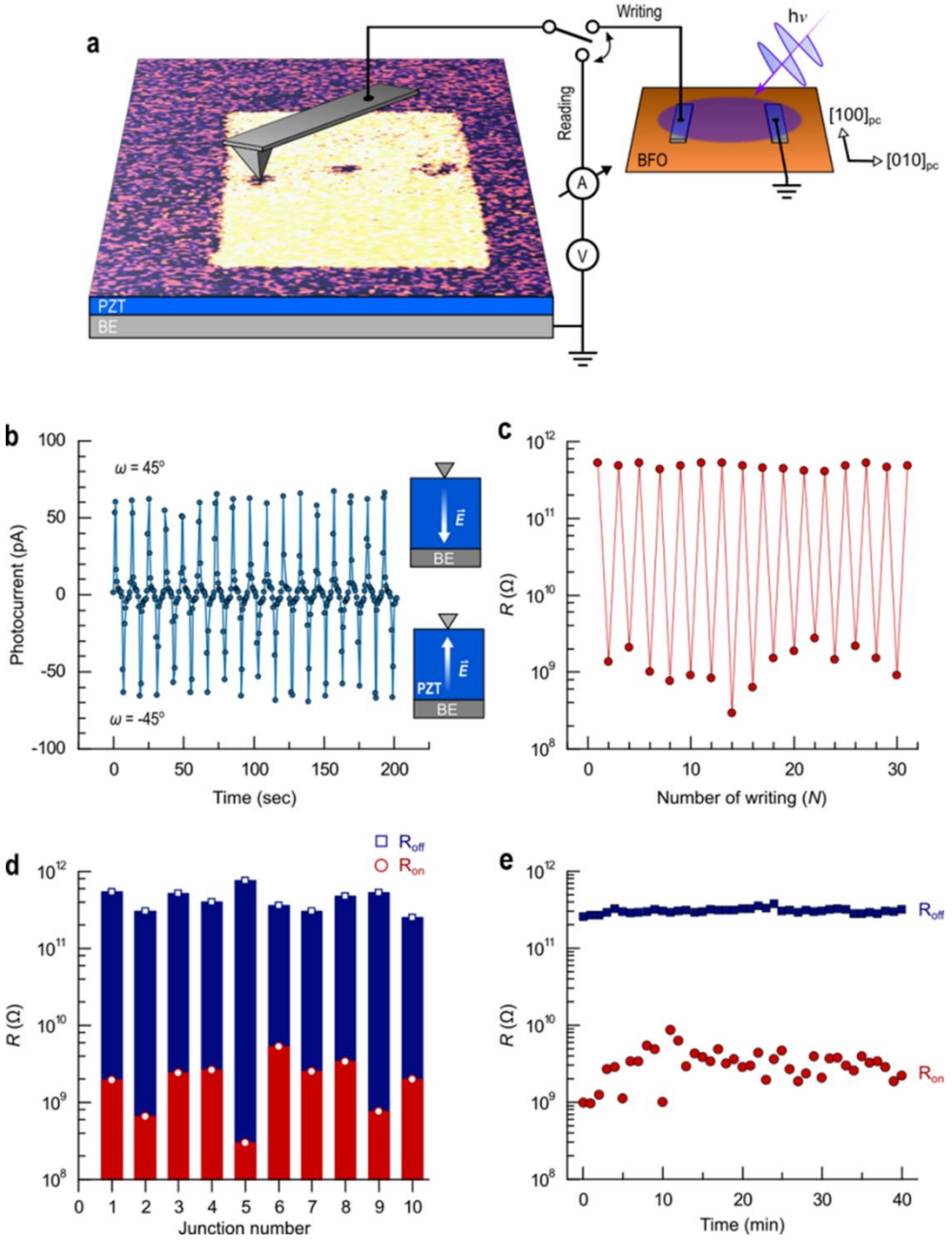

Figure 5.7: A light-controlled FTJ. (a) Schematic illustration of the device showing the light-controlled resistance state writing and the electrical reading. The contrast in the PZT layer PFM image shows the upward and downward ferroelectric polarisations. (b) Switching the polarity of photocurrent by rotating the light polarisation between -45º and 45º. (c) The resulting resistance states in the FTJ after the photo-driven AFM tip writing, indicating a resistive switching memory function. (d) Resistance of ON and OFF states by light-controlled writing among 10 junctions. (e) Resistance retention properties of the FTJ within 40 minutes.

further enhanced by the nanoscale tip-contact geometry is sufficient to exceed the coercive field of a hard ferroelectric such as PZT. Hence, the above photo-driven AFM tip writing technique can be considered as a generic approach for nanoscopic patterning of solid-state materials allowing optoelectronic memories.

5.3.3 Photocurrent generation speed

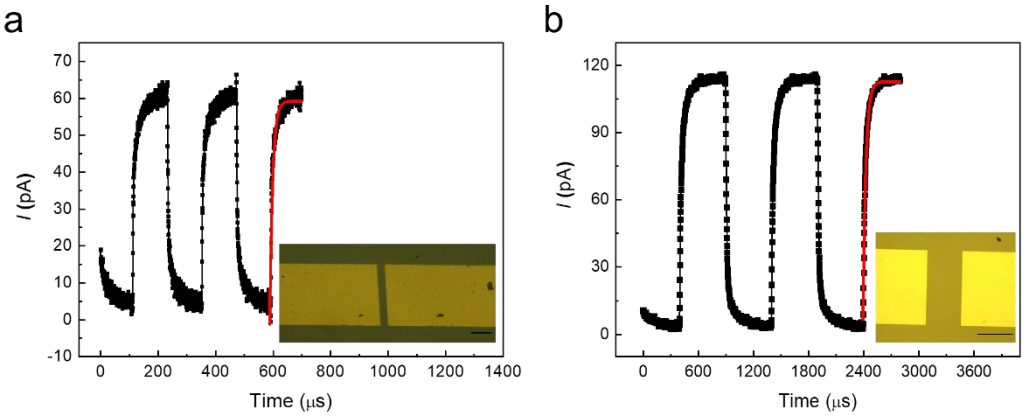

Figure 5.8: Photoresponse properties of the BFO thin film BPV cell. The photocurrent response properties of 115 μm×15 μm channel (a) and 450 μm×235 μm channel (b), respectively. The red line presents the fitting by equation (5-1). The insets show the electrode geometry. Scale bar: 40 μm in (a) and 200 μm in (b).

The photocurrent generation speed of the BPV cell is crucial to future optoelectronic device as it decides the response time of the whole system. Here, we show that the photocurrent amplitude and generation time can be tuned by design of the BFO film BPV cell. Two different electrode geometries on the same BFO film are studied here as examples. As shown in Figure 5.8, the gap × electrode width of photo-responsive channels is 115 μm×15 μm and 450 μm×235 μm, respectively. During the measurements, the laser parameters used for the two devices are identical. The photocurrent (I_{photo}) properties are different in terms of the saturated current amplitude (I_s) and response time scales. We can describe the photocurrent generation process using the equation:

$$I_{photo} = I_s[1 - e^{-t/\tau}] \qquad (5\text{-}1)$$

where *t* is the elapsed time after light on and τ is the photo carriers generation time constant. By fitting the photocurrent-time curves with the above equation, we can obtain the time constant values are 10 μs and 33 μs for the electrode geometry in Figure 5.8a and 5.8b, respectively. Therefore, the photo-responsive cell used in the photo-driven AFM writing system can be rationally designed to achieve faster response speed and higher photocurrent for future applications. We note that in practical measurements, there are two aspects which could affect the obtained photoresponse time characteristics. The first one is related to the measurement set-up, the measured time-dependent photocurrent characteristics can be affected if the response time of the circuit (normally the *RC* time of the measurement circuit) is slower than the photocurrent response time of the BFO.[155] The other factor is due to intrinsic physical properties of BFO films. In BFO thin films, the photocarrier generation is not simply a band-band excitation process but related to the shallow energy levels in the bandgap involving the complex trapping and thermal activating process.[155, 156] The shallow energy levels could be influenced by the domain structure, defects distribution, strain state, etc. of the BFO.[156] Here, by altering the electrode geometry, the effective area of the BFO film contributing to the photoresponse could be changed regarding the various complex domain structure, defects level, etc. Hence, the photoresponse time properties of the BFO devices are changed.

5.3.4 Dependence of polarisation switching on light duration and intensity

To further test the writing feasibility of the photocurrent generated electric field underneath the AFM tip, we conducted photocurrent intensity-duration dependence of the written domains of PZT films. Here, we used three different illumination conditions as shown in Figure 5.9a. As can be seen from Figure 5.9b and 5.9c, under the AFM writing of the same photocurrent-on duration, different remnant ferroelectric domains were formed as a function of the laser power, i.e., the different

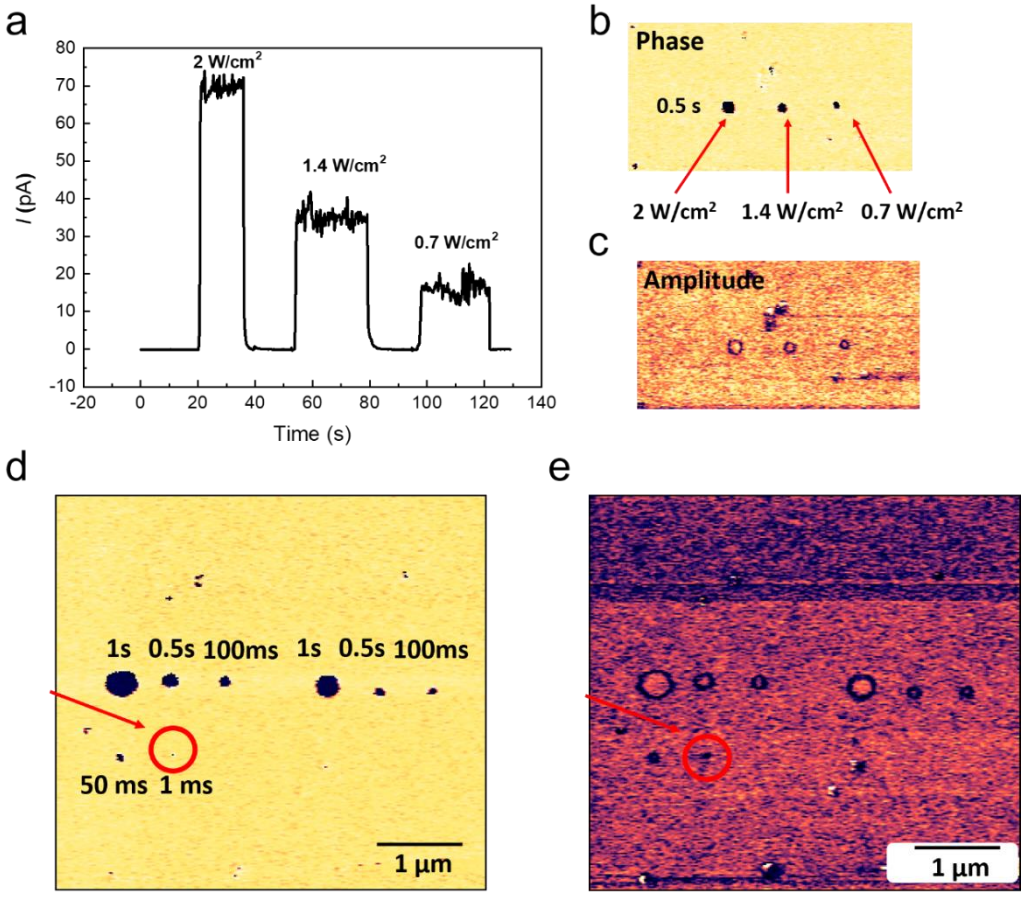

Figure 5.9: Light illumination power and time controlled PZT polarisation switching. (a) Photocurrent of the BFO film as a function of the laser intensity. Phase (b) and amplitude (c) PFM images of dot-like ferroelectric domain formation in PZT by applying photocurrent generated electric field pulses with different strength and constant duration through the AFM tip. The phase (d) and amplitude (e) images of the AFM tip mediated domain formation by applying photocurrent generated electric field with different duration.

photocurrent generated electric fields. This is similar to commonly observed AFM tip mediated ferroelectric domain switching by applying voltage pulses with different amplitude and duration.[157] A more detailed photocurrent generated electric field duration dependent ferroelectric domain switching is shown in Figure 5.9d and 5.9e. Under the same 2 W cm^{-2} illumination (identical photocurrent),

various switched domain sizes are observed by applying the photocurrent generated electric field with different durations. The observed domain formation can be attributed to the fact that ferroelectric polarisation switching commonly proceeds by nucleating reversed domains which subsequently expand, which is influenced by the electric field amplitude and time.[157, 158] These results again verify that the photo-driven AFM tip writing induced polarisation switching in PZT is a pure electric field effect, despite that the electric field on the tip is generated and controlled by the light.

We note that the light power and duration will not necessarily influence the device performance of the light controlled FTJ memory, although the remnant ferroelectric domain size is indeed affected by duration and amplitude of the photo-generated electric field. The reason is that the ferroelectric switching or domain wall velocity is decided by the material itself.[158] Therefore, the response speed of a BPV/FTJ hybrid device should be decided by the current rising time of the BPV cell and the fastest switching time of the FTJ. For example, by putting the tip still on the PZT surface, we found that even a very short laser pulse (100 μs) can induce the polarisation switching by measuring the resistance of the FTJ. However, this switching was not visible from PFM imaging due to the small ferroelectric domain size and the limit of the scanning resolution of the PFM. Overall, in this section, we demonstrated that even a very small current (~ few pA) under a moderate laser intensity can induce an electric field exceeding the coercivity of the PZT film, as shown in Figure 5.9b. Moreover, the fastest photoresponse time of our BFO BPV cell namely the writing time of the FTJ memory device obtained is at ~10 μs range and can be further optimised to meet the fast FTJ switching speed (~ns)[128] by rational device design of the photoactive component BFO. Therefore, the tip-enhanced BPV effect writing of FTJ memory could be appealing for optoelectronic memory applications in terms of low power consumption and fast operating speed for the photo-driven data writing.

5.3.5 A proposed integrated optoelectronic memory

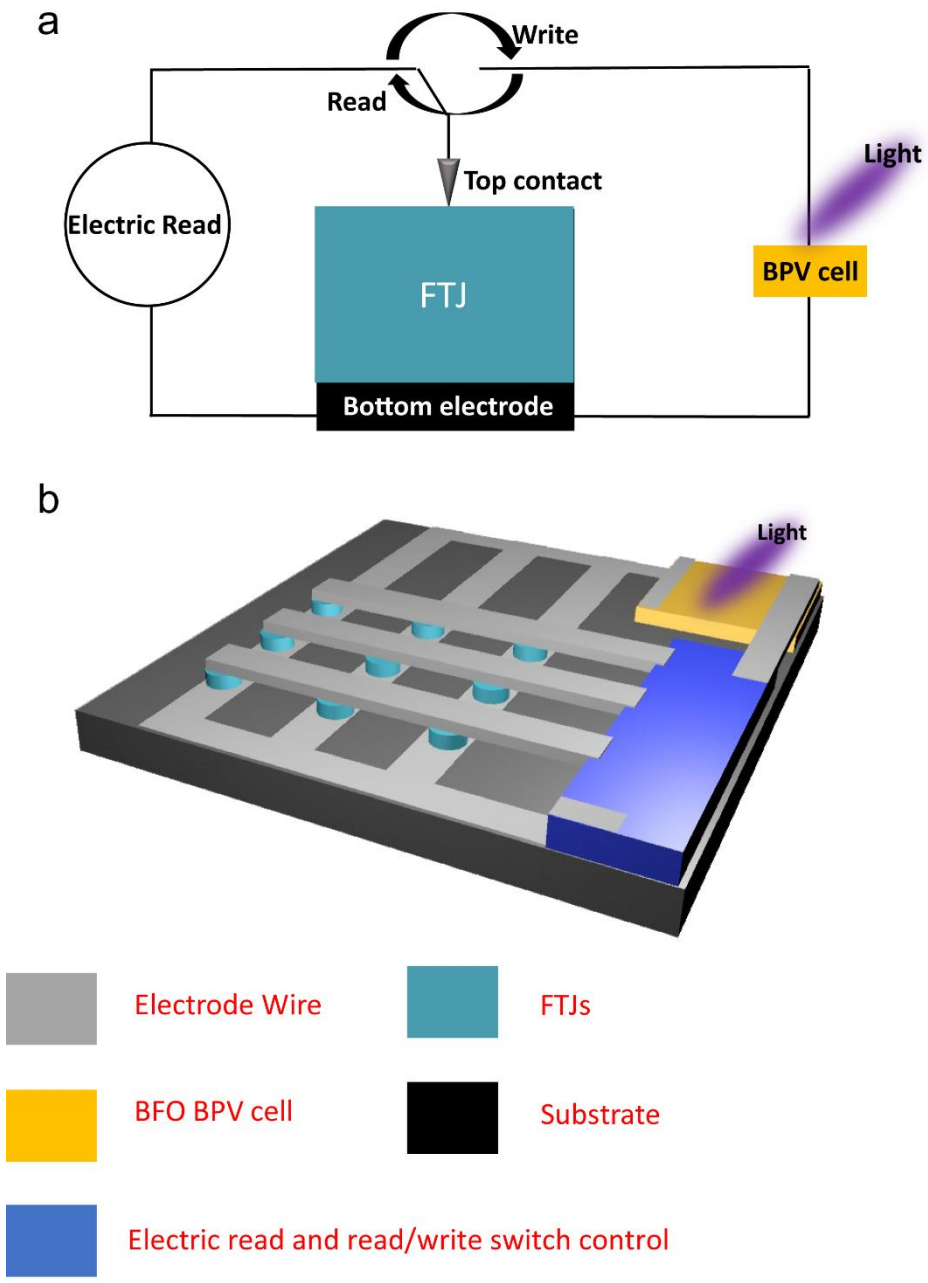

Figure 5.10: A proposed integrated light-controlled memory. (a) The working principle for an individual light-controllable FTJ. (b) An artistic illustration of an integrated optoelectronic memory chip with cross-bar memory cell structure.

In this section, we propose a hybrid light-controllable memory based on the above results. The basic operation of an individual light-controllable FTJ is shown in Figure 5.10a. While the electronic component is under the light-controlled writing process (photovoltage provided by BPV cell) e.g., light information store, light sensing and so on, the electric read part should be in the standby mode and disconnected from the electronic load. At the electric read mode, the circuit should be switched to be connected to the electronic component and the system measures the electronic property change of the electric load after the light-controlled writing process. After the read process, the circuit should be switched back to the write mode waiting for the new round of light input. Note that the top contact at the electronic component could be any electrode at nanoscale. Using such an operating protocol, a prototype light-controllable FTJ with the BPV cell (Figure 5.10b), electronic component and the read/write circuits integrated together is realised.

5.4 Summary

In this Chapter, we have demonstrated a hybrid optoelectronic memory based on the FTJ by using of tip-enhanced bulk photovoltaic effect. Using the strong, polarity switchable and strength tuneable light-induced electric field at the nano-sized contact in combination with the AFM probe technique, we realised the photoprogrammable writing of the FTJs in nanoscale. We further present the relationship between the FTJ switching and the photocurrent amplitude/duration. Finally, we come up with a novel design of the integrated optoelectronic memory platform based on the FTJ and BPV cell.

Chapter 6

Flexible memristors made from transferable ferroelectric oxide nanomembranes

As demonstrated in the previous chapters, ferroelectric tunnel junction (FTJ) based memristors exhibiting continuously electric field controllable resistance states have been considered as the promising candidate for future high-density memories and advanced neuromorphic computational architectures. In this chapter, we present the integration of centimetre-scale single crystalline FTJs on flexible plastic substrates, by water-etching based epitaxial oxide nanomembrane 'grow-transfer' method. The obtained highly flexible FTJ membranes retain the single-crystalline structure along with stable and switchable ferroelectric polarisation as the grown-on single crystal substrate state. Through electric characterisation, we show that the flexible memristors i.e., FTJs on plastic substrates, present high speed and low voltage mediated memristive behaviours with resistance changes over 500% and are stable against shape change. Moreover, 'grow-transfer' method enabled transfer of epitaxial functional oxide structures including ferroelectric and ferromagnetic oxides may pave the way for novel flexible oxide based-electronics.

6.1 Motivation: a flexible ferroelectric tunnel memristor

As discussed in Chapter 2.5, flexible electronics have aroused extensive interests from the research communities of material science, engineering, physics and so on. After the booming development in the past few years, flexible electronics are now on the verge of an innovative breakthrough towards smart, multifaceted, interacting systems comprising functions such as sensing, communication, information storage and processing, all in one unit, which request the advanced functional components.[67, 77, 159-162] A key building block of such multifunctional devices is the computing cell for which a lightweight, high performance and even wearable memory element is required. Despite the significant efforts to fabricate memory

devices on flexible substrates, there are continuous requests of new devices and architectures with superior properties in terms of the key memory performance parameters such as low-power consumption, high data density, non-volatile, fast operating speed, etc. As demonstrated in previous chapters, memristors or memristive devices exhibiting continuously electric field controllable resistance states have long been considered as a promising candidate, which could fulfil the aforementioned requirements.[5, 163, 164] Memristors made out of myriad oxides thin films are usually enabled by a process called forming, which creates conducting filaments in the film through the voltage induced breakdown.[163, 165, 166] In most cases, the conducting filaments are attributed to the ion migration and redox processes. Unfortunately, the sophisticated nature of the ionic process leaves the operating mechanism of those memristors not fully understood.[163] Moreover, it is generally agreed that this kind of memristor suffers from intrinsic switching uniformity and performance variability.[166]

The successful commercialisation of any application requires a robust and predictive understanding of its working principles. In this regard, the FTJ memristors operating on purely electronic effect, may be an ideal choice due to its clear working mechanism, i.e. the memristive resistance behaviour is corresponding to the electric field controllable ferroelectric domain configuration.[5, 128, 133, 167] Moreover, the FTJ has demonstrated the capability of scaling down to less than 5 nm in thickness and achieving the ultrafast, low energy, non-volatile electrical modulation. Along with the predictive, well-established understanding of operating mechanism, ferroelectric tunnel memristors are thus regarded as a highly promising candidate for the implementation of future high density memory applications and the advanced neuromorphic computational architectures.[5, 128] As for flexible electronics, the successful fabrication of ferroelectric tunnel memristors on soft substrates could present an essential leap towards the aforementioned high performance flexible memories. A feasible way to achieve the mechanical flexibility of the FTJ devices is to integrate such heterostructures on flexible polymer substrates. Unfortunately, as discussed in Chapter 2.5, the synthesis of

ferroelectric tunnel memristors requires the high-temperature epitaxial growth on rigid single-crystal substrates in order to ensure that non-volatile and switchable polarisation could persist in the ultrathin ferroelectric layer. The strict growth conditions thus strongly hamper the development of ferroelectric tunnel memristors towards flexible electronics applications. Moreover, as it is believed that freestanding thin film is released from the strain imposed by the growth substrate, whether the spontaneous ferroelectric polarisation can be preserved in the freestanding ultrathin ferroelectric membranes remains an open question.

In this chapter, we integrated single-crystalline $BaTiO_3$ (BTO)/$La_{0.7}Sr_{0.3}MnO_3$ (LSMO) ferroelectric tunnel memristor heterostructures on plastic substrates for ultrathin ferroelectrics based flexible memory applications. We found that BTO single-crystalline membranes of only 3.6 nm in thickness can still preserve the switchable ferroelectric polarisation after the lift-off and exhibit over 500% tunnelling electroresistance (TER) at room temperature. Regarding the epitaxial oxide heterostructure transfer, we adopted a 'grow-transfer' strategy based on the water-soluble $Sr_3Al_2O_6$ (SAO) layer which can be epitaxially grown on $SrTiO_3$ (STO) substrate. Apart from the transfer of FTJs, several single crystalline oxide materials were grown on SAO/STO and successfully lift-off to form the transferable oxide nanomembranes, which suggests that the SAO based 'grow-transfer' method can be further exploited for fabrication of a wide range of functional oxides nanomembranes.

6.2 Water soluble perovskite oxides enabled grow-transfer method

6.2.1 Fabrication of $Sr_3Al_2O_6$ film

As introduced in Chapter 3.2.5, SAO is a hygroscopic oxide perovskite which can rapidly dissolve in water. Therefore, inserting SAO film between the substrate and overlayer can enable the selective etching of SAO and release the overlayer of interest. Next, we first demonstrate the successful fabrication of SAO thin film on

STO. Due to its structure similarity to STO (001) substrate, the SAO layer can be epitaxially grown on STO by PLD. Detailed growth parameters can be found in Chapter 3.2.6. The structure properties of a 30 nm thick SAO film on STO are summarised in Figure 6.1 and 6.2. As shown in Figure 6.1a, the topography of the as-grown SAO shows flat surface which mimics the step-and-terrace of the STO substrate indicating the excellent epitaxial growth. To investigate the microstructure of the SAO film, we performed cross-sectional aberration-corrected scanning transmission electron microscopy (STEM) imaging along the [001] crystallographic direction using annular dark field (ADF). As displayed in Figure 6.1b, the STEM image shows that the SAO layer is coherently grown on STO and of a unique rhombus-like structure. Such a unique structure suggests the well-growth of the SAO which is structurally stable against the so-called 'thermal degradation'.[168] The formation of the rhombus-like structure is because of that the crystal structure of SAO is slightly deviating from the ABO_3 perovskite with the B-site cations alternating between Sr and Al atoms and from the ordered oxygen and cation vacancies.[102, 168] The atomic weight difference from such cation alternating thus results in a bright and dark contrast as the appeared 'rhombus-like' structure.

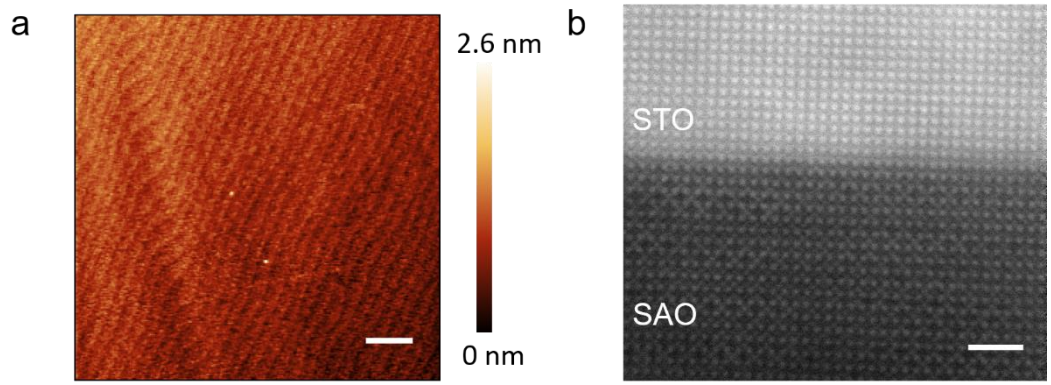

Figure 6.1: AFM and STEM investigation of SAO film. (a) AFM topography image. Scale bar: 500 nm. (b) ADF STEM image of the SAO. Scale bar: 2 nm.

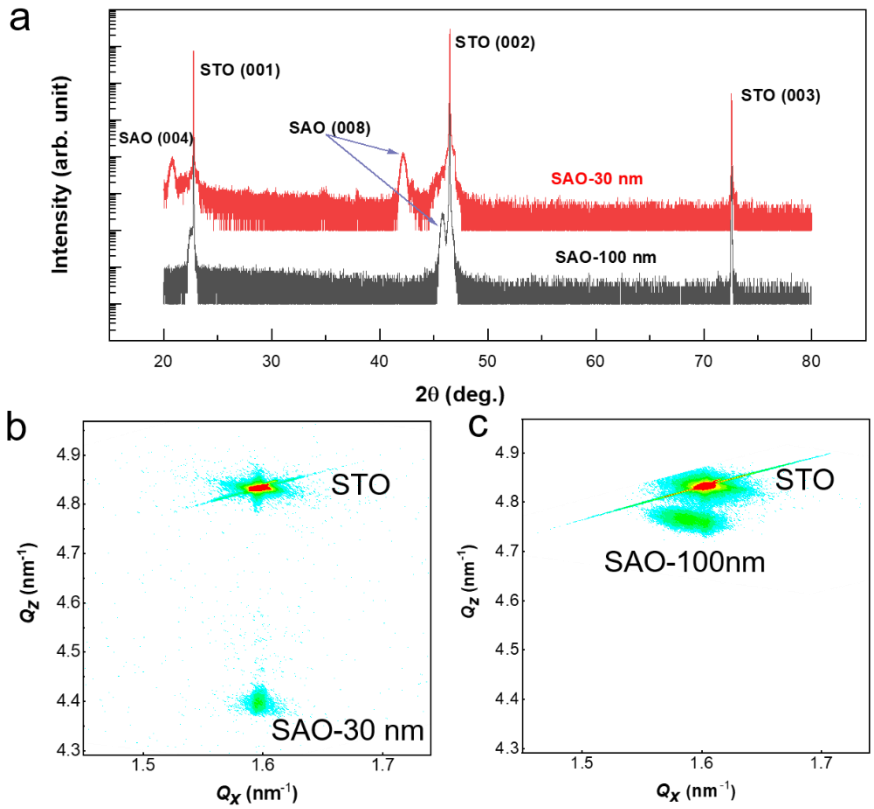

Figure 6.2: XRD measurement of SAO thin films. (a) XRD 2θ-ω scan of the SAO films with different thickness. RSM recorded around (103) plane of 30 nm thick SAO (b) and 100 nm SAO (c).

We then performed XRD measurements to investigate the crystal structural information of the SAO layer. The 2θ-ω scan displayed in Figure 6.2a reveals that the SAO is coherently grown on the STO (001) substrate which adopts the (*00l*) orientation and is free from any secondary phase. Upon the thickness variation, two kinds of SAO thin film growth can be identified as the (*00l*) peak locations are different. To better elucidate the different growths, we further studied the lattice parameters of the SAO film by conducting the RSM measurements around (103) plane of the thin films. As can be seen from Figure 6.2b and 6.2c, the SAO film is fully strained on STO at the thickness of 30 nm while relaxation growth occurred at the thickness of 100 nm. The derived lattice constants for SAO (30 nm) are *c* =

0.4288 nm and a = 0.3905 nm, while for SAO (100 nm) are $a = c$ = 0.3956 nm which are very close to the bulk lattice constant values of SAO $a = c$ = 0.3961 nm. Therefore, we can conclude that SAO thin film is fully strained on the substrate when grown at a relatively thin thickness but undergoes a relaxing process with the increased thickness. Note that for the growth of other functional oxides overlayers, we always used the SAO (30 nm) as the buffer layer.

6.2.2 Water etching of bare $Sr_3Al_2O_6$

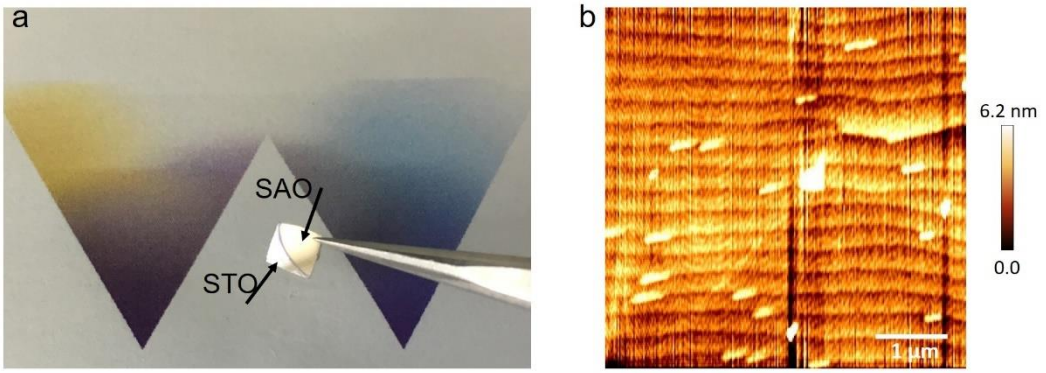

Figure 6.3: The etching of bare SAO film. (a) Optical image after water etching of SAO thin film. (b) AFM topography of the STO after removing the SAO layer.

After obtaining the epitaxial SAO thin film on STO, we next demonstrate the water etching behaviour of this material. When putting the bare SAO (30 nm)/STO sample into the DI-water at room temperature, an extensive dissolution of the SAO film occurred upon its contact with the water. As can be seen from Figure 6.3a, a clear boundary dividing the water-etched and original SAO parts can be seen from the obvious colour contrast. We then examined the topography of the STO substrate after the SAO was removed as displayed in Figure 6.3b. The STO substrate is still of a flat surface which indicates that the growth and water etching processes of SAO film did not cause damage to the substrate. Note that the white dots on the STO substrate shown in the AFM image may be due to the residue of SAO or the poor cleaning process. Moreover, we tried to grow thin films on repeatedly used STO substrates, i.e., STO substrates after growth and etching away the thin

film/SAO heterostructures, the grown structure was still of high single-crystalline quality (data not shown). Note that a careful cleaning process is needed for preparing the STO substrate for the next thin film growth process. Therefore, the possibility of preserving the growth substrates after the developed water etching process could open a door for fabricating oxide nanomembranes while saving the cost of expensive single crystal substrates. Overall, the epitaxial growth of high-quality SAO film on STO and rapid water etching of SAO layer shown here suggest the possibility of using SAO as the sacrificial layer for functional oxide thin film lift-off.

6.2.3 Growth and transfer of functional oxide films

In this section, we discuss the growth of typical functional oxide films, i.e. the heterostructure of ferroelectric BTO and ferromagnetic LSMO on SAO buffered STO substrates, and the following transfer process. We started with a BTO/LSMO heterostructure in which the BTO is relatively thick at 80 nm. The reason to start with the thick BTO film is due to the reason that the modification of the BTO growth parameters using thicker films is easier due to the easy access of XRD and ferroelectric switching tests compared to ultrathin BTO films. The optimised growth parameters can be directly applied to the growth of ultrathin BTO FTJ heterostructures.

The BTO (80 nm)/LSMO (30 nm) heterostructure was grown on SAO (30 nm) buffered STO (001) substrate. The growth parameters can be found in Chapter 3.2.6. To lift off the BTO/LSMO from the substrate, two different transfer methods were adopted here. For the first method, we left the BTO/LSMO/SAO/STO sample without any supporting layer in the DI water for selectively etching of the SAO. After SAO was fully dissolved, the released BTO/LSMO nanomembrane was floated on the water, but broke into pieces of nanomembranes. The picked-up pieces of BTO/LSMO nanomembrane were placed on a new host substrate, i.e. Polyethylene terephthalate (PET) foil as shown in Figure 6.4. The results indicate that the film without any supporting layer tends to be broken due to factors

including environmental vibration, internal strain release, etc. Hence, in order to obtain continuous nanomembranes, supporting layer/film structure was adopted to aid the nanomembrane transfer process. The supporting layer we used was Poly methyl methacrylate (PMMA) which is widely used as the stamp for 2D material transfer and with strong adhesion to the BTO layer.[78, 169]

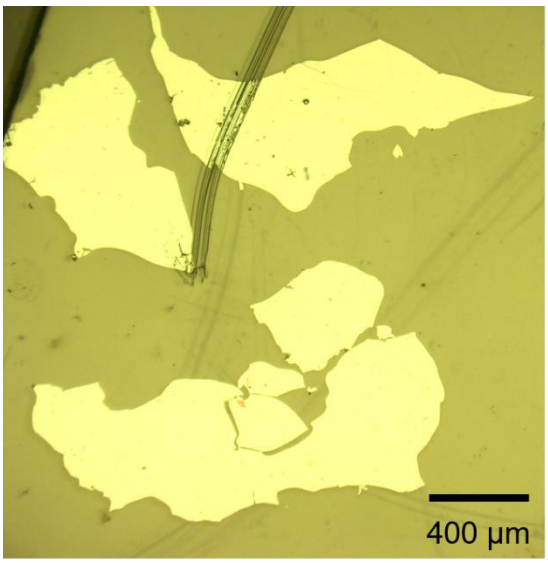

Figure 6.4: Optical image of broken BTO/LSMO nanomembrane pieces on PET substrate.

The key steps of the transfer process are summarised in Figure 6.5a. Unlike the first method, we spin-coated a layer of PMMA on the BTO surface before water etching. The PMMA/sample was then baked at 100 °C for 2 min and next put into the DI water allowing the SAO to be dissolved. Subsequently, the released PMMA/BTO/LSMO nanomembrane was picked up from the water and rinsed in DI-water three times to ensure that the SAO was fully removed. Next, the PMMA/BTO/LSMO nanomembrane was placed onto the new host substrate and baked on a hot plate at 80 °C for several hours to make sure a strong bonding between the nanomembrane and the substrate. Finally, the PMMA layer was removed by acetone to leave the bare BTO/LSMO nanomembrane on the substrate. As can be seen from Figure 6.5b, a lift-off and transfer of complete BTO/LSMO film onto the SiO_2/Si substrate was realised. Note that the irregular shape of the

substrate was intentionally made to check the film completeness during the transfer process. Moreover, beside the BTO/LSMO heterostructure, we also applied the same method on another typical ferroelectric material BFO, the transferred BFO film on PET is shown in Figure 6.5c. Therefore, as inspired by the successful examples of typical ferroelectric and ferromagnetic thin film transfer, we believe

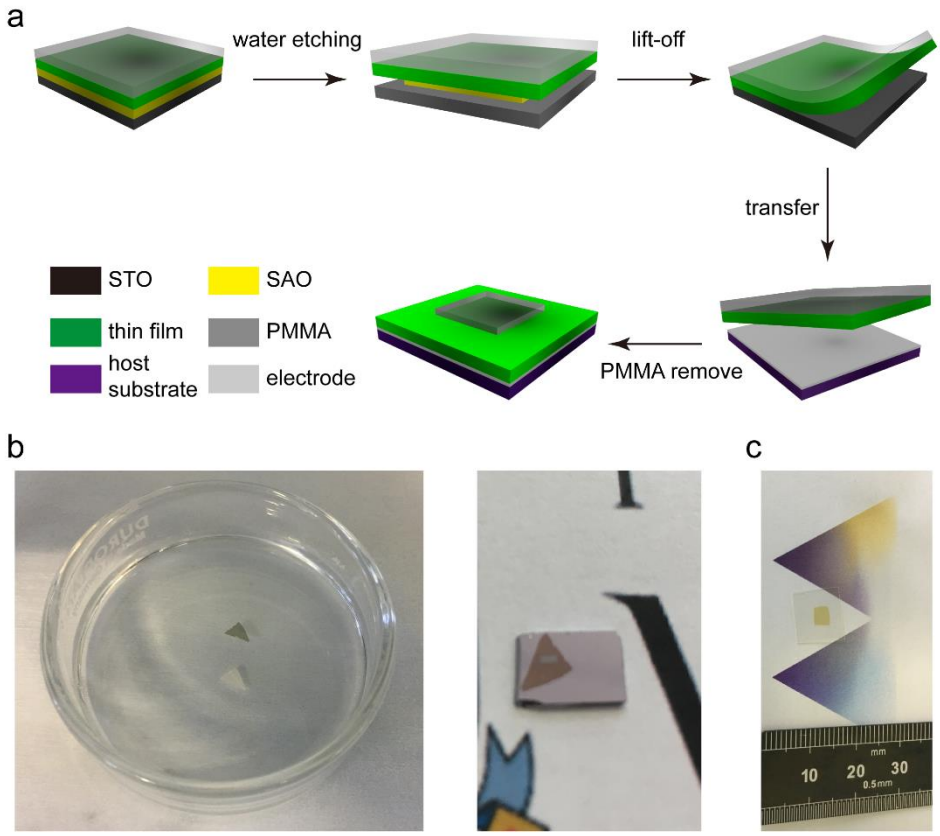

Figure 6.5: Lift-off transfer process with PMMA stamp. (a) Schematic of the key steps involved in the transfer process. Photographs of the transfer of BTO/LSMO (b) and BFO (c) nanomembranes.

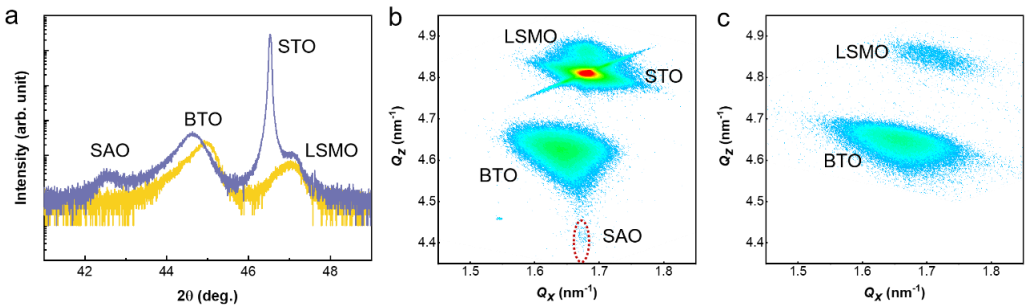

Figure 6.6: Structural information of BTO/LSMO before and after transfer. (a) 2θ-ω scan of the original (purple curve) and transferred (yellow curve) films. RSM around (103) plane of the original (b) and transferred (c) films.

that the selective etching of SAO-based 'grow-transfer' method is of great promise for production of large area single-crystalline nanomembranes out from an even wider range of functional oxide materials.

Next, we collected the structural information of the BTO/LSMO heterostructures before and after transfer process by XRD. As can be seen from Figure 6.6, the BTO/LSMO film preserves the single-crystalline structure after the transfer according to the XRD 2θ-ω scan and reciprocal space map around the (103) plane. The out-of-plane lattice of BTO and LSMO layers both changed after lift-off which can be attributed to the relaxation of the initially strained film after removing the substrate.[170]

After confirming that the 'grow-transfer' method is capable of obtaining single-crystalline oxide nanomembranes. We further checked the functional properties of the ferroelectric and ferromagnetic layers. The ferroelectric switching behaviours of the transferred BTO/LSMO were investigated by ferroelectric hysteresis loop. As can be seen from Figure 6.7a, the transferred BTO nanomembrane demonstrated the ferroelectric switching behaviours which are similar to those of as-grown films. The ferromagnetic hysteresis loop of LSMO was recorded at 10 K using the SQUID as shown in Figure 6.7b, which suggests that there was no degradation of ferromagnetic properties of the LSMO during the transfer process.

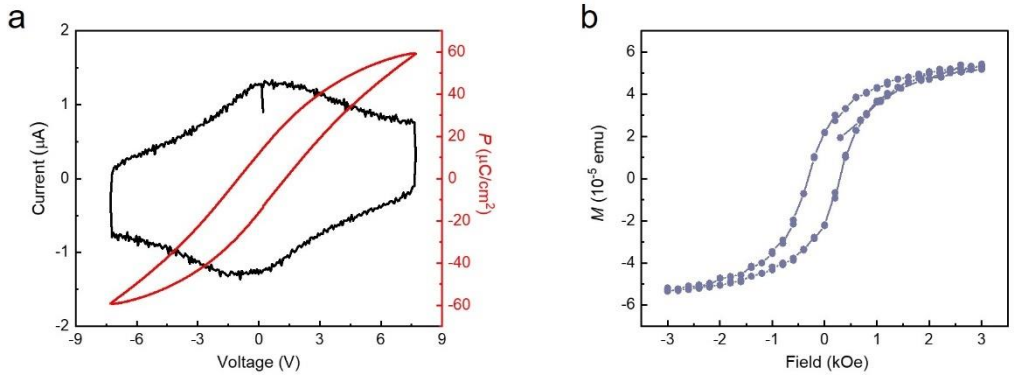

Figure 6.7: Ferroelectric (a) and ferromagnetic (b) hysteresis loops of the transferred BTO/LSMO heterostructure.

Overall, through investigating the structural and functional properties of the transferred BTO/LSMO nanomembranes, we can conclude that the 'growth-transfer' method works well for the perovskite oxide structures, and therefore high-quality ultrathin BTO nanomembranes for ferroelectric tunnel memristors are expected to be obtained in this way.

6.3 Flexible ferroelectric tunnel memristors

6.3.1 Fabrication

As discussed in the previous section, single-crystalline BTO/LSMO nanomembranes can be obtained by 'grow-transfer' method while preserving their functional properties. Using this approach, we successfully fabricated highly flexible ferroelectric tunnel memristors by transferring BTO (3.6 nm)/LSMO (40 nm) nanomembranes on Pt-coated PET substrates. As can be seen from Figure 6.8a, centimetre-scale BTO/LSMO film was completely transferred onto the PET foil from the STO substrate and the resultant device is highly flexible and bendable. Additionally, we have also transferred BTO/LSMO nanomembranes onto Si substrates using the same method in order to carry out the STEM measurements (see Figure 6.8b). 10 μm × 10 μm Pt top electrodes were deposited on the BTO/LSMO membranes to form these ferroelectric tunnel memristors as shown in

Figure 6.8c. Ultrathin metal tips were adopted for the electric measurements as shown in Figure 6.8d.

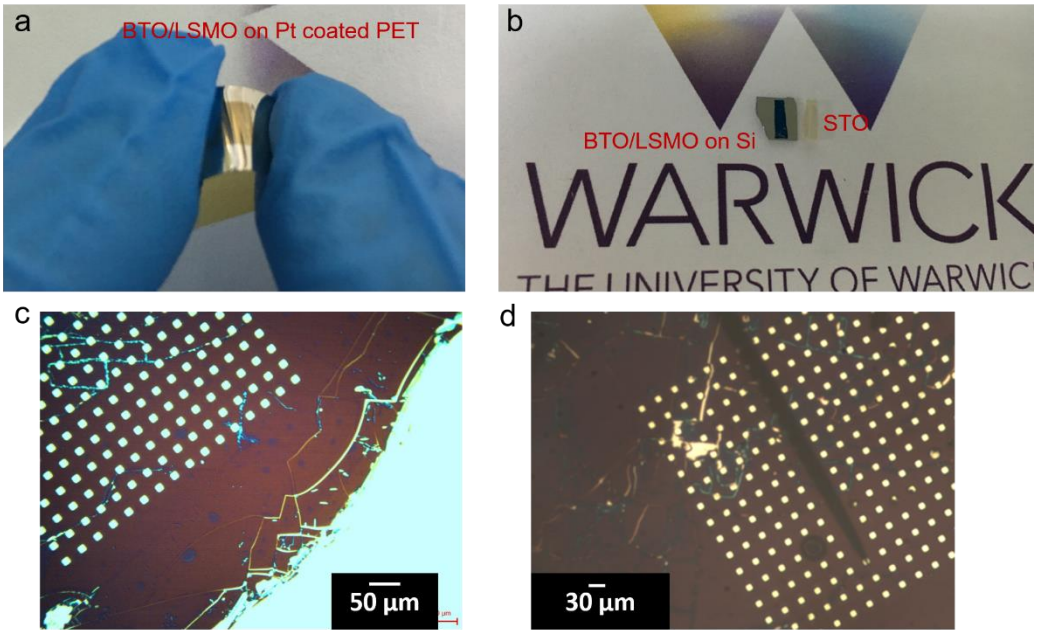

Figure 6.8: Optical images of the flexible ferroelectric tunnel memristors. (a) Flexible ferroelectric tunnel memristor. (b) Transferred BTO/LSMO membrane on Si substrate. Images showing the 10 µm × 10 µm Pt top electrodes deposited on the BTO/LSMO membranes (c) and the ultrathin tip (d) for electric measurements.

6.3.2 Structural investigation

To check the single crystallinity of the transferred BTO/LSMO nanomembranes, we conducted HR-XRD measurements. It is worth noting, in order to obtain significant XRD signal, we used BTO thin film in thickness of 6 nm for measurements, however, the BTO diffraction signal is still too weak to be recorded in the (103) peak reciprocal space mapping. As shown in Figure 6.9a, the 2θ-ω XRD scan clearly indicates the single phase and epitaxial (00l) orientation of the BTO/LSMO heterostructure after transfer. The right panel in Figure 6.9a shows the magnified (002) Bragg peaks of the transferred BTO/LSMO nanomembrane. The epitaxial quality of the transferred membranes was examined by phi-scan around the (103) diffraction of the LSMO. As shown in Figure 6.9b, the sharp peaks with

fourfold symmetry in the phi-scan pattern suggest that the transferred membrane retains the intact single-crystalline structure after the transfer process. Rocking curves of the LSMO at (002) peak before and after transfer were collected as shown in Figure 6.9c. The full width at half maximum (FWHM) of (002) peaks are of similar values which indicate that the transferred membranes are still with high epitaxial quality. In Figure 6.9d, we compare the out-of-plane lattice constants of transferred BTO (80nm) and BTO (6 nm) layers. Surprisingly, for thin BTO nanomembranes, the BTO layer is still compressively strained with the prolonged *c* lattice constant of 4.14 Å. However, the BTO (80nm) layer is fully relaxed with the *c* lattice constant close to the bulk lattice value, i.e. 4.036 Å. In addition, the LSMO layer preserves its original crystal structures with only a slight change of lattice parameters after lifting-off.

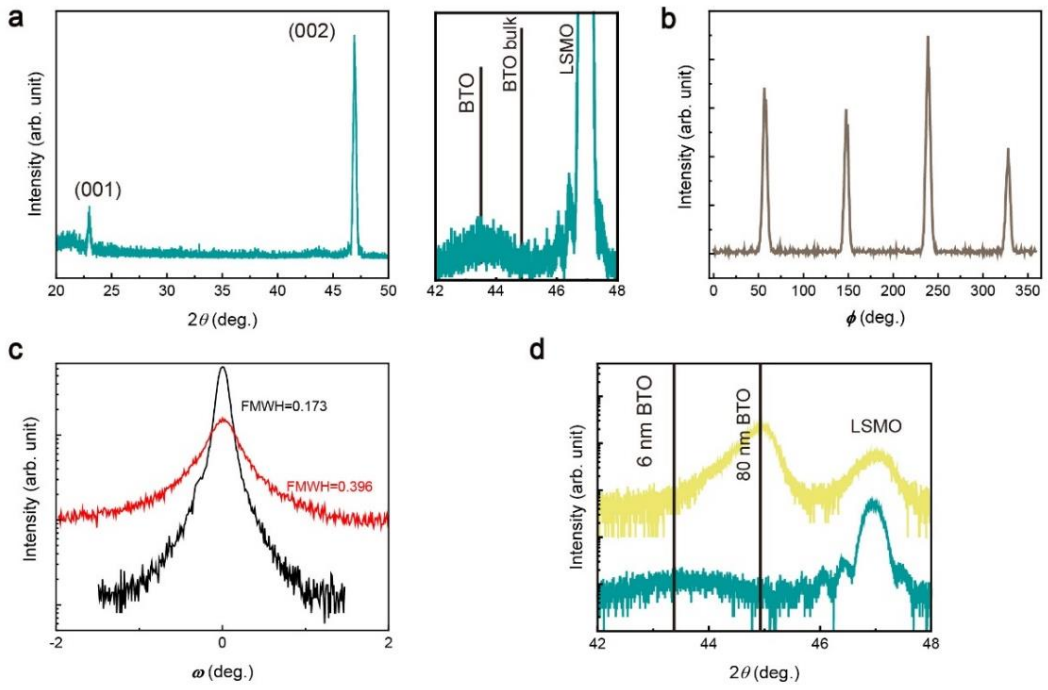

Figure 6.9: XRD measurements of transferred BTO/LSMO nanomembranes. (a) 2θ-ω scan of BTO (6nm)/LSMO (30nm). (b) Phi-scan of LSMO (103). (c) rocking curve scans of LSMO (002) before (black curve) and after (red curve) transfer. (d) Comparison of *c* lattice constants of 6 nm BTO and 80 nm BTO nanomembranes.

To further check the strain state and atomic-scale structural coherency of transferred BTO/LSMO heterostructures, we performed STEM imaging along [001] crystallographic direction using the ADF mode. The transferred BTO/LSMO heterostructure on SiO_2/Si substrate can be clearly identified as shown in Figure 6.10a, the coherent structure indicates that the transferred BTO/LSMO membrane is free from any intermixing or defect formation during the entire fabrication process. The higher magnification ADF-STEM image on the right panel of Figure 6.10, further demonstrates the near-atomically sharp interface in the transferred BTO/LSMO heterostructures. In ultrathin ferroelectric films, the misfit strain imposed by the single crystal substrates is believed to be a key ingredient in stabilizing the ferroelectricity.[16, 93] Whether the strain state or stable ferroelectricity can be maintained in freestanding ultrathin ferroelectric single-crystalline nanomembranes remains an open question and is crucial for the implementation of ultrathin ferroelectrics based flexible electronic devices. To check the strain state, we extracted the *c* and *a* lattice constants of the transferred epitaxial BTO/LSMO heterostructure from the ADF-STEM image, which are well matched with the XRD results. The calculated *c*/*a* ratios (tetragonality) of the as-grown and transferred BTO layer are shown in Figure 6.10b, respectively. We found that the tetragonality of the transferred BTO layer is slightly lower than that of its as-grown state but still remains a high value of ~1.05 in average compared to that of the bulk BTO (*c/a* = 1.01). In comparison, thicker BTO (80 nm) layer with the LSMO buffer layer after transfer undergoes a rapid strain relaxing and is of bulk-like lattice parameters (see Figure 6.9d). After the epitaxial lift-off process, although the freestanding membranes tend to be relieved from the strain state imposed by the growth substrate,[171] if the film is attached to a buffer layer (LSMO here), the strain relaxation could be greatly suppressed with decreasing the film thickness, being coherent to the buffer layer underneath.[16, 172] This is confirmed by the relationship between the lattice parameters and the thickness of the transferred BTO layer as demonstrated here. Therefore, we can conclude that the high tetragonality of the transferred BTO nanomembrane is related to its ultrathin nature which could

maintain the strain imposed by the LSMO buffer layer. We note that this high tetragonality in the transferred BTO layer (~1.05) is even comparable to that of ultrathin BTO films grown directly on single crystal substrate, for example, *c/a* = 1.051 for BTO grown on LSMO buffered $NdGaO_3$ substrate.[16]

Overall, the presented results unambiguously demonstrate that the single-crystalline structure of the BTO/LSMO nanomembranes is well preserved after the epitaxial lift-off process. Moreover, in the BTO/LSMO nanomembranes, the strain state of the BTO layer imposed by the LSMO buffer layer is similar to that of a thin film imposed by the growth substrate[16, 172] which hints that ferroelectricity could persist in the freestanding heterostructures.

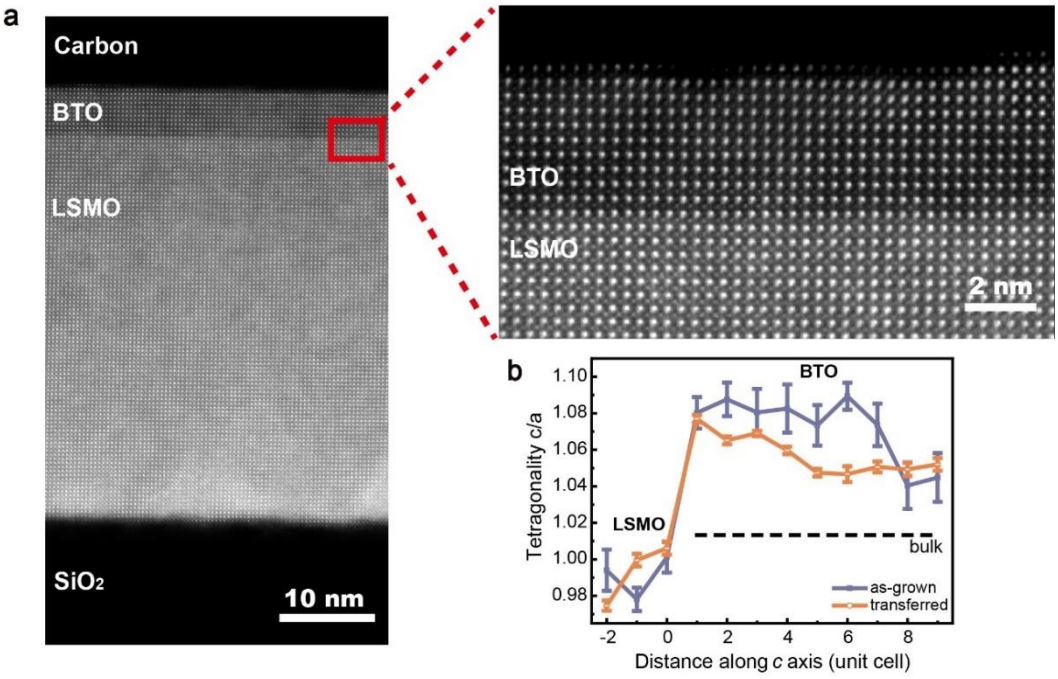

Figure 6.10: STEM analysis of BTO/LSMO nanomembrane. (a) ADF-STEM image of the transferred BTO/LSMO stack on SiO_2/Si substrate and the interface region with atomic resolution (the right panel). (b) The distribution of BTO tetragonality as a function of distance from the LSMO/BTO interface (left in the plot) to the BTO surface (right) before and after transfer process. The dashed line indicates the tetragonality value of bulk BTO crystal.

6.4 Electric characterisation of flexible ferroelectric tunnel memristor

6.4.1 Ferroelectricity and tunnelling electroresistance

After the confirmation of the epitaxial structure of the transferred single-crystalline oxide nanomembranes, we now investigated the most important functional properties, i.e. ferroelectricity, of the BTO/LSMO nanomembranes by piezoresponse force microscopy (PFM). Note that the PFM characterisations were performed using Dual AC™ Resonance Tracking piezoresponse force microscopy (MFP-3D, Asylum Research) and conductive NSC14/Pt cantilevers were used. PFM hysteresis loops were recorded at off-field model. As can be seen from Figure 6.11b and 6.11c, the electrically writing of oppositely polarised ferroelectric domains and the clear hysteretic behaviour of out-of-plane piezoresponse signal in phase and amplitude acquired as a function of the dc voltage unambiguously illustrate the ferroelectric nature for the BTO layer integrated in the flexible junction devices. As indicated by the amplitude loop, the local coercive voltages of the BTO layer are +2 V and -3 V, respectively. The written antiparallel polarized ferroelectric domain patterns shown by the PFM phase image remains stable after several hours (data not shown). Moreover, we found that a bare 5 nm thick BTO nanomembrane without the LSMO buffer layer did not show any ferroelectricity through PFM probe (data not shown). As mentioned before, the strain state in the bare BTO layer is released after the lift-off which thus results in a low *c/a* ratio of the BTO. This result in turn establishes the importance of high tetragonality in enhancing the ferroelectricity in ultrathin ferroelectric films.

The resistive switching of the resulting Pt/BTO/LSMO flexible FTJs was then investigated by measuring the device current-voltage (*I-V)* characteristics upon BTO polarisation switching. Figure 6.11d shows the *I-V* curves of a fabricated Pt/BTO/LSMO junction after applying 100 μs long voltage pulses with amplitudes of +3 V and -4 V, respectively. Those results indicate an OFF/ON ratio of 5 or 500%

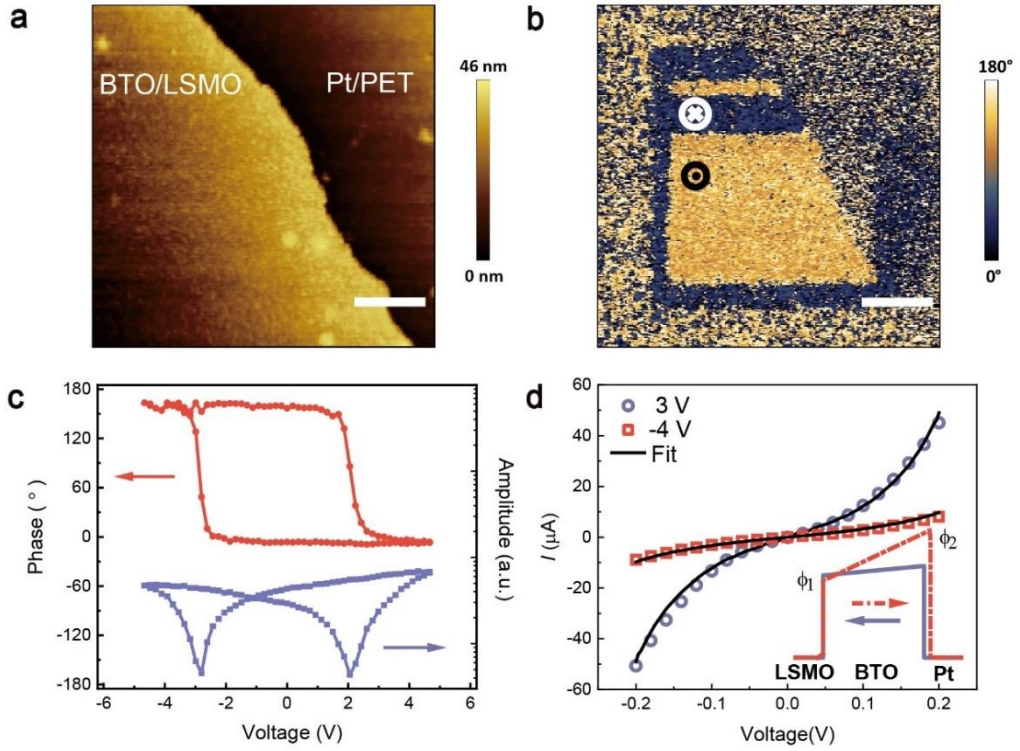

Figure 6.11: Ferroelectricity characterizations of the BTO/LSMO nanomembranes. (a) The topography of BTO/LSMO on metal-coated PET. (b) PFM image of the same area with electrically written ferroelectric domains, the writing voltages are 4 V and -4 V, respectively. Scale bars for (a) and (b): 1 μm. (c) Hysteresis dependence of the PFM phase and amplitude. (d) The *IV* curves of the FTJ at different polarisation states. The inset sketches the barrier for the metal/BTO/LSMO tunnel junction at different states.

change of TER in our flexible FTJ. To model the transport properties in the BTO/LSMO nanomembranes, we fitted the *I-V* curves of the FTJ using the Brinkman model for tunnel transport across trapezoidal potential barriers in the Wentzel–Kramers–Brillouin (WKB) approximation.[20] The current density can be expressed as:

$$J = \mathrm{C}\frac{\exp\left\{\alpha(V)\left[\left(\emptyset_2-\frac{eV}{2}\right)^{\frac{3}{2}}-\left(\emptyset_1-\frac{eV}{2}\right)^{\frac{3}{2}}\right]\right\}}{\alpha^2(V)\left[\left(\emptyset_2-\frac{eV}{2}\right)^{\frac{1}{2}}-\left(\emptyset_1+\frac{eV}{2}\right)^{\frac{1}{2}}\right]^2} \times \sinh\left\{\frac{3}{2}\alpha(V)\left[\left(\emptyset_2-\frac{eV}{2}\right)^{\frac{1}{2}}-\left(\emptyset_1+\frac{eV}{2}\right)^{\frac{1}{2}}\right]\frac{eV}{2}\right\} \quad (6\text{-}1)$$

here $\mathrm{C} = -(4em)/(9\pi^2\hbar^3)$ and $\alpha(V) = [4\mathrm{d}(2m)^{\frac{1}{2}}]/[3\hbar(\emptyset_1 + eV - \emptyset_2)]$. The device area is 100 μm^2 with the BTO barrier width d = 3.6 nm. The potential barrier heights at the LSMO/BTO ($\emptyset_2$) and BTO/Pt interfaces ($\emptyset_1$) and the effective tunnelling electron mass (m) are adjusted during the fitting process. The obtained parameters are $\emptyset_1$ = 0.2413 (0.1996), $\emptyset_2$ = 0.4166 (0.9787) and m = 0.4866 (0.2874) for the low resistance state (high resistance state). A sketch of the barrier shapes using the obtained fitting results at different BTO ferroelectric polarisation states is shown in the inset of Figure 6.11d. Indeed, the potential barrier heights changes upon the BTO ferroelectric polarisation reversal which thus leads to the TER.

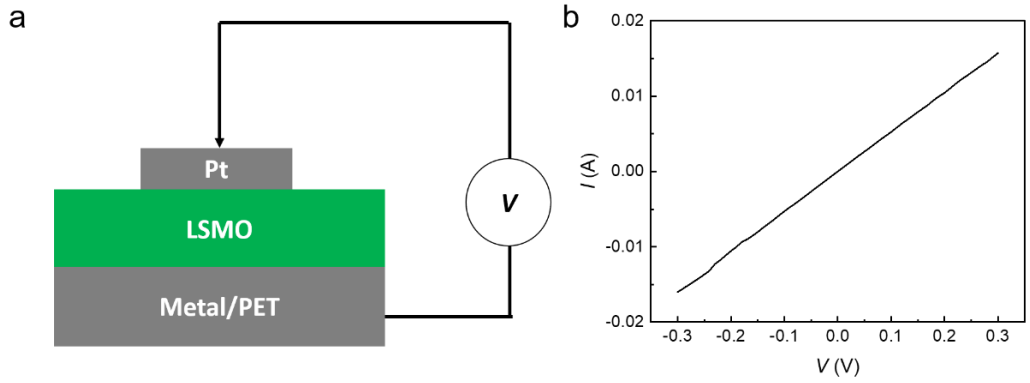

Figure 6.12: Electrical measurement of a LSMO junction. (a) Setup of the transport measurement of Pt/LSMO/Pt junction. (b) The *I*-*V* curve of a Pt/LSMO/Pt junction on PET substrate.

As reported before, LSMO junctions in some conditions such as rich of oxygen vacancies, can also exhibit memristive behaviours.[173] To eliminate the possibility of the LSMO dominated transport characteristics, we conducted reference

experiments using a transferred LSMO nanomembrane. By conducting the *I-V* tests of a Pt/LSMO/Pt junction, no TER effect in LSMO nanomembrane can be observed, in contrast the whole junction shows good conducting properties (see Figure 6.12b). Therefore, it is confirmed that the ferroelectric BTO layer plays the sole role corresponding to the observed resistive switching effect. Overall, the results shown here clearly indicate the ferroelectric character retained in the transferred epitaxial BTO layer and the ferroelectric polarisation dependent tunnelling transport nature of the flexible FTJ devices.

6.4.2 Memristive properties of the flexible devices

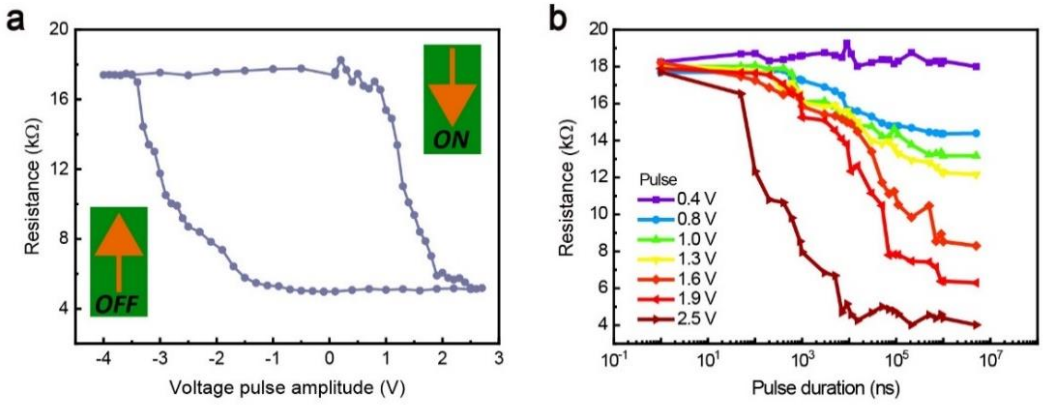

Figure 6.13: Memristive properties of the flexible BTO/LSMO ferroelectric tunnel memristors. (a) The hysteretic resistance as a function of operating voltage pulses reading at 200 mV. (b) The evolution of the memristor resistance states as a function of pulse duration and amplitude.

In the following, we present the device properties of the prototype flexible ferroelectric tunnel memristors. Figure 6.13a shows the plot of the device resistance as a function of the voltage pulse amplitude while fixing the pulse duration at 10 μs. A hysteretic resistance cycle with large OFF/ON ratio ~500% is observed, which demonstrates the junction resistance as a history of the applied voltages pulses, i.e. memristive behaviours[174]. Note that the resistance of the flexible memristors in the following experiments was recorded at 0.2 V. The observed

multi-level resistance states of the flexible FTJ can be attributed to the ferroelectric domain reconfiguration in the BTO ferroelectric barrier during applying the voltage pulses, i.e., the expansion of these existing downward or upward-polarized ferroelectric domains as well as the nucleation of new domains.[5, 128, 134] A detailed explanation of the domain reconfiguration controlled resistance evolution can be found in Chapter 4. Here, starting from the uniform upward ferroelectric polarisation state in the BTO layer (after applying -4 V voltage pulse), we gradually increased the ratio of downward/upward polarisation domains from 0 to 100% (uniform downward polarisation, ON state) by applying a set of positive voltage pulses. The reversed process, i.e., from OFF to ON resistance state, was also carried out by applying negative voltage pulses. The deterministic electric control of the multiple resistance states in one single junction indicates that our flexible FTJs are capable of multilevel data storage and can be exploited for flexible high density memories.[33] Next, we show that the resistance of the flexible memristors can be tuned by the voltage pulse number, amplitude and duration. A detailed modulation of the junction resistance by voltage pulse duration and amplitude is depicted in Figure 6.13b. The device is switched from the high resistance state towards low resistance state by applying voltage pulses of different amplitude and duration. Clearly, a wide range of intermediate resistance states in our flexible memristor can be obtained through control of the shape of the applied voltage pulses.

Figure 6.14 shows the junction resistance evolution from low resistance state to high resistance state upon applying consecutive pulses varying amplitude. To obtain the results in Figure 6.14, we used a series of negative SET voltage pulses with fixed duration of 500 ns and the ReSET voltage pulses of 3 V, 100 μs to tune the junction resistance. The final resistance states of the flexible memristor are dependent on the number of the SET voltage pulses applied which correspond to the so-called cumulative effect.[175]

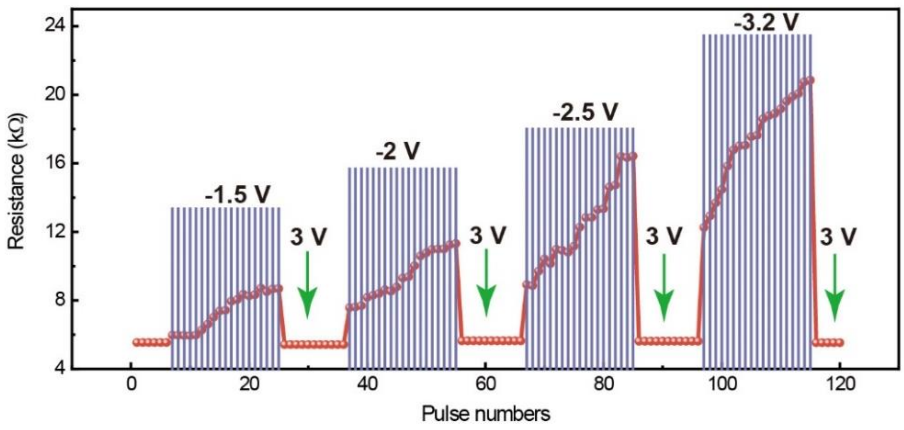

Figure 6.14: Response of the device resistance state to multiple 0.5 µs long SET voltage pulses followed by the 3V ReSET pulses.

Overall, through studying the dynamic response of the flexible device upon applying a sequences of voltage pulse stressing with different amplitudes and durations (matching the real working environment), we have demonstrated that our flexible BTO/LSMO nanomembranes are of superior memristive properties. Moreover, those demonstrated characteristics especially the cumulative effect indicate that the presented flexible memristors can be used as artificial synapses in which the synaptic transmission can be modified through spike-timing-dependent plasticity, thus are appealing for future flexible and portable neural computing applications.[128, 176, 177]

6.4.3 Reliability tests

For practical applications of the flexible memories, the device reliability is crucial. We thus carried out bending and retention tests to investigate the mechanical flexing performance and time stability of the PET substrates hosted BTO/LSMO ferroelectric tunnel memristors, respectively. The bending tests with 1.5 mm curvature of those flexible devices were carried out up to 100 cycles, which shows no sizable degradation of the functional properties, see Figure 6.15a. Furthermore, the devices present stable resistance state for several hours at respective OFF, intermediate and ON states as shown in Figure 6.15b, which indicate excellent

retention characteristics as non-volatile memories. Note that in order to prevent the sliding of the nanomembrane on the PET substrate, we spin coated a thin layer of photoresist on the device. The photoresist layer also serves as the insulating hard mask allowing the conducting wire attaching. For electric measurements, the top electrode of the device was contacted by the conducting Cu wire rather than the sharp contact needle which might induce external pressure on the flexible nanomembrane. The detailed configuration can be found in Figure 6.15c.

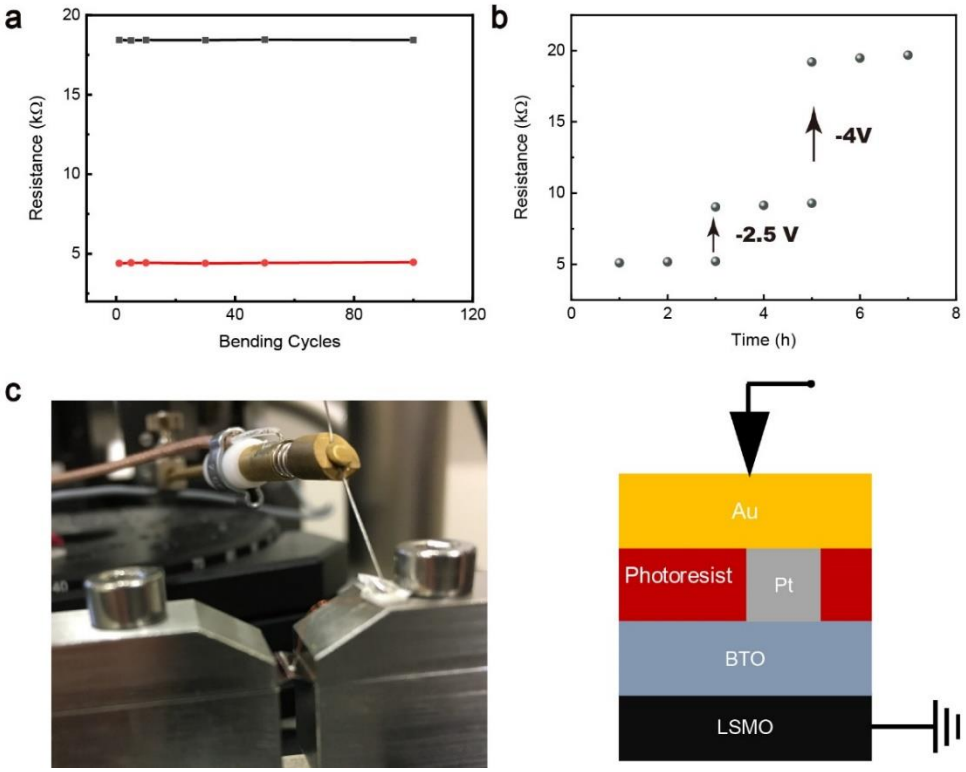

Figure 6.15: Reliability of the flexible memristor. (a) The bending test up to 100 cycles of the device at high and low resistance states, respectively. (b) The retention time of the device at three different resistance states. (c) The configuration of the measurement setup and the sample connection.

6.5 Summary

In summary, we studied the water-soluble SAO buffer layer based 'grow-transfer' method for obtaining large scale single-crystalline oxide nanomembranes. Typical

functional oxide materials like BTO, BFO and LSMO thin films have been shown to be successfully transferred on arbitrary foreign substrates, e.g. Si and PET. Those results present a practical and generic approach to integrate functional oxide films on arbitrary surfaces, which suggests exciting opportunities for future large area, affordable and flexible substrate hosted oxide nanomembrane devices with multifunctional characteristics. We further demonstrated that ultrathin epitaxial BTO layer along with the LSMO buffer can be lifted off and transferred onto flexible plastic substrates while retaining the robust ferroelectricity. The ferroelectric polarisation dependent resistive switching in plastic substrate hosted BTO/LSMO FTJ memristors was studied and illustrated predictive functionalities required for implementation of the flexible and portable high-density memories and neuromorphic architectures.

Chapter 7

Summary and outlook

In the final Chapter, main results of the performed experiments are briefly summarised and some perspectives on the future development of ferroelectric tunnel junctions (FTJs) or systems with ultrathin ferroelectric layers are given.

In the first block of this Thesis, we provided experimental evidence of the bi-ferroic or magneto-electric memristive properties, i.e., multilevel electric control of both tunnelling magnetoresistance (TMR) and tunnelling electroresistance (TER), in Co/$PbTiO_3$(PTO)/$La_{0.3}Sr_{0.7}MnO_3$(LSMO) multiferroic tunnel junctions (MFTJ). Through electrically modulating the ratio between up- and down-polarised ferroelectric domains, a broad range of both TMR and TER values have been found to be continuously written solely by applying electric voltages. The results along with the developed theory demonstrate that the multi-state ferroelectric domain configuration of the MFTJ not only contributes to the electronic memristive switching, but also results in continuous interface spin polarisation thus TMR variations. Therefore, we found that the MFTJs can be operated as both magnetic and ferroelectric tunnel memristors.

Further on, we studied an optoelectronic memory using a hybrid device design which combines the FTJs with a ferroelectric photovoltaic cell. In particular, the system is based on the combination of the nanoscale contact, e.g., atomic force microscopy (AFM) with a bulk photovoltaic (BPV) cell ($BiFeO_3$ thin film). Using the tip-enhanced photovoltaic effect, we show that through the nanosized contact, a light-generated, intensity-adjustable and polarity-switchable electric field can be used for nanoscopic writing of the resistance states in FTJs. Moreover, considering the efficiency of the method, we show that the light-controllable writing process is comparable to the programmable voltage source in terms of the reversibility and multiple-strength of the electric field applied on the electronic components.

In the final block, we demonstrated that 3.6 nm thick single-crystalline ferroelectric

$BaTiO_3$ (BTO) nanomembranes up to centimetre scale have been successfully transferred from the $SrTiO_3$ growth substrates onto flexible PET plastic substrates through a process involving wet-etching the water-soluble sacrificial epitaxial layer. Against all the predictions, we unambiguously show that the obtained freestanding ultrathin BTO layers can still retain the stable ferroelectric polarisation at room temperature due to the preservation of the compressively strained single-crystalline structure after transfer. We subsequently fabricated FTJ devices using the BTO nanomembranes mounted on plastic substrates, which exhibit excellent memristive properties with resistance switching ratio exceeding 500% and are highly mechanically flexible.

Overall, throughout this Thesis, we have explored the interplay between ferroelectricity and ferromagnetism in MFTJs and its manipulation using ferroelectric domain configuration. We also studied the light-controlled electric writing of polarisation states in ferroelectrics. Finally, novel flexible electronic devices based on ultrathin ferroelectric nanomembranes are obtained using the grow-transfer method.

Although a qualitive model involving the domain reconfiguration in the MFTJ is proposed here to elucidate the observed memristive TMR and TER behaviours, a more precise theory relating the domain switching with the TMR/TER evolution will need to be established. Once with the well-established and predictive mechanism, the MFTJ could further be developed to magnetic- and electric-field responsive neuromorphic computing hardware. As for the optic writing, although the main focus was with FTJs in this work, we note that in principle any non-photoactive electronic materials can be integrated with the BPV cell. Through proper device design, light-controlled two-terminal resistive switching junctions and three-terminal transistors can both be realised. Based on this prototype proposal, advanced applications such as light sensor and light information storage can be further developed. Regarding the flexible FTJs, an unexplored subject would be the impact of external mechanical strain on the FTJ performance. However, this will

require a better device design considering the obvious difficulty of applying sufficient stress on such a small working FTJ device (~10 μm size) by flexing the large plastic substrate, which is with four orders of magnitude larger dimension than that of an FTJ. Last, as epitaxial complex oxide heterostructures are a huge playground for novel phenomena and functionalities, the epitaxial ferroelectric nanomembranes can further be employed to explore more complex properties by means like tuning the lattice, combination with other functional oxide layers, etc. An example would be tuning the exchange bias in freestanding BFO/LSMO nanomembranes through external stress.

Bibliography

1. Scott, J. F. *Ferroelectrics* **2016,** 503, (1), 117-132.
2. Scott, J. F.; De Araujo, C. A. P. *Science* **1989,** 246, (4936), 1400-1405.
3. Garcia, V.; Bibes, M. *Nature Communications* **2014,** 5, 4289.
4. Bruno, F. Y.; Boyn, S.; Fusil, S.; Girod, S.; Carrétéro, C.; Marinova, M.; Gloter, A.; Xavier, S.; Deranlot, C.; Bibes, M. *Advanced Electronic Materials* **2016,** 2, (3), 1500245.
5. Chanthbouala, A.; Garcia, V.; Cherifi, R. O.; Bouzehouane, K.; Fusil, S.; Moya, X.; Xavier, S.; Yamada, H.; Deranlot, C.; Mathur, N. D.; Bibes, M.; Barthelemy, A.; Grollier, J. *Nature Materials* **2012,** 11, (10), 860-864.
6. Garcia, V.; Bibes, M.; Bocher, L.; Valencia, S.; Kronast, F.; Crassous, A.; Moya, X.; Enouz-Vedrenne, S.; Gloter, A.; Imhoff, D.; Deranlot, C.; Mathur, N. D.; Fusil, S.; Bouzehouane, K.; Barthelemy, A. *Science* **2010,** 327, (5969), 1106-1110.
7. Lines, M. E.; Glass, A. M., *Principles and applications of ferroelectrics and related materials*. Oxford university press: 1977.
8. Wang, Y.; Chen, W.; Wang, B.; Zheng, Y. *Materials* **2014,** 7, (9), 6377-6485.
9. Ahn, C. H.; Rabe, K. M.; Triscone, J. M. *Science* **2004,** 303, (5657), 488-491.
10. Schlom, D. G.; Chen, L.-Q.; Fennie, C. J.; Gopalan, V.; Muller, D. A.; Pan, X.; Ramesh, R.; Uecker, R. *MRS Bulletin* **2014,** 39, (2), 118-130.
11. Spaldin, N. A. *Science* **2004,** 304, (5677), 1606-1607.
12. Dawber, M.; Chandra, P.; Littlewood, P. B.; Scott, J. F. *Journal of Physics: Condensed Matter* **2003,** 15, (24), L393.
13. Setter, N.; Damjanovic, D.; Eng, L.; Fox, G.; Gevorgian, S.; Hong, S.; Kingon, A.; Kohlstedt, H.; Park, N. Y.; Stephenson, G. B.; Stolitchnov, I.; Taganstev, A. K.; Taylor, D. V.; Yamada, T.; Streiffer, S. *Journal of Applied Physics* **2006,** 100, (5), 051606.
14. Fong, D. D.; Stephenson, G. B.; Streiffer, S. K.; Eastman, J. A.; Auciello, O.; Fuoss, P. H.; Thompson, C. *Science* **2004,** 304, (5677), 1650-1653.
15. Wang, J.; Wylie-van Eerd, B.; Sluka, T.; Sandu, C.; Cantoni, M.; Wei, X. K.; Kvasov, A.; McGilly, L. J.; Gemeiner, P.; Dkhil, B.; Tagantsev, A.; Trodahl, J.; Setter, N. *Nature Materials* **2015,** 14, (10), 985-90.
16. Garcia, V.; Fusil, S.; Bouzehouane, K.; Enouz-Vedrenne, S.; Mathur, N. D.; Barthelemy, A.; Bibes, M. *Nature* **2009,** 460, (7251), 81-84.
17. Brinkman, W. F.; Dynes, R. C.; Rowell, J. M. *Journal of Applied Physics* **1970,** 41, (5), 1915-1921.
18. Pantel, D.; Alexe, M. *Physical Review B* **2010,** 82, (13), 134105.

19. Zhuravlev, M. Y.; Sabirianov, R. F.; Jaswal, S. S.; Tsymbal, E. Y. *Physical Review Letters* **2005,** 94, (24), 246902.
20. Gruverman, A.; Wu, D.; Lu, H.; Wang, Y.; Jang, H.; Folkman, C.; Zhuravlev, M. Y.; Felker, D.; Rzchowski, M.; Eom, C.-B. *Nano Letters* **2009,** 9, (10), 3539-3543.
21. Fowler, R. H.; Nordheim, L. *Proceedings of the Royal Society of London. Series A, Containing Papers of a Mathematical and Physical Character* **1928,** 119, (781), 173-181.
22. Esaki, a. L.; Laibowitz, R. B.; Stiles, P. J. *IBM Tech. Discl. Bull* **1971,** 13, (2161), 114.
23. Tsymbal, E. Y.; Kohlstedt, H. *Science* **2006,** 313, (5784), 181-183.
24. Preziosi, D.; Alexe, M.; Hesse, D.; Salluzzo, M. *Physical Review Letters* **2015,** 115, (15), 157401.
25. Bilc, D. I.; Novaes, F. D.; Íñiguez, J.; Ordejón, P.; Ghosez, P. *ACS Nano* **2012,** 6, (2), 1473-1478.
26. Velev, J.; Duan, C.-G.; Belashchenko, K.; Jaswal, S.; Tsymbal, E. *Physical Review Letters* **2007,** 98, (13), 137201.
27. Kohlstedt, H.; Pertsev, N.; Rodríguez Contreras, J.; Waser, R. *Physical Review B* **2005,** 72, (12), 125341.
28. Luo, X.; Wang, B.; Zheng, Y. *ACS Nano* **2011,** 5, (3), 1649-1656.
29. Chua, L. O. *Circuit Theory, IEEE Transactions on* **1971,** 18, (5), 507-519.
30. Krzysteczko, P.; Munchenberger, J.; Schafers, M.; Reiss, G.; Thomas, A. *Advanced Materials* **2012,** 24, (6), 762-766.
31. Chua, L. *Semiconductor Science and Technology* **2014,** 29, (10), 104001.
32. Shin, Y. H.; Grinberg, I.; Chen, I. W.; Rappe, A. M. *Nature* **2007,** 449, (7164), 881-884.
33. Lee, D.; Yang, S. M.; Kim, T. H.; Jeon, B. C.; Kim, Y. S.; Yoon, J. G.; Lee, H. N.; Baek, S. H.; Eom, C. B.; Noh, T. W. *Advanced Materials* **2012,** 24, (3), 402-406.
34. Moodera, J. S.; Kinder, L. R.; Wong, T. M.; Meservey, R. *Physical Review Letters* **1995,** 74, (16), 3273.
35. Julliere, M. *Physics Letters A* **1975,** 54, (3), 225-226.
36. Scott, J. *Nature Materials* **2007,** 6, (4), 256-257.
37. Ohno, H.; Chiba, D.; Matsukura, F.; Omiya, T.; Abe, E.; Dietl, T.; Ohno, Y.; Ohtani, K. *Nature* **2000,** 408, (6815), 944-946.
38. Matsukura, F.; Tokura, Y.; Ohno, H. *Nature Nanotechnology* **2015,** 10, (3), 209-220.
39. Gajek, M.; Bibes, M.; Fusil, S.; Bouzehouane, K.; Fontcuberta, J.; Barthelemy, A.; Fert, A. *Nature Materials* **2007,** 6, (4), 296-302.

40. Zhuravlev, M. Y.; Jaswal, S. S.; Tsymbal, E. Y.; Sabirianov, R. F. *Applied Physics Letters* **2005,** 87, (22), 222114.
41. Pantel, D.; Goetze, S.; Hesse, D.; Alexe, M. *Nature Materials* **2012,** 11, (4), 289-293.
42. Valencia, S.; Crassous, A.; Bocher, L.; Garcia, V.; Moya, X.; Cherifi, R. O.; Deranlot, C.; Bouzehouane, K.; Fusil, S.; Zobelli, A.; Gloter, A.; Mathur, N. D.; Gaupp, A.; Abrudan, R.; Radu, F.; Barthelemy, A.; Bibes, M. *Nature Materials* **2011,** 10, (10), 753-758.
43. Shah, A.; Torres, P.; Tscharner, R.; Wyrsch, N.; Keppner, H. *Science* **1999,** 285, (5428), 692-698.
44. Peumans, P.; Uchida, S.; Forrest, S. R., Efficient bulk heterojunction photovoltaic cells using small-molecular-weight organic thin films. *Materials for Sustainable Energy: A Collection of Peer-Reviewed Research and Review Articles from Nature Publishing Group*, World Scientific: 2011; 94-98.
45. Yang, S. Y.; Seidel, J.; Byrnes, S. J.; Shafer, P.; Yang, C. H.; Rossell, M. D.; Yu, P.; Chu, Y. H.; Scott, J. F.; Ager, J. W.; Martin, L. W.; Ramesh, R. *Nature Nanotechnology* **2010,** 5, (2), 143-147.
46. Sturman, P. J., *Photovoltaic and Photo-refractive Effects in Noncentrosymmetric Materials*. CRC Press: 1992; Vol. 8.
47. Fridkin, V. M., *Photoferroelectrics*. Springer Science & Business Media: 2012; Vol. 9.
48. Ruppel, W.; Von Baltz, R.; Wurfel, P. *Ferroelectrics* **1982,** 43, (1), 109-123.
49. Bhatnagar, A.; Roy Chaudhuri, A.; Heon Kim, Y.; Hesse, D.; Alexe, M. *Nature Communications* **2013,** 4, 2835.
50. Alexe, M.; Hesse, D. *Nature Communications* **2011,** 2, 256.
51. Spanier, J. E.; Fridkin, V. M.; Rappe, A. M.; Akbashev, A. R.; Polemi, A.; Qi, Y.; Gu, Z.; Young, S. M.; Hawley, C. J.; Imbrenda, D.; Xiao, G.; Bennett-Jackson, A. L.; Johnson, C. L. *Nature Photonics* **2016,** 10, (9), 611-616.
52. Sturman, B.; Podivilov, E. *Physical Review B* **2017,** 96, (13), 134107.
53. Nathan, A.; Ahnood, A.; Cole, M. T.; Sungsik, L.; Suzuki, Y.; Hiralal, P.; Bonaccorso, F.; Hasan, T.; Garcia-Gancedo, L.; Dyadyusha, A.; Haque, S.; Andrew, P.; Hofmann, S.; Moultrie, J.; Daping, C.; Flewitt, A. J.; Ferrari, A. C.; Kelly, M. J.; Robertson, J.; Amaratunga, G. A. J.; Milne, W. I. *Proceedings of the IEEE* **2012,** 100, (Special Centennial Issue), 1486-1517.
54. Sekitani, T.; Zschieschang, U.; Klauk, H.; Someya, T. *Nature Materials* **2010,** 9, (12), 1015.
55. Sekitani, T.; Yokota, T.; Zschieschang, U.; Klauk, H.; Bauer, S.; Takeuchi, K.; Takamiya, M.; Sakurai, T.; Someya, T. *Science* **2009,** 326, (5959), 1516-1519.

56. Ko, H. C.; Stoykovich, M. P.; Song, J.; Malyarchuk, V.; Choi, W. M.; Yu, C. J.; Geddes, J. B., 3rd; Xiao, J.; Wang, S.; Huang, Y.; Rogers, J. A. *Nature* **2008,** 454, (7205), 748-753.
57. Park, C.-J.; Park, H. J.; Lee, J. Y.; Kim, J.; Lee, C.-H.; Joo, J. *ACS Applied Materials & Interfaces* **2018,** 10, (35), 29848-29856.
58. Kim, Y.; Cruz, S. S.; Lee, K.; Alawode, B. O.; Choi, C.; Song, Y.; Johnson, J. M.; Heidelberger, C.; Kong, W.; Choi, S.; Qiao, K.; Almansouri, I.; Fitzgerald, E. A.; Kong, J.; Kolpak, A. M.; Hwang, J.; Kim, J. *Nature* **2017,** 544, (7650), 340-343.
59. Park, S.-E.; Shrout, T. R. *Journal of Applied Physics* **1997,** 82, (4), 1804-1811.
60. Tomita, M.; Murakami, M. *Nature* **2003,** 421, (6922), 517.
61. Ramesh, R. *Nature Materials* **2007,** 6, (1), 21.
62. Baldini, M.; Muramatsu, T.; Sherafati, M.; Mao, H. K.; Malavasi, L.; Postorino, P.; Satpathy, S.; Struzhkin, V. V. *Proceedings of the National Academy of Sciences* **2015,** 112, (35), 10869-10872.
63. Ohtomo, A.; Hwang, H. *Nature* **2004,** 427, (6973), 423.
64. Ma, N.; Zhang, K.; Yang, Y. *Advanced Materials* **2017,** 29, (46), 1703694.
65. Chen, X.; Han, X.; Shen, Q.-D. *Advanced Electronic Materials* **2017,** 3, (5), 1600460.
66. Gruverman, A.; Rodriguez, B. J.; Kingon, A. I.; Nemanich, R. J.; Tagantsev, A. K.; Cross, J. S.; Tsukada, M. *Applied Physics Letters* **2003,** 83, (4), 728-730.
67. Chu, Y.-H. *npj Quantum Materials* **2017,** 2, (1), 67.
68. Hu, W. J.; Juo, D.-M.; You, L.; Wang, J.; Chen, Y.-C.; Chu, Y.-H.; Wu, T. *Scientific Reports* **2014,** 4, 4772.
69. Bakaul, S. R.; Serrao, C. R.; Lee, O.; Lu, Z.; Yadav, A.; Carraro, C.; Maboudian, R.; Ramesh, R.; Salahuddin, S. *Advanced Materials* **2017,** 29, (11), 1605699.
70. Koma, A.; Sunouchi, K.; Miyajima, T. *Microelectronic Engineering* **1984,** 2, (1-3), 129-136.
71. Jariwala, D.; Marks, T. J.; Hersam, M. C. *Nature Materials* **2016,** 16, (2), 170-181.
72. Kim, J.; Bayram, C.; Park, H.; Cheng, C. W.; Dimitrakopoulos, C.; Ott, J. A.; Reuter, K. B.; Bedell, S. W.; Sadana, D. K. *Nature Communications* **2014,** 5, 4836.
73. Jiang, J.; Bitla, Y.; Huang, C.-W.; Do, T. H.; Liu, H.-J.; Hsieh, Y.-H.; Ma, C.-H.; Jang, C.-Y.; Lai, Y.-H.; Chiu, P.-W. *Science Advances* **2017,** 3, (6), e1700121.
74. Zhang, Y.; Cao, Y.-Q.; Hu, H.; Wang, X.; Li, P.; Yang, Y.; Zheng, J.; Zhang,

C.; Song, Z.; Li, A.-D. *ACS Applied Materials & Interfaces* **2019,** 11, (8), 8284-8290.
75. Liu, W.; Liu, M.; Ma, R.; Zhang, R.; Zhang, W.; Yu, D.; Wang, Q.; Wang, J.; Wang, H. *Advanced Functional Materials* **2018,** 28, (10), 1705928.
76. Yang, Y.; Gao, W.; Xie, Z.; Wang, Y.; Yuan, G.; Liu, J. M. *Advanced Electronic Materials* **2018,** 4, (12), 1800412.
77. Rogers, J. A.; Lagally, M. G.; Nuzzo, R. G. *Nature* **2011,** 477, (7362), 45-53.
78. Bakaul, S. R.; Serrao, C. R.; Lee, M.; Yeung, C. W.; Sarker, A.; Hsu, S.-L.; Yadav, A. K.; Dedon, L.; You, L.; Khan, A. I.; Clarkson, J. D.; Hu, C.; Ramesh, R.; Salahuddin, S. *Nature Communications* **2016,** 7, 10547.
79. Ueda, K.; Tabata, H.; Kawai, T. *Science* **1998,** 280, (5366), 1064-1066.
80. Blok, J. L.; Wan, X.; Koster, G.; Blank, D. H. A.; Rijnders, G. *Applied Physics Letters* **2011,** 99, (15), 151917.
81. Norton, D. R., *Pulsed laser deposition of thin films: applications-led growth of functional materials*. John Wiley & Sons: 2007.
82. Serna, M. I.; Yoo, S. H.; Moreno, S.; Xi, Y.; Oviedo, J. P.; Choi, H.; Alshareef, H. N.; Kim, M. J.; Minary-Jolandan, M.; Quevedo-Lopez, M. A. *ACS Nano* **2016,** 10, (6), 6054-6061.
83. Rijnders, G.; Blank, D., Growth kinetics during pulsed laser deposition. In *Pulsed Laser Deposition of Thin Films*, Eason, R., Ed. John Wiley & Sons: 2007; 177-190.
84. Connell, J. G.; Isaac, B. J.; Ekanayake, G. B.; Strachan, D. R.; Seo, S. S. A. *Applied Physics Letters* **2012,** 101, (25), 251607.
85. Woo, S.; Jeong, H.; Lee, S. A.; Seo, H.; Lacotte, M.; David, A.; Kim, H. Y.; Prellier, W.; Kim, Y.; Choi, W. S. *Scientific Reports* **2015,** 5, 8822.
86. Boschker, H.; Mathews, M.; Houwman, E. P.; Nishikawa, H.; Vailionis, A.; Koster, G.; Rijnders, G.; Blank, D. H. A. *Physical Review B* **2009,** 79, (21), 214425.
87. Garcia, V.; Bibes, M.; Maurice, J. L.; Jacquet, E.; Bouzehouane, K.; Contour, J. P.; Barthélémy, A. *Applied Physics Letters* **2005,** 87, (21), 212501.
88. Vailionis, A.; Boschker, H.; Siemons, W.; Houwman, E. P.; Blank, D. H. A.; Rijnders, G.; Koster, G. *Physical Review B* **2011,** 83, (6), 064101.
89. Majumdar, S.; Kooser, K.; Elovaara, T.; Huhtinen, H.; Granroth, S.; Paturi, P. *Journal of Physics: Condensed Matter* **2013,** 25, (37), 376003.
90. Jin, L.; Li, F.; Zhang, S.; Green, D. J. *Journal of the American Ceramic Society* **2014,** 97, (1), 1-27.
91. Acosta, M.; Novak, N.; Rojas, V.; Patel, S.; Vaish, R.; Koruza, J.; Rossetti, G. A.; Rödel, J. *Applied Physics Reviews* **2017,** 4, (4), 041305.
92. Kim, Y. S.; Kim, D. H.; Kim, J. D.; Chang, Y. J.; Noh, T. W.; Kong, J. H.;

Char, K.; Park, Y. D.; Bu, S. D.; Yoon, J. G.; Chung, J. S. *Applied Physics Letters* **2005,** 86, (10), 102907.
93. Choi, K. J.; Biegalski, M.; Li, Y.; Sharan, A.; Schubert, J.; Uecker, R.; Reiche, P.; Chen, Y.; Pan, X.; Gopalan, V. *Science* **2004,** 306, (5698), 1005-1009.
94. Scott, J. F. *Science* **2007,** 315, (5814), 954-959.
95. Yang, S.; Bao, H.; Zhou, C.; Wang, Y.; Ren, X.; Matsushita, Y.; Katsuya, Y.; Tanaka, M.; Kobayashi, K.; Song, X.; Gao, J. *Physical Review Letters* **2010,** 104, (19), 197201.
96. Megaw, H. D. *Proceedings of the Physical Society* **1946,** 58, (2), 19.
97. Frantti, J.; Lappalainen, J.; Eriksson, S.; Lantto, V.; Nishio, S.; Kakihana, M.; Ivanov, S.; Rundlöf, H. *Japanese Journal of Applied Physics* **2000,** 39, 6.
98. Catalan, G.; Scott, J. F. *Advanced Materials* **2009,** 21, (24), 2463-2485.
99. Seidel, J.; Fu, D.; Yang, S.-Y.; Alarcón-Lladó, E.; Wu, J.; Ramesh, R.; Ager, J. W. *Physical Review Letters* **2011,** 107, (12), 126805.
100. Chu, Y. H.; Cruz, M. P.; Yang, C. H.; Martin, L. W.; Yang, P. L.; Zhang, J. X.; Lee, K.; Yu, P.; Chen, L. Q.; Ramesh, R. *Advanced Materials* **2007,** 19, (18), 2662-2666.
101. Yang, M. M.; Alexe, M. *Advanced Materials* **2018,** 30, (14), 1704908.
102. Lu, D.; Baek, D. J.; Hong, S. S.; Kourkoutis, L. F.; Hikita, Y.; Hwang, H. Y. *Nature Materials* **2016,** 15, (12), 1255-1260.
103. Waseda, Y.; Matsubara, E.; Shinoda, K., *X-ray diffraction crystallography: introduction, examples and solved problems*. Springer Science & Business Media: 2011.
104. Cullity, B.; Stock, S., *Elements of X-ray Diffraction*. Prentice Hall: New Jersey, 2001; 170.
105. Pennycook, S.; Lupini, A.; Varela, M.; Borisevich, A.; Peng, Y.; Oxley, M.; Van Benthem, K.; Chisholm, M., Scanning transmission electron microscopy for nanostructure characterization. In *Scanning Microscopy for Nanotechnology*, Springer: 2006;152-191.
106. Alsteens, D.; Gaub, H. E.; Newton, R.; Pfreundschuh, M.; Gerber, C.; Müller, D. J. *Nature Reviews Materials* **2017,** 2, (5), 17008.
107. Kalinin, S. V.; Gruverman, A., *Scanning probe microscopy: electrical and electromechanical phenomena at the nanoscale*. Springer Science & Business Media: 2007; Vol. 1.
108. Balke, N.; Maksymovych, P.; Jesse, S.; Herklotz, A.; Tselev, A.; Eom, C.-B.; Kravchenko, I. I.; Yu, P.; Kalinin, S. V. *ACS Nano* **2015,** 9, (6), 6484-6492.
109. Kalinin, S. V.; Morozovska, A. N.; Chen, L. Q.; Rodriguez, B. J. *Reports on Progress in Physics* **2010,** 73, (5), 056502.
110. Buchner, M.; Höfler, K.; Henne, B.; Ney, V.; Ney, A. *Journal of Applied*

Physics **2018,** 124, (16), 161101.
111. Jiles, D., *Introduction to magnetism and magnetic materials*. CRC press: 2015.
112. Sawicki, M.; Stefanowicz, W.; Ney, A. *Semiconductor Science Technology* **2011,** 26, (6), 064006.
113. Parkin, S. S.; Kaiser, C.; Panchula, A.; Rice, P. M.; Hughes, B.; Samant, M.; Yang, S.-H. *Nature Materials* **2004,** 3, (12), 862-867.
114. Burton, J. D.; Tsymbal, E. Y. *Philosophical Transactions of the Royal Society A: Mathematical, Physical and Engineering Sciences* **2012,** 370, (1977), 4840-4855.
115. Xiang, G.; Sheu, B. L.; Zhu, M.; Schiffer, P.; Samarth, N. *Physical Review B* **2007,** 76, (3), 035324.
116. Yin, Y.-W.; Huang, W.-C.; Liu, Y.-K.; Yang, S.-W.; Dong, S.-N.; Tao, J.; Zhu, Y.-M.; Li, Q.; Li, X.-G. *Advanced Electronic Materials* **2015,** 1, (11), 1500183.
117. Fang, Y.; Dumas, R. K.; Nguyen, T. N. A.; Mohseni, S. M.; Chung, S.; Miller, C. W.; Åkerman, J. *Advanced Functional Materials* **2013,** 23, (15), 1919-1922.
118. Yin, Y. W.; Raju, M.; Hu, W. J.; Burton, J. D.; Kim, Y. M.; Borisevich, A. Y.; Pennycook, S. J.; Yang, S. M.; Noh, T. W.; Gruverman, A.; Li, X. G.; Zhang, Z. D.; Tsymbal, E. Y.; Li, Q. *Journal of Applied Physics* **2015,** 117, (17), 172601.
119. Duan, C. G.; Jaswal, S. S.; Tsymbal, E. Y. *Physical Review Letters* **2006,** 97, (4), 047201.
120. Quindeau, A.; Fina, I.; Marti, X.; Apachitei, G.; Ferrer, P.; Nicklin, C.; Pippel, E.; Hesse, D.; Alexe, M. *Scientific Reports* **2015,** 5, 9749.
121. Yin, Y. W.; Burton, J. D.; Kim, Y. M.; Borisevich, A. Y.; Pennycook, S. J.; Yang, S. M.; Noh, T. W.; Gruverman, A.; Li, X. G.; Tsymbal, E. Y.; Li, Q. *Nature Materials* **2013,** 12, (5), 397-402.
122. Mao, H. J.; Miao, P. X.; Cong, J. Z.; Song, C.; Cui, B.; Peng, J. J.; Li, F.; Wang, G. Y.; Zhao, Y. G.; Sun, Y.; Xiao, L. R.; Pan, F. *Journal of Applied Physics* **2014,** 116, (5), 053703.
123. Velev, J. P.; Duan, C. G.; Belashchenko, K. D.; Jaswal, S. S.; Tsymbal, E. Y. *Physical Review Letters* **2007,** 98, (13), 137201.
124. Pantel, D.; Goetze, S.; Hesse, D.; Alexe, M. *ACS Nano* **2011,** 5, (7), 6032-6038.
125. Kim, D. J.; Lu, H.; Ryu, S.; Bark, C. W.; Eom, C. B.; Tsymbal, E. Y.; Gruverman, A. *Nano Letters* **2012,** 12, (11), 5697-5702.
126. Quindeau, A.; Borisov, V.; Fina, I.; Ostanin, S.; Pippel, E.; Mertig, I.; Hesse, D.; Alexe, M. *Physical Review B* **2015,** 92, (3), 035130.

127. Quindeau, A.; Hesse, D.; Alexe, M. *Frontiers in Physics* **2014,** 2, 7.
128. Boyn, S.; Grollier, J.; Lecerf, G.; Xu, B.; Locatelli, N.; Fusil, S.; Girod, S.; Carrétéro, C.; Garcia, K.; Xavier, S. *Nature Communications* **2017,** 8, 14736.
129. Burton, J. D.; Tsymbal, E. Y. *Physical Review B* **2009,** 80, (17), 174406.
130. Yamada, H.; Garcia, V.; Fusil, S.; Boyn, S.; Marinova, M.; Gloter, A.; Xavier, S.; Grollier, J.; Jacquet, E.; Carrétéro, C. *ACS Nano* **2013,** 7, (6), 5385-5390.
131. De Teresa, J. M.; Barthélémy, A.; Fert, A.; Contour, J. P.; Montaigne, F.; Seneor, P. *Science* **1999,** 286, (5439), 507-509.
132. Apachitei, G.; Peters, J. J.; Sanchez, A. M.; Kim, D. J.; Alexe, M. *Advanced Electronic Materials* **2017,** 3, (7), 1700126.
133. Chanthbouala, A.; Crassous, A.; Garcia, V.; Bouzehouane, K.; Fusil, S.; Moya, X.; Allibe, J.; Dlubak, B.; Grollier, J.; Xavier, S.; Deranlot, C.; Moshar, A.; Proksch, R.; Mathur, N. D.; Bibes, M.; Barthelemy, A. *Nature Nanotechnology* **2011,** 7, (2), 101-104.
134. Wen, Z.; Li, C.; Wu, D.; Li, A.; Ming, N. *Nature Materials* **2013,** 12, (7), 617-621.
135. Li, W.; Alexe, M. *Applied Physics Letters* **2007,** 91, (26), 262903.
136. Tan, H.; Liu, G.; Zhu, X.; Yang, H.; Chen, B.; Chen, X.; Shang, J.; Lu, W. D.; Wu, Y.; Li, R. W. *Advanced Materials* **2015,** 27, (17), 2797-803.
137. Kim, J.; Lee, H. C.; Kim, K. H.; Hwang, M. S.; Park, J. S.; Lee, J. M.; So, J. P.; Choi, J. H.; Kwon, S. H.; Barrelet, C. J.; Park, H. G. *Nature Nanotechnology* **2017,** 12, (10), 963-968.
138. Ye, C.; Peng, Q.; Li, M.; Luo, J.; Tang, Z.; Pei, J.; Chen, J.; Shuai, Z.; Jiang, L.; Song, Y. *Journal of the American Chemical Society* **2012,** 134, (49), 20053-20059.
139. Lee, D.; Hwang, E.; Lee, Y.; Choi, Y.; Kim, J. S.; Lee, S.; Cho, J. H. *Advanced Materials* **2016,** 28, (41), 9196-9202.
140. Ungureanu, M.; Zazpe, R.; Golmar, F.; Stoliar, P.; Llopis, R.; Casanova, F.; Hueso, L. E. *Advanced Materials* **2012,** 24, (18), 2496-2500.
141. Guan, X.; Hu, W.; Haque, M. A.; Wei, N.; Liu, Z.; Chen, A.; Wu, T. *Advanced Functional Materials* **2018,** 28, (3), 1704665.
142. Jin Hu, W.; Wang, Z.; Yu, W.; Wu, T. *Nature Communications* **2016,** 7, 10808.
143. Baugher, B. W.; Churchill, H. O.; Yang, Y.; Jarillo-Herrero, P. *Nature Nanotechnology* **2014,** 9, (4), 262-267.
144. Sarker, B. K.; Cazalas, E.; Chung, T. F.; Childres, I.; Jovanovic, I.; Chen, Y. P. *Nature Nanotechnology* **2017,** 12, (7), 668-674.
145. Rubio-Marcos, F.; Ochoa, D. A.; Del Campo, A.; García, M. A.; Castro, G.

R.; Fernández, J. F.; García, J. E. *Nature Photonics* **2017,** 12, (1), 29-32.
146. Manz, S.; Matsubara, M.; Lottermoser, T.; Büchi, J.; Iyama, A.; Kimura, T.; Meier, D.; Fiebig, M. *Nature Photonics* **2016,** 10, (10), 653-656.
147. Bera, A.; Peng, H.; Lourembam, J.; Shen, Y.; Sun, X. W.; Wu, T. *Advanced Functional Materials* **2013,** 23, (39), 4977-4984.
148. Irvin, P.; Ma, Y.; Bogorin, D. F.; Cen, C.; Bark, C. W.; Folkman, C. M.; Eom, C.-B.; Levy, J. *Nature Photonics* **2010,** 4, (12), 849-852.
149. Leydecker, T.; Herder, M.; Pavlica, E.; Bratina, G.; Hecht, S.; Orgiu, E.; Samori, P. *Nature Nanotechnology* **2016,** 11, (9), 769-75.
150. Ebrahimi, M.; Rosei, F. *Nature Photonics* **2016,** 10, (7), 434-436.
151. Matsuo, H.; Noguchi, Y.; Miyayama, M. *Nature Communications* **2017,** 8, (1), 207.
152. Sze, S. M.; Ng, K. K., *Physics of semiconductor devices*. John wiley & sons: 2006.
153. Lampert, M.; Many, A.; Mark, P. *Physical Review* **1964,** 135, (5A), A1444.
154. Lampert, M. A.; Mark, P., *Current injection in solids*. Academic Press: New York, 1970.
155. Alexe, M. *Nano Letters* **2012,** 12, (5), 2193-2198.
156. Bhatnagar, A.; Kim, Y. H.; Hesse, D.; Alexe, M. *Applied Physics Letters* **2014,** 105, (12), 122905.
157. Guo, E. J.; Roth, R.; Herklotz, A.; Hesse, D.; Dorr, K. *Advanced Materials* **2015,** 27, (9), 1615-1618.
158. Grigoriev, A.; Do, D. H.; Kim, D. M.; Eom, C. B.; Adams, B.; Dufresne, E. M.; Evans, P. G. *Physical Review Letters* **2006,** 96, (18), 187601.
159. Sharma, B. K.; Ahn, J.-H. *Advanced Electronic Materials* **2016,** 2, (8), 1600105.
160. Koo, J. H.; Kim, D. C.; Shim, H. J.; Kim, T.-H.; Kim, D.-H. *Advanced Functional Materials* **2018,** 28, (35), 1801834.
161. Lee, H. E.; Park, J. H.; Kim, T. J.; Im, D.; Shin, J. H.; Kim, D. H.; Mohammad, B.; Kang, I.-S.; Lee, K. J. *Advanced Functional Materials* **2018,** 28, (32), 1801690.
162. Melzer, M.; Monch, J. I.; Makarov, D.; Zabila, Y.; Canon Bermudez, G. S.; Karnaushenko, D.; Baunack, S.; Bahr, F.; Yan, C.; Kaltenbrunner, M.; Schmidt, O. G. *Advanced Materials* **2015,** 27, (7), 1274-1280.
163. Yang, J. J.; Strukov, D. B.; Stewart, D. R. *Nature Nanotechnology* **2013,** 8, (1), 13-24.
164. Borghetti, J.; Snider, G. S.; Kuekes, P. J.; Yang, J. J.; Stewart, D. R.; Williams, R. S. *Nature* **2010,** 464, (7290), 873-876.
165. Waser, R.; Dittmann, R.; Staikov, G.; Szot, K. *Advanced Materials* **2009,**

21, (25-26), 2632-2663.
166. Yang, Y.; Lu, W. *Nanoscale* **2013,** 5, (21), 10076-10092.
167. Boybat, I.; Le Gallo, M.; Nandakumar, S. R.; Moraitis, T.; Parnell, T.; Tuma, T.; Rajendran, B.; Leblebici, Y.; Sebastian, A.; Eleftheriou, E. *Nature Communications* **2018,** 9, (1), 2514.
168. Baek, D. J.; Lu, D.; Hikita, Y.; Hwang, H. Y.; Kourkoutis, L. F. *ACS Applied Materials & Interfaces* **2017,** 9, (1), 54-59.
169. Li, X.; Zhu, Y.; Cai, W.; Borysiak, M.; Han, B.; Chen, D.; Piner, R. D.; Colombo, L.; Ruoff, R. *Nano Letters* **2009,** 9, (12), 4359-4363.
170. Paskiewicz, D. M.; Sichel-Tissot, R.; Karapetrova, E.; Stan, L.; Fong, D. D. *Nano Letters* **2016,** 16, (1), 534-542.
171. Jang, H. W.; Baek, S. H.; Ortiz, D.; Folkman, C. M.; Das, R. R.; Chu, Y. H.; Shafer, P.; Zhang, J. X.; Choudhury, S.; Vaithyanathan, V.; Chen, Y. B.; Felker, D. A.; Biegalski, M. D.; Rzchowski, M. S.; Pan, X. Q.; Schlom, D. G.; Chen, L. Q.; Ramesh, R.; Eom, C. B. *Physical Review Letters* **2008,** 101, (10), 107602.
172. Wei, Y.; Nukala, P.; Salverda, M.; Matzen, S.; Zhao, H. J.; Momand, J.; Everhardt, A. S.; Agnus, G.; Blake, G. R.; Lecoeur, P.; Kooi, B. J.; Iniguez, J.; Dkhil, B.; Noheda, B. *Nature Materials* **2018,** 17, (12), 1095.
173. Liu, D.; Cheng, H.; Zhu, X.; Wang, G.; Wang, N. *ACS Appllied Materials & Interfaces* **2013,** 5, (21), 11258-11264.
174. Chua, L. *Applied Physics A* **2011,** 102, (4), 765-783.
175. Kim, S.; Jeong, H. Y.; Kim, S. K.; Choi, S. Y.; Lee, K. J. *Nano Letters* **2011,** 11, (12), 5438-4542.
176. Wang, Z.; Joshi, S.; Savel'ev, S.; Song, W.; Midya, R.; Li, Y.; Rao, M.; Yan, P.; Asapu, S.; Zhuo, Y.; Jiang, H.; Lin, P.; Li, C.; Yoon, J. H.; Upadhyay, N. K.; Zhang, J.; Hu, M.; Strachan, J. P.; Barnell, M.; Wu, Q.; Wu, H.; Williams, R. S.; Xia, Q.; Yang, J. J. *Nature Electronics* **2018,** 1, (2), 137-145.
177. Pickett, M. D.; Medeiros-Ribeiro, G.; Williams, R. S. *Nature Materials* **2013,** 12, (2), 114-117.